# Intersubband polaritons in photonic crystal cavities

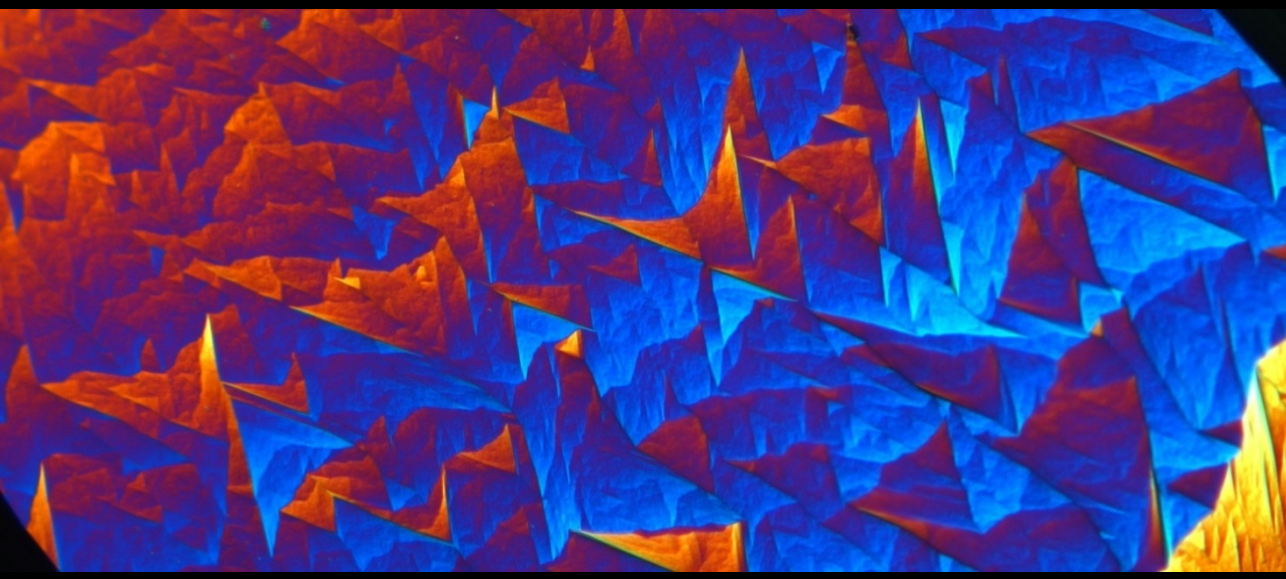

Simone Zanotto

Scuola Normale Superiore

Ph. D. Thesis

# Intersubband polaritons in photonic crystal cavities

Simone Zanotto

*Advisor:*
Prof. Alessandro Tredicucci

2014

*a Giulio Rampa*

# Contents

# Introduction

Light and matter, which in everyday's life usually appear as well separated physical entities, lose their mutual independence when the interaction between them is sufficiently strong. Technically speaking, this independence is lost when a light emitter (like a single atom, or an assembly of identical atoms) is embedded in a cavity supporting a *single* mode of the electromagnetic field – like the resonance of a Fabry-Pérot device. Moreover, the loss rates have to be smaller than the light-matter coupling constant.

The need for a single mode of the electromagnetic field, and for a sufficiently large coupling constant, can be understood as follows. If the electromagnetic field has a continuum of modes, the photons are randomly emitted by the "atoms" into a macroscopic number of scattering channels, and finally get irreversibly lost. In this case, the system is described by a *perturbative* theory – like the Fermi golden rule. A similar situation occurs when considering a single-mode cavity, but featuring a decay rate larger in comparison to the light-matter coupling strength. The photon emitted into the cavity mode is more likely to undergo irreversible dephasing due to losses, rather than to be re-absorbed by the "atom".

When the coupling strength is instead larger than the decay rates, the system enters the *non-perturbative regime*. From a quantum-mechanical point of view, the eigenstates of the strongly coupled system are no more the unperturbed ones originating from the separated light and matter Hamiltonians, but rather a superposition of states taken from both the light and the matter Hilbert spaces; these states are named *dressed states*, or *polaritons*.

The terminology *dressed states* was introduced when the first experiments concerning Rydberg atoms in microwave cavities were performed [Kaluzny83, Thompson92]. In the following years, when the advances in semiconductor nanostructure processing opened the way

towards integrated quantum emitter/photonic resonator devices, the concept of *cavity polariton* entered the physicist's lexicon. The term *cavity polariton* is mostly used when the matter constituent is approximately a *boson*, like an exciton, or an intersubband transition in a semiconductor quantum well; the definition *dressed state* is instead usually employed when the matter constituent is a *fermion*, like a single atom or a semiconductor quantum dot.

The first observation of cavity polaritons, [Weisbuch92], relied on an excitonic transition as the matter constituent. Exciton-polaritons experienced a wide success thanks, for instance, to their impact on ultralow threshold optoelectronic devices, and for having enabled on-chip experiments about Bose-Einstein condensation and related phenomena like polariton superfluidity [Kavokin07].

While exciton-polaritons rely on the optical interband transition of a semiconductor quantum well (QW), if one seeks for the analogous phenomenon involving the transitions between the conduction subbands in a QW, the concept of *intersubband polariton* emerges. This new quasiparticle has been theoretically predicted in 1997 [Liu97], experimentally observed in 2003 [Dini03], and widely explored in the forthcoming years, especially by the quantum cascade laser community – thanks to the affinity of theoretical and experimental methods involved.

Indeed, it is not only this affinity that motivates the research in intersubband polaritons. While quantum cascade lasers underwent deep physical investigations and engineering throughout the last decades, they still suffer from quite small efficiency and low operating temperatures, at least when devices operating in the THz spectral range are considered. In order to overcome these limitations, in the last few years two alternative mechanisms leading to mid-infrared and THz lasing without inversion have been proposed, relying on radiative or non-radiative polariton-polariton scattering mechanisms [De Liberato09c, De Liberato13].

When looking towards devices which implement these theoretical insights, three main issues have to be addressed. (i) The radiative coupling efficiency between polariton states and free-space photons has to be optimized. This follows from the need of effectively populate the upper polariton state (by means of optical pumping, in a proof-of-principle device; a final device would instead preferrably rely on electrical pumping), and of effectively extract the light from the lower polariton state (i.e. the final state in the two-level polariton laser). (ii)

An engineering of the photonic dispersion, which implies the *bottlenecking*, may be of key relevance, in analogy with the observations concerning exciton-polaritons. (iii) It should be verified that the strong coupling is not saturated (*bleached*) by the pump beam which populates the upper polariton state.

In this thesis work we addressed the above issues, by introducing the *metallo-dielectric photonic crystal slab resonator* (MD-PhCS) geometry for the photonic cavity. As opposed to the resonator geometries known in the literature (planar slab, patch cavities, LC resonators [Dini03, Todorov09, Geiser10]), the MD-PhCS allows for a simultaneous control of the radiative linewidth – of key relevance in controlling the coupling between polaritons and free-space photons, point (i) in the above – and of the photonic mode dispersion, point (ii).

It is especially the first point that has been deeply studied, highlighting the relevance of damping rate matching between the cavity mode and the intersubband resonance. By introducing a semiclassical coupled-mode model of a single-mode optical cavity which embeds a matter resonance (**Chapter 2**), we figured out that the damping rate matching implies a peculiar condition which we named *strong critical coupling* (SCC). Under this condition, the absorption spectrum of the cavity is a doublet of peaks which reach unity values. This means that energy transfer between the incoming waves and the matter constituents is full – *critical coupling*, well known in device physics [Haus84, Yariv07]; in addition, the spectral doublet is the clear counterpart of *strong coupling*, i.e. non-perturbative light-matter coupling. In other words, all the incident photons are converted into polaritons – in our case, intersubband polaritons. This is not the whole story; actually, the perfect absorption into polariton states has been experimentally observed in a slightly more complicated (and rich) arrangement. Since a photonic crystal slab can be illuminated from both surfaces, we performed a *coherent absorption experiment*, where two beams simultaneously excite the two surfaces of the membrane. By sweeping the optical dephasing of the beams, it turns out that in a sample under SCC condition the polaritonic absorption can be tuned from zero to unity, hence opening interesting avenues towards the coherent control of the polariton population inside the sample.

The above described *polaritonic coherent perfect absorption* is perhaps the central result of **Chapter 3**, which in general reports on the *linear response* of photonic crystal intersubband polariton samples. The material contained therein is fully original, starting from the design

of a simple photonic crystal sample, passing through the analysis of defect-mode intersubband polaritons, and concluding with a method for tuning the radiative linewidth of a double-metal photonic crystal resonator mainly intended for the terahertz spectral range.

In the thesis work we also addressed the *non-linear response* of intersubband polaritons. This was mainly motivated by the point (iii) outlined above: when high power pumping is involved, the polariton concept itself may lose its validity due to saturation of the light-matter coupling. This phenomenon, already known in the exciton-polariton framework [Houdré95, Norris95], has been observed for the first time in an intersubband-polariton sample, leading to the definition of an intersubband polariton saturation threshold. Since this threshold lies above the stimulated scattering threshold, lasing induced by polariton-polariton scattering is potentially within experimental reach (**Chapter 4**). In that Chapter we also provide a semiclassical, rate-equation based model, which correctly describes the observed polariton saturation. In addition, the model suggests that intersubband polariton bistability could occur under specific monochromatic intense pumping, and under specific cooperativity conditions.

Finally, in **Chapter 4** we also report on experiments concerning ultrafast polariton switch-on. The reaching of the ultimate speed of such a switching process is of overwhelming importance towards the so-called *vacuum photon emission*, a phenomenon reminiscent of the dynamical Casimir effect that was predicted for ultrastrongly-coupled systems. Intersubband polaritons have shown potentials in this direction [Anappara09, Günter09], especially in connection with the photonic crystal geometry which implies significant simplifications of the experimental set-up.

The content of the manuscript is completed by **Chapter 1**, which introduces the intersubband polariton physics in a generic photonic resonator, and with the **Appendices**, where the theory of coherent perfect absorption, and the sample fabrication protocols, are summarized.

# Chapter 1

# Quantum and semiclassical theory of intersubband polaritons

The aim of this Chapter is to give a detailed insight into the theory of intersubband polaritons, mainly focusing on the concepts that will be relevant in the experimental implementations that are the main topic of this thesis.

Two complementary approaches are discussed, each of them revealing some key features of intersubband polariton physics. At first, in Section 1.3 a quantum Hamiltonian treatment that describes on the same footing electron-cavity as well as electron-electron interactions is given. Secondly, a semiclassical approach which models the quantum wells as a dispersive dielectric medium is introduced (Sect. 1.4). Those approaches explicitly rely on the properties of *intersubband transitions* as the matter constituent of polariton states, and some properties inherent to intersubband physics (like the depolarization shift) will be thoroughly discussed.

## 1.1 Electron confinement in a quantum well

As for a significant part of intersubband-related devices like quantum cascade lasers or quantum well infrared photodetectors (QCLs, QWIPs), in this work we treat quantum wells (QWs) realized em-

ploying GaAs and $Al_{0.33}Ga_{0.67}As$ as materials for wells and barriers. The above compounds can be integrated with other $Al_xGa_{1-x}As$ alloys which are useful both as low-index optical guiding layers and as etching stop layers. This is the case, respectively, of the compounds $Al_{0.95}Ga_{0.05}As$ and $Al_{0.5}Ga_{0.5}As$.

The description of quantum states in a quantum well is often given in terms of the *envelope function* formalism [Bastard88]. The idea, taken from the $\mathbf{k}\cdot\mathbf{p}$ method for bulk semiconductors, is that the electron wavefunction can be expanded over the basis of the bulk semiconductor wavefunctions at a certain high-symmetry point; for direct-gap semiconductors, the involved states are typically those at the $\Gamma$ point. Depending on the desired precision, one or more bands can be taken into account; here we sketch the basic theory for a one-band model, which can only be used for a rough quantitative prediction of the intersubband transition energy.

In this model the electron wavefunction is

$$\psi_{\mathbf{k},\lambda}(\mathbf{r},z) = u_\Gamma^{B,W}(\mathbf{r},z)\phi_\lambda(z)e^{i\mathbf{k}\cdot\mathbf{r}},$$

where $u_\Gamma^B$ ($u_\Gamma^W$) is the conduction band wavefunction of the barrier (well) material at the $\Gamma$ point, $\phi(z)$ is the envelope function and $\mathbf{k} = (k_x, k_y)$ is the conserved wavevector component lying in the epitaxial plane; $\lambda$ is the subband quantum number. The envelope function satisfies the *Ben Daniel – Duke* equation, what, for a bulk isotropic and parabolic band, reads

$$\left[-\partial_z \frac{\hbar^2}{2m^*(z)}\partial_z + \frac{\hbar^2 k^2}{2m^*(z)} + V(z) - \hbar\omega_\lambda\right]\phi_\lambda(z) = 0. \qquad (1.1)$$

Electrons are confined by the conduction band profile $V(z)$, and experience different effective masses $m^*$ depending on the material where they are travelling. Under the hypothesis that the energy levels are not too close to the barrier potential, the energy of the quantum state $(\mathbf{k},\lambda)$ is well approximated by the expression

$$\hbar\omega_{\lambda\mathbf{k}} = \hbar\omega_\lambda + \hbar^2k^2/2m^* \qquad (1.2)$$

which is referred to as *parabolic subband approximation*.

Equation 1.1 can be solved semianalytically for a single quantum well consisting, for instance, of a GaAs well embedded between thick $Al_{0.33}Ga_{0.67}As$ barriers. This is because Eq. 1.1 can be solved piecewise in the layers where $V$ is constant, and the global solution is obtained

by matching both $\phi$ and $\partial_z\phi/m^*$ across the interfaces. Provided that the confining potential and barrier width are in a given range, Eq. 1.1 displays two solutions $\lambda = 1, 2$. In the following we will work within this hypothesis, both in the further developments of the theory and in designing the samples.

When the quantum well is populated by electrons, the Coulomb potential arising from their spatial distribution modifies the original heterostructure potential $V$. This Hartree term, that has to be calculated self-consistently on the basis of the electron distribution function (e.g. the thermal Fermi-Dirac distribution), leads to a red shift of the transition $\omega_{12} = \omega_2 - \omega_1$. However, this red shift is usually more than compensated by the so-called *depolarization shift*, whose nature is fully discussed in Sect. 1.3.4. For this reason, if the charge density involved is not too large, the Hartree and depolarization shifts can be simultaneously neglected at least at the design stage.

As a fundamental linking point between quantum and classical theory of the dielectric response, the adimensional quantity *oscillator strength* is introduced:

$$f_0 = \frac{2m^*\omega_{12}}{\hbar} z_{12}^2 \tag{1.3}$$

where $z_{12} = \int \phi_1(z)\phi_2(z)\, z\, dz$ is the dipole matrix element of the transition. The dipole of the transition (and the oscillator strength[1]) are connected to the intersubband current

$$\xi(z) = \phi_2(z)\partial_z\phi_1(z) - \phi_1(z)\partial_z\phi_2(z) \tag{1.4}$$

via the expression

$$\int_{-\infty}^{+\infty} \xi(z)\, dz = \frac{2m^*\omega_{12}}{\hbar} z_{12}. \tag{1.5}$$

Finally, we introduce the *quantum well effective length* [Todorov12]. It reads

$$L_{\text{eff}} = \frac{2m^*\omega_{12}}{\hbar \int \xi^2} \tag{1.6}$$

and describes the spatial region in which the quantum intersubband current takes place[2]. All these concepts will be employed in Sect. 1.3, when the quantum well is embedded in a photonic resonator.

[1] Care has to be taken while comparing different works, since it is also common to find $f_0 = 2m\omega_{12}z_{12}^2/\hbar$, where $m$ is the free-electron mass.

[2] As an insight into typical values, if one considers the first two levels of an infinite-barrier quantum well of length $L$, the numbers $f_0 = 2^8/(3^3\pi^2) \simeq 0.96$, $z_{12}/L = 16/(9\pi^2) \simeq 0.18$, $L_{\text{eff}}/L = 3/5$ are obtained.

## 1.2 Photon confinement in a slab waveguide

In the following we will sketch the basics of electromagnetic wave confinement, again in one spatial dimension. The system we are referring to is the *planar slab waveguide*; a general discussion can be found in any photonic textbook like [Yariv07]. Here we report some formulas and concepts that will be useful in the next Chapters.

A sequence of dielectric layers gives rise to a permittivity function $\varepsilon(z)$ which depends only on one spatial dimension. The translational invariance naturally induces a dependence of the fields from the in-plane coordinate $\mathbf{r} = (r_x, r_y)$ of the form $e^{i\mathbf{k}\cdot\mathbf{r}}$, which physically corresponds to a propagating field along the in-plane direction $\mathbf{k}$. Furthermore, the translational invariance along two directions removes the intrinsic vectorial nature of the electromagnetic problem, hence inducing two independent polarization states – TE and TM. Due to the selection rules for intersubband transitions, the only relevant polarization is TM, and we will focus our analysis on that single case. With these hypothesis, the Maxwell equations for a monochromatic field reduce to the Helmholtz equation

$$\left[-\partial_z^2 + k^2 - \varepsilon(z)\frac{\omega_{i\mathbf{k}}^2}{c^2}\right] f(z) = 0 \tag{1.7}$$

where $\omega_{i\mathbf{k}}^2$ is the angular frequency of the $i$-th cavity mode, and $k$ is the modulus of the in-plane propagation wavevector[3]. According to the boundary conditions for the electromagnetic fields, the functions $f$ and $\partial_z f/\varepsilon$ have to be continuous across the boundaries where $\varepsilon(z)$ has a jump[4].

A useful derived quantity is the *effective dielectric constant*, which is defined as $\varepsilon_{\text{eff},i} = c^2k^2/\omega_{i\mathbf{k}}^2$. It describes the permittivity "seen" by the $i$-th propagating mode, and is a kind of average of the permittivities of the layers where the field is confined.

[3] In the engineering literature this quantity is usually referred to as $\beta$.

[4] Notice that the photon confinement problem is similar to that for the electronic wavefunction, but not completely analogous. Indeed, the frequency eigenvalue in the first case *adds* to the confining potential $V(z)$, while in the second case it *multiplies* the "confining potential" $\varepsilon(z)$.

The complete expressions for the fields are

$$\begin{aligned}
\mathbf{H}(\mathbf{r},z) &= iH_0\ (\mathbf{e}_\mathbf{k}\times\mathbf{e}_z)f_\mathbf{k}(z)\ e^{i\mathbf{k}\cdot\mathbf{r}}\\
\mathbf{D}_\parallel(\mathbf{r},z) &= -H_0\ \mathbf{e}_\mathbf{k}\ \frac{1}{\omega_{i\mathbf{k}}}\ \partial_z f_\mathbf{k}(z)\ e^{i\mathbf{k}\cdot\mathbf{r}}\\
\mathbf{D}_z(\mathbf{r},z) &= iH_0\ \mathbf{e}_z\frac{|\mathbf{k}|}{\omega_{i\mathbf{k}}}\ f_\mathbf{k}(z)\ e^{i\mathbf{k}\cdot\mathbf{r}}
\end{aligned} \tag{1.8}$$

where $\mathbf{e}_\mathbf{k}$ is the unit vector along the $\mathbf{k}$ direction. In this classical theory $H_0$ is the wave field amplitude, linked to the power flux in the waveguide; in the next Section we will give the quantum expression of $H_0$ linked to a single photon wavepacket.

The presence of a field profile $f_\mathbf{k}(z)$, which can vary by a significant amount across the region embedding the QW in the final polaritonic device, is a key point of the following Sections, where it will be shown that the quantum excitations have to "accommodate" the actual field they experience.

## 1.3 Quantum Hamiltonian treatment of ultra-strong coupling

The non-dissipative quantum theory of intersubband polaritons was first developed in a fundamental paper published in 2005 [Ciuti05], where the relevance of anti-resonant terms in the light-matter coupling Hamiltonian is fully discussed. On that occasion the term *ultra-strong coupling* (USC) was introduced, together with the proposal of exploiting intersubband polaritonic devices for the observation of vacuum photon radiation phenomena. These ideas originate from the possibility to embed a large volume density of electrons in the quantum wells of a polaritonic cavity, thus leading to a large ratio between the coupling constant $\Omega$ and the ISB transition frequency $\omega_{12}$. It is indeed the adimensional value $\Omega/\omega_{12}$ which governs the effectiveness of the rotating-wave approximation in the usual strong coupling Hamiltonian – that is, the one neglecting antiresonant terms. When $\Omega/\omega_{12}$ is of the order of 0.1, the difference between the models with and without antiresonant terms becomes experimentally accessible, as first pointed out in [Anappara09]. Further proofs of the USC physics were evidenced in [Todorov09], where the use of a THz transition[5] allowed

[5] It can be shown that for a square QW in the $GaAs/Al_{0.33}Ga_{0.67}As$ system the scaling law $\Omega/\omega_{12} \propto \sqrt{1/\omega_{12}}$ holds [Ciuti05].

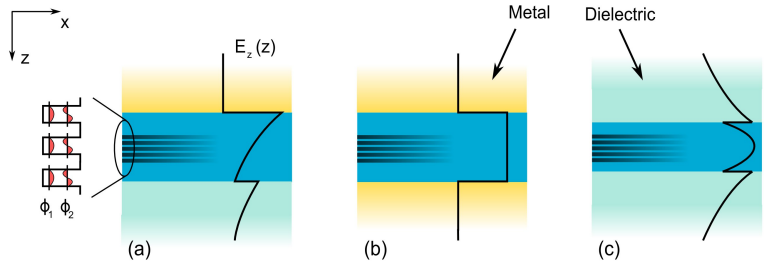


Figure 1.1: Schematics of the planar waveguides on which – more or less directly – most of the works on intersubband polaritons rely. *Panel (a),* surface-plasmon waveguide; *panel (b),* double-metal waveguide (also known as metal-insulator-metal waveguide – MIM); *panel (c),* ordinary dielectric slab waveguide.

even larger values of $\Omega/\omega_{12}$.

In the paper by Ciuti, the electromagnetic field is treated in the Coulomb gauge, and the coupling constant $\Omega$ is obtained by evaluating matrix elements of the form $\langle \mathbf{A} \cdot \mathbf{p} \rangle$. However, this analysis did not explicitly treat the dynamic electron-electron Coulomb interaction, which in an isolated QW leads to the well known *depolarization shift* effect [Ando82]. The latter consists in a blue-shift of the resonance frequency with respect to the value that one would calculate by considering only the static Coulomb interaction (i.e. the Hartree self-consistent potential). As both the depolarization shift and the coupling constant $\Omega/\omega_{12}$ increase when the electron density in the polaritonic device is increased, the researcher interested in the ultra-strong coupling regime would do better by relying on a theory which explicitly describes all those interaction mechanisms.

The most up-to-date study is that by Todorov [Todorov12], where an approach based on the Power-Zienau-Woolley gauge (also known as *electrical dipole gauge*) is proposed and discussed. That paper develops a solid and very general theory, that can be quite easily adapted to many experimental situations. Here I will specifically consider that theory for the sample geometry shown in Fig. 1.1, that is, the dielectric or metallic slab cavity embedding a finite number of quantum wells, each of them experiencing a different cavity field. With a straightforward generalization, the result is extended to an arbitrarily-shaped cavity, giving a strong theoretical foundation to the formula that was proposed in [Zanotto12] starting from heuristic considerations.

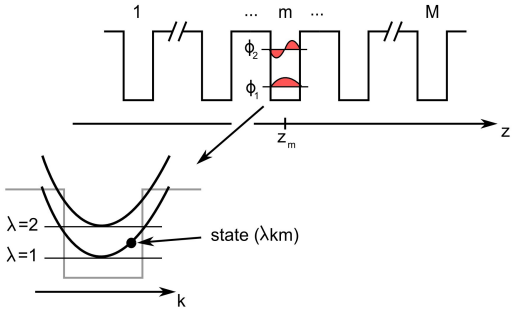


Figure 1.2: Schematics of a two-level, parabolic subband multi-quantum well (MQW).

### 1.3.1 Interaction Hamiltonian in the electrical dipole gauge

The full Hamiltonian of the system is the sum of electronic, photonic and interaction Hamiltonians:

$$\hat{H} = \hat{H}_e + \hat{H}_p + \hat{H}_{int}. \tag{1.9}$$

The electronic term $\hat{H}_e$ describes the electron dynamics in the confining potential, including only the static Hartree interaction term. As it is most convenient to work in second quantization, we introduce a set of fermionic creation and annihilation operators $c^\dagger_{\lambda \mathbf{k} m}$ and $c_{\lambda \mathbf{k} m}$, corresponding to the single-particle states shown in Fig. 1.2. Those states span a complete basis for the multi-quantum well landscape we are interested in, that is, the case of $m = 1 \ldots M$ identical independent two-level quantum wells. The subband index is allowed to assume only the values $\lambda = 1, 2$. With these hypothesis one has

$$\hat{H}_e = \sum_{\lambda \mathbf{k} m} \hbar \omega_\lambda c^\dagger_{\lambda \mathbf{k} m} c_{\lambda \mathbf{k} m}. \tag{1.10}$$

The photonic term $\hat{H}_p$ describes the dynamics of the electromagnetic degrees of freedom of the cavity field, that is, the $E$ and $H$ fields feeling the nondispersive background dielectric whose spatial modulation implements the photon confinement within the waveguide. Starting from the usual expression of the electromagnetic energy density

$$\hat{H}_p = \int \left[ \frac{1}{2\,\varepsilon_0 \varepsilon(z)} \hat{\mathbf{D}}^2 + \frac{\mu_0}{2} \hat{\mathbf{H}}^2 \right] \tag{1.11}$$

and employing the classical field profiles (Eq. 1.8), the conventional quantization procedure of the electromagnetic field leads to

$$\hat{H}_p = \sum_{\mathbf{k}} \hbar\omega_{c\mathbf{k}} \left( a^\dagger_{\mathbf{k}} a_{\mathbf{k}} + \frac{1}{2} \right) \tag{1.12}$$

where $\omega_{c\mathbf{k}}$ is the frequency of the cavity mode at $\mathbf{k}$ in-plane wavevector[6]. The bosonic operators $a^\dagger_{\mathbf{k}}$ and $a_{\mathbf{k}}$ enter in the definition of the quantum field operators. For instance, the component $\hat{\mathbf{D}}_z$ reads

$$\hat{\mathbf{D}}_z(\mathbf{r}, z) = i \sum_{\mathbf{k}} A_{\mathbf{k}}\, \mathbf{e}_z \frac{|\mathbf{k}|}{\omega_{i\mathbf{k}}} f_{\mathbf{k}}(z)\, e^{i\mathbf{k}\cdot\mathbf{r}} \left( a_{\mathbf{k}} - a^\dagger_{-\mathbf{k}} \right) \tag{1.13}$$

where

$$A_{\mathbf{k}} = \sqrt{\frac{\hbar\omega_{c\mathbf{k}}}{2\mu_0 S L_{\mathbf{k}}}} \tag{1.14}$$

is the amplitude of the field corresponding to a single photon propagating within the quantization surface $S$ of the waveguide. The effective length of the electromagnetic mode $L_{\mathbf{k}}$ is connected with the mode profile function normalization by the equation

$$\int_{-\infty}^{+\infty} f^2_{\mathbf{k}}(z)\, dz = L_{\mathbf{k}}. \tag{1.15}$$

The interaction term $\hat{H}_{int}$ describes the interaction of the electrons with the cavity field, and the dynamical Coulomb interaction between the electron themselves:

$$\hat{H}_{int} = \int \frac{1}{\varepsilon_0 \varepsilon(z)} \left[ -\hat{\mathbf{D}} \cdot \hat{\mathbf{P}} + \frac{1}{2} \hat{\mathbf{P}}^2 \right]. \tag{1.16}$$

In this expression the operator $\hat{\mathbf{P}}$ is the quantum analogue of the microscopical average polarization density, usually introduced in the classical treatment of the dielectric properties of condensed matter to describe the contribution of bound charges. Like for $\hat{H}_e$ and $\hat{H}_p$, one seeks for a second-quantized form of $\hat{H}_{int}$ such that the global Hamiltonian has a readily-diagonalizable expression that evidences the nature of fundamental excitations.

[6] In this Section the hypothesis of a single-mode cavity is understood.

### 1.3.2 Polarization operator and bosonized electronic Hamiltonian

To link $\hat{\mathbf{P}}$ with the operators describing the quantum dynamics of electrons, that is, the $c^\dagger$ and $c$ operators introduced above, we observe that

$$\frac{\partial \hat{\mathbf{P}}}{\partial t} = \frac{1}{i\hbar}[\hat{\mathbf{P}}, \hat{H}] = \hat{\mathbf{j}} \tag{1.17}$$

where the equality between the first and the second term is the quantum equation of motion (driven by the *total* Hamiltonian of the system), and the equality between the first and the last terms stems from the definition of microscopical charge current connected to a polarization volume density. Although in principle the $\hat{\mathbf{P}}$ operator has all three spatial components different from zero, from now on we neglect[7] the in-plane components $\hat{P}_{x,y}$.

The operator form for the current is

$$\hat{j}_z = \frac{i\hbar e}{2m^*}[\hat{\Psi}^\dagger \partial_z \hat{\Psi} - \partial_z \hat{\Psi}^\dagger \hat{\Psi}] \tag{1.18}$$

where the field operators can be expressed in terms of the single-particle wavefunctions via

$$\hat{\Psi}(\mathbf{r}, z) = \frac{1}{\sqrt{S}} \sum_{\lambda \mathbf{k} m} c_{\lambda \mathbf{k} m} \phi_{\lambda m} e^{i\mathbf{k}\cdot\mathbf{r}}. \tag{1.19}$$

In the MQW approximation, the wavefunctions are chosen in the localized basis $\phi_{\lambda m} = \phi_\lambda(z - z_m)$, recalling the solutions of the single quantum well given in Sect. 1.1, and Fig. 1.2. By plugging Eq. 1.19 in Eq. 1.18 and performing the summations[8], one gets

$$\hat{j}_z(\mathbf{r}, z) = \frac{i\hbar e}{2m^* S} \sum_{\mathbf{q}} e^{i\mathbf{q}\cdot\mathbf{r}} \sum_m \xi(z - z_m) \left( \tilde{B}_{\mathbf{q}m} - \tilde{B}^\dagger_{-\mathbf{q}m} \right) \tag{1.20}$$

where $\xi$ is the intersubband current localized in the $m$-th QW (Eq. 1.4). Fundamental ingredients of the above expression are the operators

$$\tilde{B}^\dagger_{\mathbf{q}m} = \sum_{\mathbf{k}} c^\dagger_{2,\mathbf{k}+\mathbf{q},m} c_{1\mathbf{k}m} \tag{1.21}$$

[7] In the MQW environment, this means that intrasubband currents are disregarded. This approximation will be briefly discussed in the semiclassical framework of Sect. 1.4.

[8] Special care has to be taken in avoiding to include in Eq. 1.20 null terms, as they will appear in the denominator of subsequent expressions.

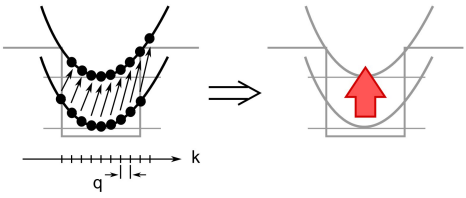


Figure 1.3: Schematic of the action of the collective intersubband excitation $\tilde{B}^{\dagger}_{\mathbf{q}m}$, localized in the $m$-th quantum well.

which describe a coherent superposition of single-particle excited states. Since we started from a single-particle basis whose wavefunctions are delocalized along $x$-$y$ and localized along $z$, those operators behave accordingly: the excitation created by $\tilde{B}^{\dagger}_{\mathbf{q}m}$ is delocalized along $x$-$y$ (a plane wave at fixed $\mathbf{q}$) and localized along $z$ (concentrated in the $m$-th QW); a pictorial representation of this action is given in Fig. 1.3. This behaviour follows from choosing the totally symmetric linear combination in Eq. 1.21. In the literature, these excitations are named *bright excitations*, since – as it will become clearer later – these are the sole states which interact with the microcavity electromagnetic field.

The commutator of the $B$ operators with the electronic Hamiltonian reads[9]

$$[\tilde{B}^{\dagger}_{\mathbf{q}m}, \hat{H}_e] = -\hbar\omega_{12}\tilde{B}^{\dagger}_{\mathbf{q}m} \tag{1.22}$$

under the common hypothesis that the excitation wavevector $\mathbf{q}$ is much smaller than the average electronic wavevectors.

The above formula has a twofold consequence. First, it enables to solve Eq. 1.17 for the polarization operator, which explicitly reads

$$\hat{P}_z(\mathbf{r}, z) = \frac{\hbar e}{2m^* S\omega_{12}} \sum_{\mathbf{q}} e^{i\mathbf{q}\cdot\mathbf{r}} \sum_m \xi(z - z_m) \left(\tilde{B}_{\mathbf{q}m} + \tilde{B}^{\dagger}_{-\mathbf{q}m}\right). \tag{1.23}$$

Furthermore, Eq. 1.22 can be regarded as the emergence of effective bosonic degrees of freedom in the dynamics of the weakly excited electron gas. The full electronic Hamiltonian $\hat{H}_e$ can indeed be replaced by the effective Hamiltonian

$$\hat{H}'_e = \hbar\omega_{12} \sum_{\mathbf{q}m} \tilde{b}^{\dagger}_{\mathbf{q}m}\tilde{b}_{\mathbf{q}m} \tag{1.24}$$

[9] A detailed derivation can be found in [De Liberato09a].

without inficiating the commutator (1.22). Hence, the dynamics of the low-energy excitations of the real Fermi gas can be described as the dynamics of an ensemble of *bosons*[10], each of them contributing with an energy quantum $\hbar\omega_{12}$. The operators $\tilde{b}$'s are obtained by a normalization of the $\tilde{B}$'s: $\tilde{b}^{\dagger}_{\mathbf{q}m} = \tilde{B}^{\dagger}_{\mathbf{q}m}/\sqrt{\Delta N}$, where

$$\sqrt{\Delta N} = \frac{1}{M}\langle F| \sum_{\mathbf{q}m} c^{\dagger}_{1\mathbf{q}m} c_{1\mathbf{q}m} - c^{\dagger}_{2\mathbf{q}m} c_{2\mathbf{q}m} |F\rangle \tag{1.25}$$

is the population difference between the first and second subband in a single quantum well. $|F\rangle$ is the ground state of the electronic system, above which the (collective) single-particle excitation takes place. Usually $|F\rangle$ is the ground thermal state of the Fermi-Dirac statistics, i.e., for sufficiently low doping level, each QW populated up to the Fermi wavevector only in the first subband[11].

### 1.3.3 Electron-photon coupling and the emergence of bright states

In the previous Section, we showed how the electronic Hamiltonian can be simplified by introducing bosonic excitations, and we provided an explicit expression of the polarization operator that enters the interaction Hamiltonian (1.16). Nonetheless, the number of involved degrees of freedom is still very large. From the matter point of view, for example, there are $N \times M$ degrees of freedom corresponding to the choices of $\mathbf{q}$ and $m$ in $\tilde{b}^{\dagger}_{\mathbf{q}m}$. $N$ is a macroscopic number, of the order of the number of electrons in a surface $S$ of the single QW, while $M$ is the number of QWs that can reach $\simeq 100$ in certain devices. While the issue of a macroscopic $N$ is naturally dealt with the translational invariance of the system, the presence of $M$ excitations corresponding to the individual quantum wells has to be resolved in a smarter way. As it will be clear in the following, what occurs is a rearrangement of the excitations that leads to a factor $\sqrt{M}$ in the coupling strength, reminiscent of the superradiance phenomenon introduced by Dicke [Kavokin07].

[10] The procedure used here is actually known as *bosonization*. Indeed, the quasi-bosonic commutation relation $[\tilde{b}_{\mathbf{q}m}, \tilde{b}^{\dagger}_{\mathbf{q}'m'}] \simeq \delta_{\mathbf{q}\mathbf{q}'}\delta_{mm'}$ holds when dealing with weakly excited states [De Liberato09a].

[11] If mid-infrared intersubband transitions are considered, this is true even at room temperature (mid-infrared $\rightarrow \hbar\omega_{12} \simeq 100$ meV $\simeq 4k_BT$). On the contrary, in the terahertz range $\hbar\omega_{12} \simeq 10$ meV this is not true and the temperature can be used as a tuning tool for $\Delta N$.

The idea is to work out the first term of the interaction Hamiltonian (Eq. 1.16), which is linear in the operators $\tilde{b}$:

$$H_{I1} = i\frac{\hbar e}{2m^* S\omega_{12}} \sum_{\mathbf{q}\mathbf{q}'m} A_{\mathbf{q}} \frac{|\mathbf{q}|}{\omega_{c\mathbf{q}}} (a^\dagger_{\mathbf{q}} - a_{-\mathbf{q}})(\tilde{b}^\dagger_{\mathbf{q}'m} + \tilde{b}_{-\mathbf{q}'m}) \times \\ \times \int_S e^{i(\mathbf{q}+\mathbf{q}')\cdot\mathbf{r}} \int_{-\infty}^{\infty} f_{\mathbf{q}}(z)\xi(z - z_m)\, dz \tag{1.26}$$

$$= i\frac{\hbar e}{2m^*\omega_{12}} \sum_{\mathbf{q}m} A_{\mathbf{q}} \frac{|\mathbf{q}|}{\omega_{c\mathbf{q}}} (a^\dagger_{\mathbf{q}} - a_{-\mathbf{q}})(\tilde{b}^\dagger_{-\mathbf{q}m} + \tilde{b}_{\mathbf{q}m}) \times \\ \times f_{\mathbf{q}}(z_m) \int_{-\infty}^{\infty} \xi(z)\, dz. \tag{1.27}$$

where the hypothesis that $f$ varies slowly on the single QW length scale has been assumed.

First, one notices that the presence of the factors $e^{i\mathbf{q}\cdot\mathbf{r}}$ in both $\hat{D}_z$ and $\hat{P}_z$ induces a collapse of the double summation over $\mathbf{q}$ and $\mathbf{q}'$ into a single summation. This means that the optical mode at $\mathbf{q}$ couples *only* to the intersubband excitation at $\mathbf{q}' = \mathbf{q}$, with a strength $S$ proportional to the macroscopic number of involved degrees of freedom. In other words, since both the photonic resonator and the QWs are translationally-invariant, the states of the global system must accomplish translational invariance too, and their labeling by a $\mathbf{q}$ index comes out straightforwardly from the theory. This is what happens for the $xy$ spatial directions – in substance, a normalization. Instead, when dealing with the $z$ direction, a different idea has to be exploited. Here we have $M$ electronic excitations in interaction with *one* photonic excitation, and we wonder whether the interaction can be recast in terms of only *one* "smart" electronic excitation. Indeed, if one defines

$$b^\dagger_{\mathbf{q}\alpha} = \sum_m \gamma_{\alpha m} \tilde{b}^\dagger_{\mathbf{q}m} \tag{1.28}$$

with

$$\gamma_{1m} = \frac{f_{\mathbf{q}}(z_m)}{\sqrt{\sum_{m'} f^2_{\mathbf{q}}(z_{m'})}} \tag{1.29}$$

and the others $\gamma_{\alpha m}$ obtained by an orthonormalization procedure such that

$$\sum_m \gamma_{\alpha m}\gamma_{\alpha' m} = \delta_{\alpha\alpha'},$$

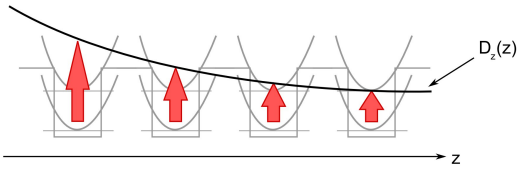


Figure 1.4: Schematic of the action of the bright intersubband excitation $b^{\dagger}_{\mathbf{q}1}$, delocalized along the multi-quantum well and following the amplitude of the displacement field.

the linear interaction Hamiltonian becomes

$$H_{I1} = \sum_{\mathbf{q}} \frac{i\hbar\omega_P}{2} \sqrt{\frac{\omega_{c\mathbf{q}}}{\omega_{12}} f_0 f_w}\, (a^{\dagger}_{\mathbf{q}} - a_{-\mathbf{q}})(b^{\dagger}_{-\mathbf{q}1} + b_{\mathbf{q}1}) \tag{1.30}$$

where we define an overlap factor

$$f_w = \frac{L_{\text{eff}}}{L_{\mathbf{q}}} \frac{\varepsilon_{\text{eff}}}{\varepsilon_w} \sum_m f^2_{\mathbf{q}}(z_m) \tag{1.31}$$

and employed the plasma frequency

$$\omega_P = \sqrt{\frac{e^2 \Delta n}{\varepsilon_0 \varepsilon_w m^* L_{\text{eff}}}} \tag{1.32}$$

pertaining to a two-dimensional electron gas of density $\Delta n = \Delta N / S$ distributed in the quantum well effective thickness $L_{\text{eff}}$ (Eq. 1.6). Here, $\varepsilon_w$ is the permittivity of the quantum well material, $\varepsilon_{\text{eff}}$ is the effective permittivity of the guided mode, and $L_{\mathbf{q}}$ is given by Eq. 1.15.

Equation 1.30 is exactly what we were looking for: the interaction between *one* photonic mode and *one* collective, delocalized intersubband excitation, $b^{\dagger}_{\mathbf{q}1}$. This *bright excitation*, whose action is schematized in Fig. 1.4, brings all the dipole oscillator strength of the system. Its superradiant behaviour clearly appears from (1.31): given the normalization (1.15), the term $\sum_m f^2_{\mathbf{q}}(z_m)$ is of the order of $M$ evidencing that the ensemble of QWs acts as an enhanced collective oscillator.

The above formulas are an exact result applicable to a planar cavity with an arbitrary structure along the QW's growth axis, and they correct a factor given in [Ciuti05] that was evaluated in the traveling-wave

approximation[12]. The two main geometries to which they can be applied are the cavities based on dielectric confinement and on a metal interface (see Fig. 1.1). In these cavities, the inherent field inhomogeneity – especially relevant when there is a large number of QWs placed far from the field maximum – plays a role[13], summarized by Eq. 1.31.

All the results above have been derived rigorously with the assumption that the sample is translationally invariant along two directions. Being one of the aims of this thesis the study of ISB polaritons in photonic crystal slabs (PhCS), a generalization of the previous theory is necessary[14]. A rigorous approach would rely on an analysis similar to that given for exciton-polaritons in [Gerace07], where the bright excitation operators are no more given by Eq. 1.28. Instead, they would be labeled by a Bloch wavevector $\mathbf{K}$ linked to the periodicity in the PhCS, and would consist of a suitable superposition of the $\tilde{b}$ intersubband excitation operators: $b_{\mathbf{K},\alpha} = \sum_{\mathbf{q}m} \gamma_{\mathbf{K},\mathbf{q};\alpha,m} \tilde{b}_{\mathbf{q}m}$. Since virtually any photonic resonator can be thought as a periodic photonic structure – in the sense that a dilute periodic array of identical copies of the resonator will behave as a single, isolated resonator – this framework is capable of describing all the geometries employed for intesubband polariton physics: patch cavity arrays, LC resonators, and split-ring resonators.

Without developing the explicit theory according to the above idea, here we give a general expression for the overlap factor $f_w$. We claim that this formula, which in the translational-invariant case rigorously follows from Eq. 1.31, is the correct expression for the general situation of an arbitrarily-shaped photonic resonator embedding non-interacting QWs. Under the hypothesis of $M$ equispaced QWs, having barrier (well) widths $L_b$ ($L_w$), distributed over a region of thickness $L_{\mathrm{MQW}}$, we have

$$f_w = \frac{ML_{\mathrm{eff}}}{L_{\mathrm{MQW}}} \frac{\int_{\mathrm{MQW}} |E_z|^2 \varepsilon_{\mathrm{MQW}}}{\int |\mathbf{E}|^2 \varepsilon(\mathbf{r}, z)} \equiv \frac{L_{\mathrm{eff}}}{L_b + L_w} \Gamma. \tag{1.33}$$

Here we introduced the *overlap factor* $\Gamma$ which is a ratio between field integrals. The above formula, first reported heuristically in [Zanotto12], and successfully employed in [Feuillet-Palma12], substantially states

[12] In [Ciuti05], equation (9), the factor $\sin\theta$ indicates that the light propagation in the microcavity is understood in the ray-optics limit, and does not correspond to a physical quantity of the microcavity resonant mode.

[13] This was already noticed in [Załużny09], although there the electron-electron interactions were disregarded. Actually, it will turn out that the overlap factor $f_w$ plays a role when the full Hamiltonian is diagonalized.

[14] The generalization to an array of strongly confining patch cavities (*quantum boxes*) is already formalized in [Todorov12].

that the largest $f_w$, and hence the strongest coupling, is attained when the QWs are as close as possible, and fill the region where the electromagnetic mode dwells. Furthermore, the best situation is that in which the field is mostly directed along the $z$ direction.

As a final remark it should be pointed out that the superradiant state $b^\dagger_{\mathbf{q}1}|F\rangle$ is always accompanied by a macroscopic number of single-particle excited states $c^\dagger_{2\mathbf{k}m}c_{1\mathbf{k}'m}|F\rangle$ lying at the same energy. This presence is thought to have a negative influence when electrical pumping of a polaritonic system is involved: as there is no mean for a direct electrical injection of a coherent superposition of single-particle excitations[15], in this class of experiments the overlap between the injected quantum state and the superradiant state can be very small. However, the argument is still under debate, and the development of more complicated population schemes (like the three-level design of [Delteil11]) could make the road towards electrically pumped intersubband polariton light emitters viable.

### 1.3.4 Electron-electron coupling and intersubband plasmons

After the long detour about the nature of bright states, we now move back to the interaction term found in $\hat{H}_{int}$ (Eq. 1.16) which is quadratic in the polarization operators:

$$\hat{H}_{I2} = \sum_{\mathbf{q}\alpha} \frac{\hbar\omega_P^2}{4\omega_{12}} (b_{\mathbf{q}\alpha} + b^\dagger_{-\mathbf{q}\alpha})(b_{-\mathbf{q}\alpha} + b^\dagger_{\mathbf{q}\alpha}) \tag{1.34}$$

This Hamiltonian keeps the different $\alpha$ states decoupled[16], and can be diagonalized together with the electronic effective Hamiltonian (Eq. 1.24)

$$\hat{H}'_e = \hbar\omega_{12} \sum_{\mathbf{q}\alpha} b^\dagger_{\mathbf{q}\alpha} b_{\mathbf{q}\alpha} \tag{1.35}$$

by employing the Bogoljubov transformation

$$p_{\mathbf{q}\alpha} = \frac{\tilde{\omega}_{12} + \omega_{12}}{2\sqrt{\tilde{\omega}_{12}\omega_{12}}} b_{\mathbf{q}\alpha} + \frac{\tilde{\omega}_{12} - \omega_{12}}{2\sqrt{\tilde{\omega}_{12}\omega_{12}}} b^\dagger_{-\mathbf{q}\alpha}. \tag{1.36}$$

[15] The theory given in [Ciuti06] relied on the possibility of such a coherent pumping, and the predicted enhancement of intersubband spontaneous emission is still far from experimental reach.

[16] The same would have been found within the localized excitation basis framework: $\hat{H}_{I2} = \sum_{\mathbf{q}m} \hbar\omega_P^2/4\omega_{12}(\tilde{b}_{\mathbf{q}m} + \tilde{b}^\dagger_{-\mathbf{q}m})(\tilde{b}_{-\mathbf{q}m} + \tilde{b}^\dagger_{\mathbf{q}m})$.

The operators $p$ describe the excitation of an intersubband *plasmon*, that is, an eigenstate of the electronic Hamiltonian which includes the retarded electron-electron interaction. Each $p^\dagger|F\rangle$ state has an energy $\tilde{\omega}_{12} = \sqrt{\omega_{12}^2 + \omega_P^2}$, which is the depolarization-shifted intersubband transition energy.

### 1.3.5 Intersubband polariton states

Up to now we considered separate combinations of the interaction Hamiltonians and electron Hamiltonian, shedding light on the coupling mechanisms with the consequent definition of *bright states* and *intersubband plasmons*. All these components can be finally put together in the total Hamiltonian

$$\hat{H} = \sum_{\mathbf{q}\alpha} \hbar\tilde{\omega}_{12} p^\dagger_{\mathbf{q}\alpha} p_{\mathbf{q}\alpha} + \sum_{\mathbf{q}} \hbar\omega_{c\mathbf{q}} (a^\dagger_{\mathbf{q}} a_{\mathbf{q}} + 1/2) \tag{1.37}$$

$$+ i \sum_{\mathbf{q}} \hbar\Omega_{\mathbf{q}} (a^\dagger_{\mathbf{q}} - a_{-\mathbf{q}})(p^\dagger_{-\mathbf{q}1} + p_{\mathbf{q}1}) \tag{1.38}$$

where the coupling constant is

$$\Omega_{\mathbf{q}} = \frac{\omega_P}{2} \sqrt{\frac{\omega_{c\mathbf{q}}}{\tilde{\omega}_{12}} f_0 f_w}. \tag{1.39}$$

While the states with $\alpha \neq 1$ are decoupled *dark plasmons*, the remaining can be diagonalized by the Hopfield-Bogoljubov transformation

$$\Pi_{\mathbf{q}} = x_{\mathbf{q}} a_{\mathbf{q}} + y_{\mathbf{q}} a^\dagger_{-\mathbf{q}} + z_{\mathbf{q}} p_{\mathbf{q}1} + t_{\mathbf{q}} p^\dagger_{-\mathbf{q}1} \tag{1.40}$$

by requiring that the commutator $[\hat{H}, \Pi_{\mathbf{q}}] = \hbar\omega_{\mathbf{q}}\Pi_{\mathbf{q}}$ is satisfied. The presence of the *creation* operators $a^\dagger$ and $p^\dagger$ in the *destruction* operator $\Pi$ is a sign that we are solving the full Hamiltonian with the non-resonant coupling terms $ap$ and $a^\dagger p^\dagger$; in other words, this approach goes beyond the rotating-wave approximation.

The two real and positive solutions $\omega \equiv \omega_{\mathrm{UP,LP},\mathbf{q}}$ of the secular equations

$$(\omega^2 - \tilde{\omega}_{12}^2)(\omega^2 - \omega_{c\mathbf{q}}^2) = f_0 f_w \omega_P^2 \omega_{c\mathbf{q}}^2 \tag{1.41}$$

are thus the energies of the eigenstates of the coupled system, that is, the polaritons. When dealing with a dispersive cavity, i.e. a cavity whose $\omega_{c\mathbf{q}}$ depends on $\mathbf{q}$ in such a way that $\tilde{\omega}_{12}$ is crossed at a certain

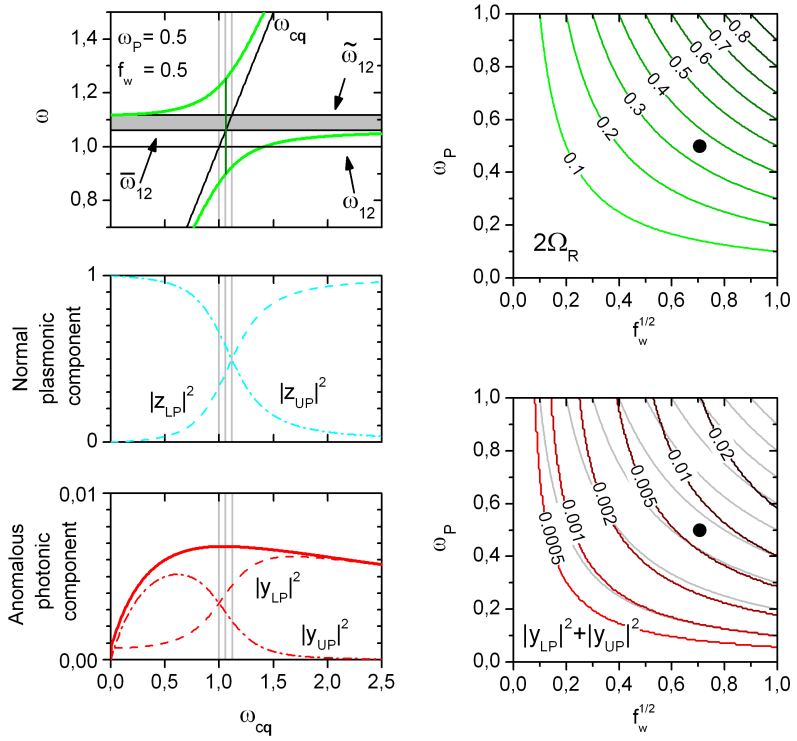


Figure 1.5: *Top left*, ultra-strong coupling polaritonic antocrossing. All the frequencies are normalized to $\omega_{12}$. *Middle and bottom left*, some relevant mixing fractions. The anomalous photonic component $|y_{\rm LP}|^2 + |y_{\rm UP}|^2$ coincides with the number of virtual cavity photons in the polaritonic ground state. Parameters $\omega_P = f_w = 0.5$ have been employed. *Top right*, maximum UP/LP splitting as a function of the parameters. The black dot recalls the parameters used in the left panels. *Bottom right*, number of virtual cavity photons at resonance ($\omega_{c\mathbf{q}} = \omega_{12}$) as a function of the parameters.

point of the $q$ space, one usually refers to the relation $\mathbf{q} \leftrightarrow \omega_{\rm UP,LP,\mathbf{q}}$ as the *polaritonic dispersion relation*.

The main features of the polaritonic dispersion are represented in the upper left panel of Fig. 1.5. There are two anticrossing polaritonic branches, which exhibit horizontal asymptotes at the frequencies $\tilde{\omega}_{12}$ and $\bar{\omega}_{12} = \sqrt{\omega_{12}^2 + \omega_P^2(1 - f_0 f_w)}$. Since $0 < f_0 f_w < 1$, one has $\omega_{12} < \bar{\omega}_{12} < \tilde{\omega}_{12}$, with the consequent formation of a *gap* reminiscent of

the transverse-longitudinal splitting of bulk phonon-polaritons. There are two situations where the gap tends to close and the anticrossing is vanishing: one is when $\omega_P \to 0$, the other when[17] $f_w \to 0$. The first corresponds to the case of very low doping, hence giving rise to a decoupled transition at the non-depolarized frequency $\omega_{12}$. The second corresponds to the case of weak field-QW overlap[18], and the decoupled matter excitation lies at the depolarized frequency $\tilde{\omega}_{12}$.

When the coupling is non-zero, one recognizes three relevant values of the cavity frequency $\omega_{c\mathbf{q}}$, reported as grey vertical lines in Fig. 1.5. When $\omega_{c\mathbf{q}} = \bar{\omega}_{12}$, the UP/LP splitting is minimum and takes the value $\omega_P\sqrt{f_0 f_w}$. This highlights that while usually in the strong-coupling theory there is only one parameter, i.e. the coupling constant (vacuum Rabi frequency) which is identified with the minimum splitting (vacuum Rabi splitting), here there are two independent parameters: $\omega_P$ and $f_w$. While both contribute to increase the mode splitting, their role is different in principle; this has to be kept in mind even when a "Rabi frequency" is defined as the minimum splitting:

$$2\Omega_R = \omega_P\sqrt{f_0 f_w}. \tag{1.42}$$

Going back to the relevant values of the cavity frequency, one notices from Fig. 1.5 that when $\omega_{c\mathbf{q}} = \tilde{\omega}_{12}$ the mixing is maximum (middle left panel), while the anomalous photonic components are equal when $\omega_{c\mathbf{q}} = \omega_{12}$. The anomalous photonic components $|y_{\mathrm{UP,LP}}|^2$ deserve a special interest, since they are linked to the number of *virtual photons* contained in the vacuum polariton states. As [Ciuti05] reports, given the ground $\mathbf{q}$-polaritonic state $|G_{\mathbf{q}}\rangle$ (that is, the state satisfying $\Pi_{\mathrm{UP},\mathbf{q}}|G_{\mathbf{q}}\rangle = \Pi_{\mathrm{LP},\mathbf{q}}|G_{\mathbf{q}}\rangle = 0$), the expectation value of the cavity photon number in the mode $\mathbf{q}$ is given by

$$\langle G_{\mathbf{q}}|a^\dagger_{\mathbf{q}}a_{\mathbf{q}}|G_{\mathbf{q}}\rangle = |y_{\mathrm{LP}}|^2 + |y_{\mathrm{UP}}|^2. \tag{1.43}$$

As clearly appears in the bottom left panel of Fig. 1.5, the *global* contribution from the $|y|^2$ is broadly distributed around the anticrossing region; this quite counterintuitive behaviour could be exploited while designing an experiment of vacuum photon generation and detection (see Sect. 4.2.2).

[17] In this formalism $f_0 \neq 0$ since we are implicitly considering an active transition.

[18] It may appear that this case describes the multipass QW absorption experiment. Indeed, what really happens in that case is the *complete absence* of a cavity mode, or the strong detuning between the cavity mode and the transition. The latter case corresponds to the empty dots of Fig. 1.6.

The different role of $\omega_P$ and $f_w$ emerges from the right panels of Fig. 1.5. In the upper right panel we report the minimum splitting $2\Omega_R$ as a function of the fundamental parameters; it is clear that $\omega_P$ and $\sqrt{f_w}$ play a symmetric role. This is not true when considering the vacuum photon number $|y_{\mathrm{LP}}|^2 + |y_{\mathrm{UP}}|^2$ reported in the lower right panel: the asymmetry is evidenced by the mismatch between red and grey curves, where the latter retrace the green curves of the upper right panel. Anyway, the difference is small and a large splitting is surely connected to a non-negligible vacuum photon content in the polariton ground state.

As a final remark of this Section, it should be highlighted that equation 1.41 is the main tool for interpreting experimental data within the quantum theory framework. For example, if one knows $f_0$, $f_w$, $L_{\mathrm{eff}}$ and $\omega_{c\mathbf{q}}$ from first-principle calculations, the measured polariton dispersion leads to an accurate determination of $\tilde{\omega}_{12}$ and $\Delta n$, which are quite easily affected by uncertainties in the epitaxial growth process. This analysis is straightforward when dealing with a planar metal-dielectric cavity, where the polaritons appear as clear dips in the ATR spectrum of a prism-shaped sample – contrary to what happens in certain photonic crystal (PhC) samples (Sect. 3.2.2). It is actually the interpretation of the spectra measured on these PhC samples that motivated us to first repeat the basic intersubband polariton experiment [Dini03] on the heterostrucure HM 3014, whose details are given in Sect. 3.2.2. In Fig. 1.6 we report as dots the measured dip energies in the energy-wavevector diagram, together with the fitting curves from Eq. 1.41. The bare photonic mode dispersion $\omega_{c\mathbf{q}}$ has been calculated by means of the transfer-matrix formalism [Born99]; from the same calculations we obtained the field overlap factor $f_w$. Notice the difference between the true overlap factor and that obtained in the travelling wave approximation (see footnote 12). Employing the parameters $\Delta n = (5 \pm 0.3) \cdot 10^{11}\mathrm{cm}^{-2}$ and $\tilde{\omega}_{12} = 124.4 \pm 1$ meV extracted from the present data gives very good agreement with the spectra measured on the PhC samples (see Fig. 3.15). It should be noticed that the ability to correctly estimate $\tilde{\omega}_{12}$ relied on the analysis of *two* prism samples, one cut at 68° and the other at 45°. While from the first one the true polaritonic resonances have been measured (filled dots in Fig. 1.6), from the second one the flat part of the upper polariton dispersion is retrieved, hence giving a closer access to $\tilde{\omega}_{12}$. Actually, this is nothing else than the ordinary multipass absorption experiment: a spectrum is reported in the inset of Fig. 1.6. From the spectrum, the intersubband

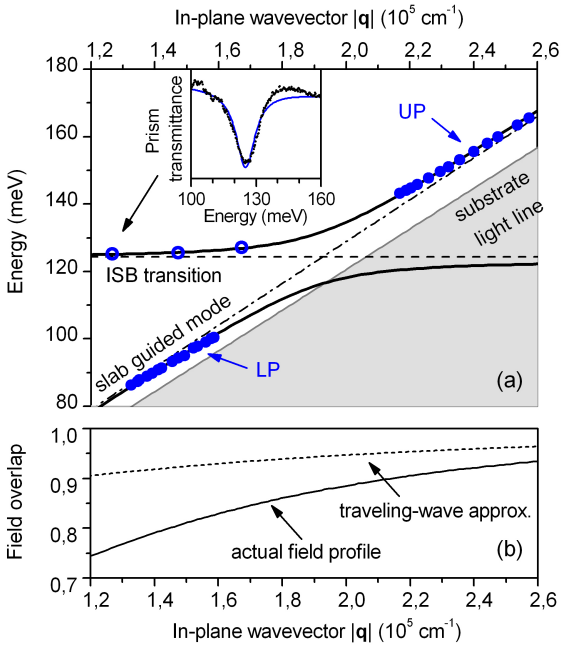


Figure 1.6: Polaritonic dispersion in a planar metal-dielectric waveguide, observed by means of attenuated total reflectance (ATR) in a prism-shaped sample. The filled dots have been obtained from a prism cut at 68°, while the empty dots at 45°. In the lower panel we report the overlap $\Gamma$ factor that enters Eq. 1.33.

transition linewidth $\gamma_{12}$ can be measured as well, hence allowing to experimentally determine the relaxation rate whose relevant role – that goes beyond the Hamiltonian theory – will be highlighted in Chapter 2.

## 1.4 Semiclassical treatment of intersubband polaritons

Since our world is quantum in nature, the Hamiltonian treatment introduced in the previous Section is a building block of unique relevance for the understanding of many physical aspects, like the presence of virtual photons in the polariton ground state or the *ab initio* description of particle-particle interactions. However, it retains the weaknesses of

a non-dissipative theory: it describes the *states* without giving a complete picture about how they couple to the external world. If one designs an optical experiment, it is of great importance to know how the fundamental excitations of the system appear in the practically accessible quantities, like transmittance, reflectance, electro- or photoluminescence...

Moreover, the problem has a more fundamental aspect: when the interaction with external, dissipative degrees of freedom is involved, the very nature of the states of the system can be radically modified; this idea will be detailed in the next Chapter, when introducing the transition between the strong and the weak coupling regimes. If one looks for a natural evolution of the energy-conserving Hamiltonian formalism, the answer is the quantum master equation formalism. With reference to semiconductors in strong coupling, one can refer to a work on the archetypical Jaynes-Cummings model of a two-level quantum dot coupled to a three-dimensional resonator [Andreani99]; for the case of intersubband transitions in planar cavities one should instead refer to [Ciuti06, De Liberato08, De Liberato09b].

If somebody's interest is limited to the analysis of polaritonic dispersion and lineshapes, it turns out however that classical electromagnetism supported by a local and linear response theory provides correct answers. Within this framework, dissipation mechanisms are easily kept into account: non-radiative channels are included "by hand" as an imaginary part in the dielectric constants, and radiative losses are intrinsically described via the coupling with the far-field. Furthermore, the task of describing a realistic sample configuration – also in the photonic crystal slab case – can be afforded thanks to the abundance of methods devoted to the numerical solution of the Maxwell equations in more or less specific geometries.

### 1.4.1 Effective medium dielectric function of a multi-quantum well

The mid-infrared optical response of a quantum well stack is governed by intersubband and intrasubband transitions. It has been shown [Załużny99] that the MQW behaves as an anisotropic dispersive dielectric, with Lorentz- and Drude-like frequency dependences respectively corresponding to inter- and intrasubband electronic excitations. This linear and local response theory, which stems from the spatial averaging of the localized currents in the wells over the MQW period, leads

to explicit formulas for the dielectric tensor:

$$\begin{aligned} \varepsilon_{x,y}(\omega) &= \varepsilon\left[1-\frac{\bar{\omega}_P^2}{\omega(\omega+i\gamma_{\|})}\right] \\ \varepsilon_z(\omega) &= \varepsilon\left[1-f_0\frac{\varepsilon^2}{\varepsilon_w^2}\frac{\bar{\omega}_P^2}{\tilde{\omega}_{12}^2-\omega^2-2\,i\omega\gamma_{12}}\right]^{-1}. \end{aligned} \tag{1.44}$$

The strength of Drude- and Lorentz-like terms is governed by a plasma frequency which corresponds to the *average volume charge density*[19] in the MQW:

$$\bar{\omega}_P=\sqrt{\frac{e^2\Delta n}{\varepsilon_0\varepsilon m^*(L_b+L_w)}}.$$

With $\varepsilon$ we refer to the average background permittivity[20], while $\varepsilon_w$ is the dielectric constant in the well material. Damping of both intra- and intersubband currents is described by the rates $\gamma_{\|}$ and $\gamma_{12}$.

If one looks at typical values of the plasma frequency $\bar{\omega}_P \leq 50$ meV and of the damping rates ($\gamma_{\|} \simeq 5$ meV), it turns out that in the mid-infrared $\varepsilon_{x,y}$ is very close to the bulk value. For this reason, in all the numerical simulations we neglected the Drude contribution; in addition, this justifies *a posteriori* that the in-plane currents have been disregarded in the Hamiltonian treatment (Sect. 1.3.2). On the contrary, $\varepsilon_z$ has a strong dispersion and its imaginary part is close to a Lorentzian with full width at half maximum equal to $2\gamma_{12}$, and peak amplitude proportional to $\Delta n/\gamma_{12}$. Since the absorbance $\alpha$ is proportional to $\mathrm{Im}(\varepsilon)$, this Lorentzian lineshape is observed in a single- or multipass absorption experiment, which hence provides a tool to estimate the charge density and the damping rate.

We will now show that this result is fully compatible with the quantum treatment given in the previous Section. Indeed, let's consider the double-metal geometry [Fig. 1.1 (b)], whose fundamental mode (the TEM mode) has the electric field perfectly aligned along the $z$ direction and an effective modal permittivity equal to the bulk permittivity of the material embedded between the (perfect) metal plates. If this

[19] Recall that the coupling constant of the Hamiltonian theory involves the *surface charge density* (Eqs. 1.32 and 1.39).

[20] More precisely, two different averaging schemes should be employed for the $\varepsilon$ appearing in $\varepsilon_{x,y}(\omega)$ and $\varepsilon_z(\omega)$. However, if barrier and well permittivities are close to each other – as it is the case of the GaAs/$Al_{0.33}Ga_{0.67}$As system – this difference can be neglected, and the usual $\varepsilon=(L_b\varepsilon_b+L_w\varepsilon_w)/(L_b+L_w)$ can be employed.

material happens to be a MQW stack, its permittivity is given by the $\varepsilon_z(\omega)$ in (1.44), and the dispersion relation of the double-metal waveguide is

$$\varepsilon_z(\omega)\frac{\omega_{\mathbf{q}}^2}{c^2} = |\mathbf{q}|^2. \tag{1.45}$$

The specific $\omega$-dependence of $\varepsilon_z(\omega)$ implies that the above equation has two solutions for each $|\mathbf{q}|$, which coincide[21] with the upper and lower polariton roots of the secular equation (1.41). Clearly, in this comparison the intersubband damping $\gamma_{12}$ has to be set to zero. This equality is a further confirmation that the quantum and the semiclassical treatments are fully compatible and complementary: they give rise to the same dispersion, while giving insight – respectively – into the quantum nature of the polaritonic states, and into the influence of losses and geometry. Strictly speaking, in the comparison given above the radiative losses did not enter at all, and the geometry was a very special one. However, the effective dielectric approach will be extensively used for intersubband polaritons in photonic crystal slabs, and it will turn out that its predictions are really accurate.

## 1.5 Conclusions

In conclusion, we outlined the quantum theory of intersubband polaritons in a photonic cavity, highlighting the role of field inhomogeneity across the resonant cavity, with the attendant emergence of a bright excitation and the need for an optimal overlap between the guided mode field profile and the multi-quantum well. We started from the formalism of [Todorov12], and obtained the specific forms for the overlap factors in Eq. 1.31 and 1.33. Since both electron-electron interactions and antiresonant terms are included in the theory, the phenomena known as *depolarization shift* and *vacuum photons in the polaritonic ground state* are described in the most general theoretical framework.

[21] The equality is rigorous provided that – according to what has been assumed in the Hamiltonian analysis – the background permittivity mismatch between barrier and well material is neglected.

# Chapter 2

# Coupled-mode theory of strongly coupled resonators

*Coupled-mode theory* is a general terminology which refers to the wealth of physical situations where the concept of *mode* can be applied. For instance, in the field of photonics for optical communications the analysis of *co-* and *contra-directional coupling* in terms of temporal coupled-mode theory is well known in the study of the crosstalk between different *propagating* modes of an optical waveguide.

Another relevant physical situation is that in which one *propagating* mode couples with a *resonant* mode; it is indeed this coupling that makes it possible to directly probe any resonant mode of whatever system. In the field of photonics the model can be found in textbooks, with direct reference to the coupling between an optical beam and a double-mirror cavity (with the laser cavity in mind [Haus84]), to the optical fiber – microring resonator system [Cai00], or to the coupling between plane waves (diffraction orders) and the resonant mode of a photonic crystal slab [Fan03].

Being the geometry of the system analyzed in [Fan03] very similar to that of our intersubband polaritonic photonic crystals, and being that formalism easily generalizable, here we propose an analogous model in which a further *resonant* degree of freedom is added to the already existent *resonant photonic mode*. The additional degree of freedom, coupled with the resonant photonic mode, and in turn with the

propagating photonic modes (plane waves), reproduces a material excitation like the electronic transition of a two-level quantum system. Although the two-level system we have in mind is the intersubband transition, the model itself is very general, and gives significant insights into the phenomenology of light-matter coupling in both the strong coupling and weak coupling regimes.

In the literature, similar models can be found in [Auffèves-Garnier07, Srinivasan07, Shen09a, Shen09b, Shen10]. There, the resonator geometry is a microdisk or a microring resonator[1], and the fields are treated in their fully quantum nature. However, if one focuses on the response of the quantum system to a classical input state of the light, weak enough to avoid significant population of the excited matter state, a classical model where the two-level system – either fermionic or bosonic – is replaced by a harmonic oscillator indeed gives the same results.

Hence, limiting ourselves to the semiclassical regime, one could expect that we are going to draw the same conclusions of the above cited works. In the following, however, we will mainly focus on the *absorption* properties of our system, a topic usually disregarded in the literature about quantum cavity electrodynamics. In summary, given a limited set of parameters (the radiative and non-radiative damping rates, and the light-matter coupling constant) we are going to extend the concept of *critical coupling* from the *weak coupling* to the *strong coupling* framework; in other words, when a certain damping rate matching occurs, complete energy transfer from the propagating waves into the polariton states is achieved. The *strong critical coupling* is hence different from the *quantum critical coupling* introduced in [Shen10], where the authors study the drop to zero of the transmittance in a polaritonic system. Its relevance stems from the basic need of an efficient mechanism for populating a polariton state, when certain scattering experiments involving intersubband polaritons are designed [De Liberato09c, De Liberato13].

Besides the concept of *strong critical coupling*, the other key concept deduced from the model is the *polaritonic coherent perfect absorption* (CPA). Indeed, when a double-sided cavity is analyzed, the critical coupling appears to be strictly connected to CPA [Chong10], either in the weak coupling and in the strong coupling frameworks. This strik-

[1] In ring and disk resonators one has to deal with quasi-degenerate *clockwise* and *counterclockwise* resonant modes, while in our photonic crystal case we assume the presence of an isolated photonic resonance.

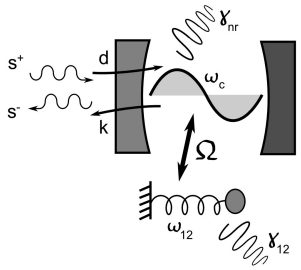


Figure 2.1: Scheme of the one-port photonic cavity. The photonic mode is coupled to the scattering channels via the coupling constants $d$ and $\kappa$, connected to the radiative decay rate $\gamma_r$ (see text).

ing phenomenon, which consists in tuning the polaritonic absorbance by means of the phase of an input beam, is detailed in Sect. 2.2.2 and will be experimentally confirmed in Sect. 3.1.5.

Besides these main results, we figured out that in a two-port resonator the lineshapes occurring in reflectance and in transmittance in the strong coupling regime are linked to the bare resonator lineshape, hence leading to the *lineshape inheritance* concept (Sect. 2.2.1), which enabled to fully understand certain experimental spectra that have been observed during the thesis work (Sect. 3.2.2).

## 2.1 Formalism for the one-port system

The prototypical situation we are going to study is sketched in Fig. 2.1. It consists of one scattering channel, one photonic resonator and one matter resonator. The photonic resonator we have in mind is either a planar waveguide coupled by attenuated total reflectance, or a metal-insulator-metal photonic crystal slab resonator; this is naturally coupled to the free space plane waves, which constitute the scattering channel[2]. The matter resonator, i.e. the two-level system, is represented by a charged oscillator, and is directly coupled to the photonic resonator via the coupling constant $\Omega$.

The dynamics of the system is described by the following equa-

[2]Although the free space plane waves contitute a continuum of scattering channels, thanks to translational invariance only one pair incident/outgoing plane wave is connected at a time. In the case of a photonic crystal resonator, the absence of open diffraction channels is assumed.

tions:

$$\begin{aligned} \frac{db}{dt} &= (i\omega_{12} - \gamma_{12})b + i\Omega a \\ \frac{da}{dt} &= (i\omega_c - \gamma_c)a + i\Omega b + \kappa s^+ \\ s^- &= cs^+ + ad \end{aligned} \tag{2.1}$$

where $s^\pm$, $a$, and $b$ is a set of complex, time-dependend coordinates, respectively describing the input/output channels, the photonic resonance, and the matter resonance. They are defined such that

- $|s^\pm|^2$ is the energy flux per unit time ingoing (outgoing) into (out of) the system
- $|a|^2$ is the total electromagnetic energy stored in the cavity
- $|b|^2$ is the total energy stored in the matter resonator.

The photonic resonator is driven from the input scattering channel through the complex amplitude $\kappa$, and radiates into the output channel through $d$. The non-resonant scattering amplitude is given by $c$. The free evolution of the uncoupled and undriven ($\Omega = 0$, $s^+ = 0$) two-level system and resonant cavity is that of damped resonators with energy damping rate respectively equal to $2\gamma_{12}$ and $2\gamma_c$.

The damping rate $\gamma_c$ corresponds to the *total* losses of the *bare cavity*, which we will separate in the sum of two contributions: $\gamma_c = \gamma_r + \gamma_{nr}$. The first is the main *radiative* mechanism, i.e. the cavity leaks into the scattering channel. The second is the sum of all the other mechanisms, either *non-radiative* (like absorption by free carriers or metallic components), or *radiative* (like the scattering into channels different from the "main" one: roughness scattering, diffraction losses ...). What matters is that these mechanisms must be *non-resonant*, i.e. their entity must depend very slowly on the energy scale given by the overall width of the cavity mode. An algebraic manipulation will then link the radiative damping rate $\gamma_r$ to the coupling constants $d$ and $k$. Given the meaning of $s^\pm$, $a$, and $b$, one would expect that the following instantaneous energy conservation equation holds:

$$|s^+|^2 - |s^-|^2 = 2\gamma_{12}|b|^2 + 2\gamma_{nr}|a|^2 + \frac{d|b|^2}{dt} + \frac{d|a|^2}{dt}. \tag{2.2}$$

By differentiating $d|a|^2/dt = a^*\ da/dt + a\ da^*/dt$ (and similarly with $b$), and employing Eq. 2.1, it can be shown that the above energy bal-

ance is fulfilled when the coupling constants are chosen such that

$$\begin{aligned} \kappa = d &= -ie^{i\phi/2}\sqrt{2\gamma_r} \\ c &= e^{i\phi}. \end{aligned} \tag{2.3}$$

Hence, the system is fully described in terms of six real parameters: the bare resonance frequencies $\omega_{12}$ and $\omega_c$, the damping rates $\gamma_{12}$, $\gamma_r$ and $\gamma_{nr}$, and the phase $\phi$.

We now move to the study of the driven system, i.e. the situation where the ingoing scattering channel is populated by a harmonically time-dependent amplitude $s^+ = s_0^+ e^{i\omega t}$; thanks to the linearity of Eq. 2.1, in the steady-state the system has a response at the same frequency $\omega$. In particular, the outgoing channel will be populated by an amplitude $s^- = s_0^- e^{i\omega t}$ given by the relation

$$s_0^- = s_0^+ \left( e^{i\phi} + e^{i\phi} \frac{i(\omega - \omega_{12}) + \gamma_{12}}{(\omega - \omega_+)(\omega - \omega_-)} 2\gamma_r \right) \tag{2.4}$$

with the consequent definition of the *reflection amplitude*

$$r(\omega) = \frac{s_0^-}{s_0^+} = e^{i\phi} \frac{(\omega - \bar{\omega}_+)(\omega - \bar{\omega}_-)}{(\omega - \omega_+)(\omega - \omega_-)}. \tag{2.5}$$

Under the simplifying hypothesis that the cavity is tuned at the two-level system resonance frequency, i.e. $\omega_{12} = \omega_c \equiv \omega_0$, the above expression has two zeroes and two poles occurring at

$$\begin{aligned} \bar{\omega}_\pm &= \omega_0 + \frac{1}{2}\left[ i(-\gamma_r + \gamma_{nr} + \gamma_{12}) \pm \sqrt{4\Omega^2 - (\gamma_r - \gamma_{nr} + \gamma_{12})^2} \right] \\ \omega_\pm &= \omega_0 + \frac{1}{2}\left[ i(\gamma_r + \gamma_{nr} + \gamma_{12}) \pm \sqrt{4\Omega^2 - (\gamma_r + \gamma_{nr} - \gamma_{12})^2} \right]. \end{aligned} \tag{2.6}$$

In usual experiments, the relevant quantity is the *reflectivity* $R_{1\text{port}}(\omega) \equiv |r(\omega)|^2$, hence the phase $\phi$ does not play any role. The reflectivity function $R_{1\text{port}}(\omega)$, and its directly connected absorbance $A_{1\text{port}}(\omega) = 1 - R_{1\text{port}}(\omega)$, play a central role not only in the present one-port theory but also in the two-port theory detailed in the next Section. For this reason we report the explicit expression:

$$A_{1\text{port}}(\omega) = 4\gamma_r \frac{(\Delta^2 + \gamma_{12}^2)\gamma_{nr} + \gamma_{12}\Omega^2}{\Delta^4 + \Delta^2(\gamma_c^2 + \gamma_{12}^2 - 2\Omega^2) + (\Omega^2 + \gamma_c\gamma_{12})^2} \tag{2.7}$$

where $\Delta = (\omega - \omega_0)$.

In the following we will analyze the meaning of the poles and of the zeroes of the reflection amplitude, the latter being coincident to the frequencies of unity absorbance.

### 2.1.1 Strong and weak coupling. Connection to the Purcell effect

Coming back to the coupled case ($\Omega \neq 0$), we will now analyse the behaviour of the poles ($\omega_\pm$) given in Eq. 2.6. As usual for linear systems, we interpret the complex poles as damped eigenfrequencies of the free-decaying modes of the global system. Two main cases can be recognized, depending on the sign of the real quantity under the square root:

$$2\Omega \gg |\gamma_r + \gamma_{nr} - \gamma_{12}| \quad \rightarrow \quad \text{strong coupling regime} \tag{2.8}$$

$$2\Omega \ll |\gamma_r + \gamma_{nr} - \gamma_{12}| \quad \rightarrow \quad \text{weak coupling regime.} \tag{2.9}$$

In the first case, one has

$$\omega_\pm \simeq \omega_0 + i\frac{\gamma_r + \gamma_{nr} + \gamma_{12}}{2} \pm \Omega \tag{2.10}$$

that is, two modes split by $2\Omega$ and having a damping which is the average of the cavity and matter damping rates. This splitting[3] is an evidence of the same physics appearing in the microscopic Hamiltonian treatment given in Chapter 1, with additional informations on the damping but also with the lack of any direct insight into the microscopic nature of the coupling constant $\Omega$. However, in the following, we will discuss some elements that induce a unifying vision of coupled-mode and quantum theories.

Let us now consider the weak coupling case. Under the additional hypothesis $\gamma_c \gg \gamma_{12}$ (recall that $\gamma_c = \gamma_r + \gamma_{nr}$ is the cavity total decay

[3]The condition for observing a splitting in the real part of the poles is in general less demanding than the condition for observing a splitting in the spectral response functions (reflectance, transmittance, absorbance, luminescence...). Indeed, one can have a real part splitting between $\omega_\pm$ thanks to the damping rate matching $\gamma_r + \gamma_{nr} = \gamma_{12}$ together with a large pole imaginary part $\gamma_r + \gamma_{nr} + \gamma_{12}$.

rate)[4], the eigenfrequencies are

$$\omega_+ \simeq \omega_0 + i\gamma_c \tag{2.11}$$

$$\omega_- \simeq \omega_0 + i\left(\gamma_{12} + \frac{\Omega^2}{\gamma_c}\right). \tag{2.12}$$

The pole given by $\omega_+$ represents the bare cavity resonance, while that given by $\omega_-$ represents the two-level system dressed by the cavity resonance [Andreani99]. Its decay rate has an intrinsic non-radiative contribution $\gamma_{12}$, and an additional contribution $\Omega^2/\gamma_c$ that can be interpreted as a modified spontaneous emission rate. Indeed, if one writes $2\Omega^2/\gamma_c = \gamma_{SE}$, where $\gamma_{SE}$ is the spontaneous emission rate[5] given by the Purcell effect formula $\gamma_{SE} = \gamma_0 F_P$, and recalling the expressions

$$\gamma_0 = \frac{1}{3}\frac{\sqrt{\varepsilon}}{\pi\varepsilon_0}\frac{e^2 z_{12}^2 \omega_0^3}{\hbar c^3}$$

and

$$F_P = \frac{3}{4\pi^2}\left(\frac{\lambda_0}{\sqrt{\varepsilon}}\right)^3 \frac{Q}{\tilde{V}},$$

one obtains for the phenomenological coupling constant $\Omega$ exactly the quantum expression for the dipole – electric field coupling energy:

$$\Omega^2 = |\langle \mathbf{d}\cdot\mathbf{E}\rangle|^2 = \frac{1}{4\pi\varepsilon_0}\frac{\pi e^2 f_0}{\varepsilon m \tilde{V}}. \tag{2.13}$$

This expression is valid for a single quantum emitter placed at a location $\mathbf{r}_0$ where the electric field[6] is such that $|\mathbf{E}(\mathbf{r}_0)|^2 = 1/\tilde{V}$. When an assembly of $N$ quantum emitters is considered, the superradiance-induced coupling between the emitters leads to an increase in the coupling constant quantified by $\sqrt{N}$. If the electric field profile is constant and fully confined in a volume $V$ where the emitters are embedded, the substitution $1/\tilde{V} \rightarrow N/V \equiv n_{3d}$ has hence to be made. In the intersubband polariton framework, this hypotesis on the electric field profile is satisfied when referring to a metal-insulator-metal waveguide, and the above expression for $\Omega$ should be compared with (1.33) and (1.42) with an overlap factor $\Gamma = 1$. The comparison leads to full

[4]This approximation can for sure be applied to certain single quantum dot/photonic resonator systems, where the Purcell spontaneous emission rate enhancement has been observed.

[5]Note the factor 2 recalling that in this coupled mode theory the decay rates $\gamma$ refer to the amplitude and not to the energy.

[6]Usual normalization $\int |\mathbf{E}|^2\varepsilon = 1$ is assumed.

matching of the expressions; hence – apart from the issue of antiresonant terms and electron-electron interaction – the Hamiltonian theory (Sect. 1.3) is compatible with the present coupled mode theory. Recalling the consistency of the Hamiltonian theory with the effective dielectric approach (Sect. 1.4) it turns out that we have three consistent and complementary methods for the study of light-matter coupling from different points of view.

### 2.1.2 Critical coupling

We now move our attention from the *poles* to the *zeroes* of the response function $r(\omega)$. If such a zero occurs at *real* $\omega$'s, the reflectance drops to zero and all the energy radiated towards the system is absorbed by the system itself. The physics is basically that of impedance matching, and in the photonics community this is one of the situations referred to as *critical coupling* [Haus84].

The absorption mechanism involved in this definition is a non-resonant loss mechanism, like roughness scattering in disk or ring resonators [Cai00], carrier excitation in the active region of a detector or of a solar cell [Rosenberg10, Yu12], or finally ohmic losses in a bolometric device [Kats12]. Within our formalization of the coupled-mode theory, these examples correspond to decoupling the cavity from the losses induced by the resonant two-level system, i.e. setting $\Omega = 0$.

Under this condition, the reflection amplitude becomes

$$r(\omega) = e^{i\phi} \frac{i(\omega - \omega_0) + \gamma_{nr} - \gamma_r}{i(\omega - \omega_0) + \gamma_{nr} + \gamma_r} \tag{2.14}$$

with a real zero occurring at $\omega_0$ when $\gamma_r = \gamma_{nr}$. The corresponding reflectance is a reversed Lorentzian, with FWHM equal to $2(\gamma_r + \gamma_{nr})$, i.e. the global damping rate of the cavity:

$$R_{1\text{port},\,\Omega=0}(\omega) = \frac{(\omega - \omega_0)^2 + (\gamma_{nr} - \gamma_r)^2}{(\omega - \omega_0)^2 + (\gamma_{nr} + \gamma_r)^2}. \tag{2.15}$$

A set of sample curves are given in Fig. 2.2, where the transition across the critical coupling is evidenced. Usually, the regions $\gamma_r < \gamma_{nr}$ ($\gamma_r > \gamma_{nr}$) are referred to as under- (over-) coupling.

In Sect. 3.3.1 we will show how to tune the $\gamma_r$ of a MIM photonic crystal, in a way such that $\gamma_{nr}$ is substantially unaffected and the transition through under-, critical-, and over-coupling is clearly recognized.

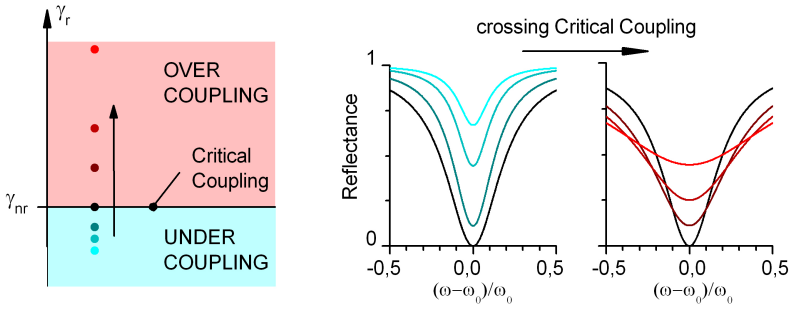


Figure 2.2: Undercoupling, critical coupling, and overcoupling, when no coupling to the matter oscillator is assumed ($\Omega = 0$). When the radiative losses $\gamma_r$ equal the non-radiative, non-resonant losses $\gamma_{nr}$, the reflectance has a zero. The curves are calculated for $\gamma_{nr} = 0.1\ \omega_0$.

### 2.1.3 Strong critical coupling

Given the concepts of *strong coupling* and *critical coupling* introduced above, one may now wonder whether these two situations are compatible or not. The idea is to check whether the zeroes $\bar{\omega}_\pm$ of the full reflection amplitude (see Eqs. 2.5 and 2.6) can lie on the real axis. Depending on the sign of the square root argument, two separate cases are recognized:

- Two real zeroes: **strong critical coupling.**

  The zeroes occur at

  $$\omega_0 \pm \sqrt{\Omega^2 - \gamma_{12}^2}$$

  when

  $$\begin{cases} \gamma_r &= \gamma_{nr} + \gamma_{12} \\ \gamma_{12} &< \Omega \end{cases} \tag{2.16}$$

- One real zero: **weak critical coupling.**

  The zero occurs at

  $$\omega_0$$

  when

  $$\gamma_{12}(\gamma_r - \gamma_{nr}) = \Omega^2. \tag{2.17}$$

We named the first case *strong critical coupling* because of the co-presence of splitting and reflectance zeroes. In this situation, all the incoming energy is absorbed from both the matter oscillator and the non-resonant channels. The further condition $\gamma_{nr} = 0$ would eliminate the latter dissipation mechanism, and the above condition acquires the full meaning of critical coupling into polariton states.

In the second case we applied the nomenclature *weak critical coupling*, since under the decoupling hypothesis $\Omega = 0$ one recovers the usual critical coupling requirement $\gamma_r = \gamma_{nr}$, independently of the presence of the two-level system.

An overview on these cases is given in Fig. 2.3, where a "phase diagram" generalizes to the present framework the critical coupling chart given in Fig. 2.2. A set of spectra, corresponding to the points reported in the chart on the left, are given in the right panels, evidencing the crossing of strong and weak critical coupling conditions. In addition to the reflectance zeroes, one may notice the collapse of the splitting between reflectance minima that occurs upon certain values of the parameters. The place in the parameter space where this collapse occurs is reported as a dashed line in the "phase diagram", and corresponds to the following condition:

$$\gamma_r^2 = \Omega^2 \left( \frac{\gamma_{nr}}{\gamma_{12}} + 2 \right) - \frac{\gamma_{nr}\gamma_{12}^3}{\Omega^2} + \gamma_{nr}^2 - \gamma_{12}^2 + 2\gamma_{nr}\gamma_{12}.$$

This is a somewhat involved expression, that upon the hypothesis of zero non-resonant losses $\gamma_{nr} = 0$ reduces to the simpler cirumference formula

$$\gamma_r^2 + \gamma_{12}^2 = 2\Omega^2.$$

The above hypothesis $\gamma_{nr} = 0$ also simplifies the weak critical coupling condition (Eq. 2.17) to

$$\frac{\Omega^2}{\gamma_r \gamma_{12}} = 1$$

which is a condition on the cooperativity $C = \Omega^2/2\gamma_r\gamma_{12} = 1/2$.

In conclusion, the main result of this simple model is the prediction of a condition upon which all the energy is coupled into polaritonic states. While the presence of a coupling constant that is large compared to all the damping rates guarantees to enter the strong coupling regime, a mismatch between radiative and matter damping rates leads to a scarce coupling efficiency. On one hand, this means scarce contrast in the reflectance spectra, and hence possibly difficult readout

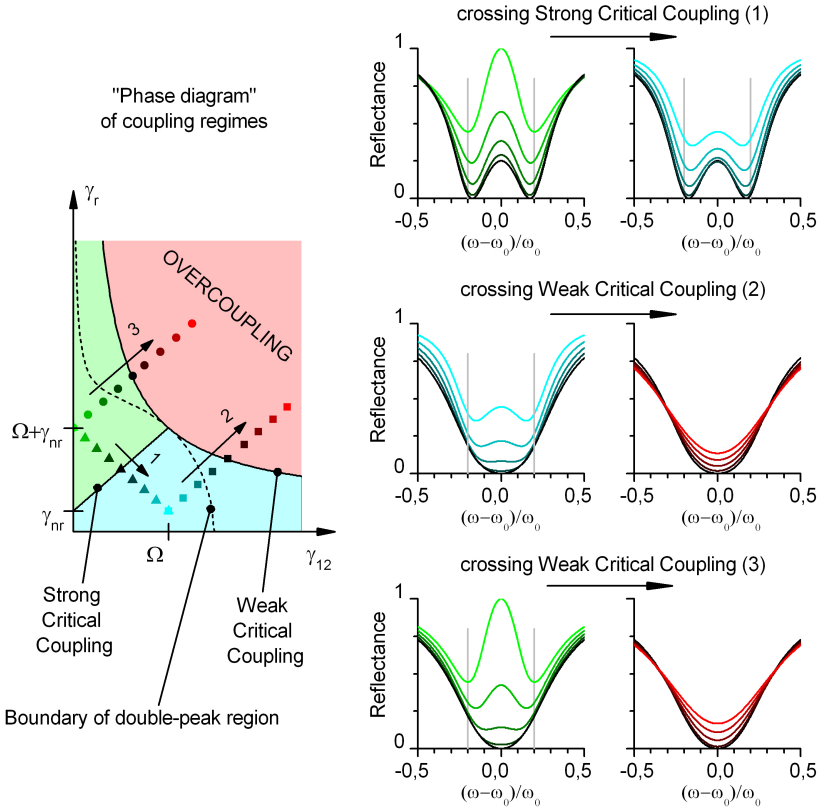


Figure 2.3: "Phase diagram" for the coupling regimes when the matter resonator exchanges energy with the cavity ($\Omega \neq 0$). Numerical values employed are $\gamma_{nr} = 0.05\,\omega_0$, $\Omega = 0.2\,\omega_0$.

of the presence of polariton states. On the other hand, a scarce polariton absorption implies potential difficulties in pumping polariton states, hence limiting the efficiency of certain scattering experiments [De Liberato09c, De Liberato13].

## 2.2 Formalism for the two-port system

In the following we will generalize the discussion to the case where a second scattering channel has to be considered. Having again in mind practical implementations, this framework includes photonic crystal

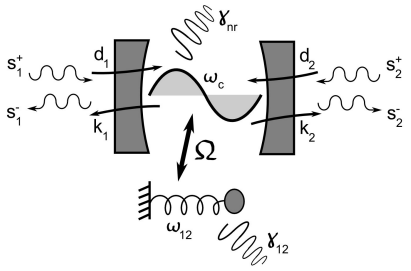


Figure 2.4: Scheme of the two-port photonic cavity. It is coupled to the scattering channels via the coupling constants $d_{1,2}$ and $\kappa_{1,2}$, eventually connected to the radiative decay rate $\gamma_r$ (see text).

membranes like those we are going to analyse in the next Chapter (see, e.g., Fig. 3.10). By referring again to [Fan03], and to Fig. 2.4, the two scattering channels are labeled by indices $1, 2$ and the equations 2.1 are rewritten as follows:

$$\begin{aligned} \frac{db}{dt} &= (i\omega_{12} - \gamma_{12})b + i\Omega a \\ \frac{da}{dt} &= (i\omega_c - \gamma_c)a + i\Omega b + (\langle\kappa|^*)|s^+\rangle \\ |s^-\rangle &= C|s^+\rangle + a|d\rangle \end{aligned} \tag{2.18}$$

where $|s^\pm\rangle = (s_1^\pm, s_2^\pm)^T$ are column vectors describing ingoing and outgoing scattering amplitudes. Also the coupling constants have to be arranged in vectors, $|d\rangle$ and $|\kappa\rangle$. In this notation, the transformation $|v\rangle \rightarrow \langle v|$ means transposition *and* complex conjugation, while $|d\rangle \rightarrow |d\rangle^*$ means only complex conjugation. $C$ stands for a scattering matrix which describes the background, non-resonant process that would take place if there were no coupling with the resonances: hence, it must be unitary (enforcing energy conservation) and symmetric (enforcing reciprocity[7]). Additional constraints stem from the require-

[7]Reciprocity is a quite general concept, sometimes referred to with the sentence "if source and detector are exchanged, nothing changes". Although not very clear in the underlying hypotheses, this sentence is substantially true, and in our system it means that the transmission amplitude between ports 1 and 2 is the same, both in phase and in amplitude, as the transmission amplitude between ports 2 and 1. Electromagnetic reciprocity in this sense is a consequence of Lorentz reciprocity theorem (a corollary of Maxwell equations) plus the hypothesis of dealing with linear response ($\varepsilon$ and $\mu$ independent of frequency) and "material reciprocity" ($\varepsilon$ and $\mu$ being symmetric tensors). A non-reciprocal device must contain either a non-linear or a magneto-optical material [Hoop60, Jalas13].

ment of instantaneous energy conservation of the global process, that is, fulfilment of Eq. 2.2. This is guaranteed by the conditions

$$\begin{aligned} |\kappa\rangle &= |d\rangle \\ \langle d|d\rangle &= 2\gamma_r \\ C|d\rangle^* &= -|d\rangle. \end{aligned} \tag{2.19}$$

As for the one-port case, the total cavity damping rate $\gamma_c$ is written as the sum of a radiative and a non-resonant contribution $\gamma_r + \gamma_{nr}$, where only the first is involved in the normalization of the radiative coupling constants $|d\rangle$.

By searching for the steady-state solution of Eq. 2.18, one gets that the outgoing amplitudes are linearly dependent from the ingoing amplitudes by means of a frequency-dependent scattering matrix: $|s_0^-\rangle = S(\omega)|s_0^+\rangle$, where

$$S(\omega) = C - \frac{i(\omega - \omega_{12}) + \gamma_{12}}{(\omega - \omega_+)(\omega - \omega_-)} |d\rangle \left(\langle d|^*\right). \tag{2.20}$$

As for the one-port theory, the polariton poles $\omega_\pm$ already given in Eq. 2.6 again appear. But here the theory is more complex (and rich), as the direct and resonant processes are described by matrices rather than by scalars (cfr. Eq. 2.4). Implementing the constraints introduced above, those matrices can be written in terms of a minimal set of parameters which evidence the key "ingredients" of the theory[8]:

$$C = e^{i\phi} \begin{pmatrix} re^{i\psi} & it \\ it & re^{-i\psi} \end{pmatrix}$$

$$|d\rangle \left(\langle d|^*\right) = -e^{i\phi}\gamma_r \begin{pmatrix} d_{11} & d_{12} \\ d_{12} & d_{22} \end{pmatrix}$$

$$\begin{aligned} d_{11} &= \left(r + x \pm it\sqrt{1-x^2}\right) e^{i\psi} \\ d_{22} &= \left(r - x \pm it\sqrt{1-x^2}\right) e^{-i\psi} \\ d_{12} &= \pm r\sqrt{1-x^2} + it \end{aligned} \tag{2.21}$$

The non-resonant process is basically described by the constant reflectance and transmittance $r$ and $t$, subject to the constraint $r^2 + t^2 = 1$

[8]The following expressions are the most general ones that fulfil the constraints given in Eq. 2.19, and generalize both [Fan03] and [Auffèves-Garnier07].

and $0 < r, t < 1$; $\phi$ and $\psi$ are a global and a relative phase. The resonant process inherits most of its properties from the non-resonant one, with the addition of a further degree of freedom $x \in [-1, 1]$ which describes the asymmetry occurring in the emission of radiation from the resonant mode: $x = (|d_1|^2 - |d_2|^2)/(|d_1|^2 + |d_2|^2)$. If the physical system under analysis possesses a spatial symmetry that exchanges the scattering channels 1 and 2, one must have $x = 0$ and $\psi = 0$ or $\pi$. Furthermore, the arbitrary sign which appears in (2.21) can be chosen at will, and it is connected to the symmetry of the resonant mode. As a limiting case, note that the positions $r = 1$ and $x = \pm 1$ imply that the two-port system factorizes into two one-port systems, with either port 1 or 2 in interaction with the resonance (see Eq. 2.5 for comparison).

As a final remark, we notice that the S-matrix determinant coincides – apart for a phase factor – with the reflection amplitude calculated for the 1-port system (Eq. 2.5):

$$\det S(\omega) = e^{2i\phi} \frac{(\omega - \bar{\omega}_+)(\omega - \bar{\omega}_-)}{(\omega - \omega_+)(\omega - \omega_-)} \tag{2.22}$$

with the same zeroes and poles reported in Eq. 2.6. Together with the fact that the determinant does not depend either on $r$ or on $x$, this is the key for extending the concepts of strong and weak critical coupling to the 2-port system (Sect. 2.2.2).

### 2.2.1 Lineshape inheritance

In passing from the one- to the general two-port theory, the additional parameters $r$ and $x$ have to be introduced[9]. It is known that $r$ governs the bare resonator lineshape [Fan03]: indeed, by setting $\Omega = 0$ and sweeping $r$ from 0 to 1 one finds that the reflectance spectrum sweeps from a Lorentzian to a reversed Lorentzian, passing through asymmetric Fano-like lineshapes. This is true when the system is symmetric ($x = 0$); the less common situation of an asymmetric system leads to warped lineshapes with smaller contrasts. The contrast is also reduced by the presence of a damping $\gamma_{nr}$, while the radiative damping $\gamma_r$ only determines the linewidth. It can be shown that when $\gamma_{nr} = 0$ and $x = 0$ the reflectance lineshapes are fully contrasted; given the absence of losses other than the radiative ones, unity contrast is also observed in transmittance.

[9] Remember that $t$ is univocally determined by $r$, and that $\psi$ cannot be read out from an experiment where only intensities are measured.

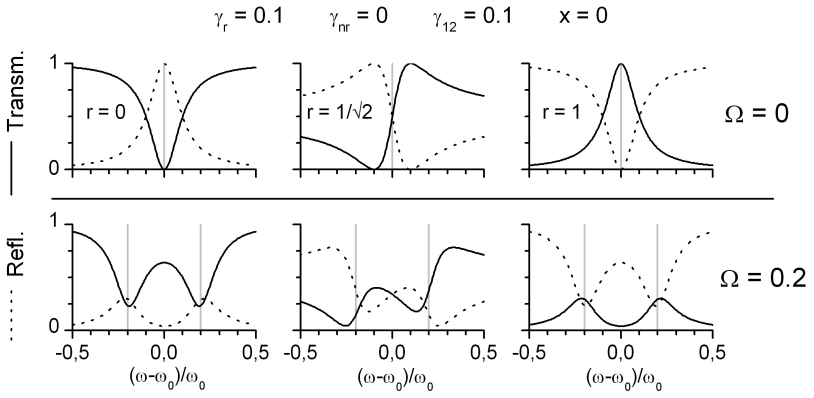


Figure 2.5: Lineshapes of the uncoupled photonic resonator (upper panels) and corresponding lineshapes when the light-matter coupling is turned on (lower panels). The parameter $r$ governs the resonator lineshape, which is inherited by the polariton lineshapes.

In Figure 2.5, upper panels, we report a set of sample curves which show the phenomenology detailed above. Here, the upper sign in Eqs. 2.21 is employed; the other choice would have exchanged $(\omega - \omega_0) \rightarrow (\omega_0 - \omega)$ hence reversing the $r = 1/\sqrt{2}$ spectrum. The onset of a light-matter coupling (lower panels) induces a splitting of the single photonic spectral feature in two polaritonic spectral features, whose lineshape is inherited from the first. Here, damping rate matching $\gamma_r = \gamma_{12}$ is assumed; this is the condition that maximizes the contrast. If one looks only at the transmittance[10], a counterintuitive behaviour is found when $r = 1$: despite the presence of absorption in the matter channel, two transmission *peaks* are observed. We will show later that this apparent non-sense is solved since the absorption lineshape, i.e. the real "probe" of the system's eigenmodes, does not depend on the specific value of $r$. The key is that the features in transmittance are compensated by those in reflectance, since the peak contrast and splitting are different. In particular, when $r = 0$ the contrast is larger in transmittance rather than in reflectance, and vice-versa occurs for $r = 1$: as a consequence, it turns out that a cavity with $r \simeq 0$ is better probed in transmittance, while a reflectance experiment is more suited when $r \simeq 1$.

[10]Transmittance is preferred to reflectance when performing angle-resolved experiments since the setup is less demanding.

Most of the above reported phenomenology has been observed in different experiments performed on intersubband polaritonic samples. The measured traces, pertaining to different photonic crystal geometries, are in good agreement with the theoretical traces, as it will be shown in different points of the next Chapter.

### 2.2.2 Polariton coherent perfect absorption (CPA)

As anticipated above, the interest is now drawn by absorption spectra, which, being directly connected to the cavity and matter field intensities $|a|^2$ and $|b|^2$, can be considered as a direct probe of the system eigenmodes[11]. Since we are dealing with a two-port system, both ordinary and joint absorbance will be considered. Ordinary absorbance is a well-known quantity, and is connected to transmittance and reflectance with the usual formula $A_{1,2} = 1 - R_{1,2} - T$, where $R_1 = |S_{11}|^2$, $R_2 = |S_{22}|^2$ are the reflectances and $T = |S_{12}|^2 = |S_{21}|^2$ is the transmittance[12]. Joint absorbance is a quantity that started drawing attention since the introduction of the *coherent perfect absorption* (CPA) concept [Chong10]. In a CPA experiment, when a two-port absorbing system whose scattering matrix has zero determinant is excited from both ports with proper input amplitudes, all the energy incident on the system is absorbed by the system itself. The key condition is that

$$\det S = 0$$

i.e. the scattering matrix determinant has to vanish.

It is anyway interesting to study the response of a general absorbing two-port linear system when the input channels are simultaneously excited by generic coherent inputs. If the arbitrary input vector $|s_0^+\rangle = (s_{0,1}^+, s_{0,2}^+)$ is considered, a certain amount of the input energy is absorbed by the system: from this, the *joint absorbance* is defined as $A_{\text{joint}} = 1 - \langle s_0^-|s_0^-\rangle / \langle s_0^+|s_0^+\rangle$. The joint absorbance depends on the dephasing between input beams $\Delta\phi = \arg(s_{0,2}^+/s_{0,1}^+)$, and passes from a minimum to a maximum hence showing *interferometric control of absorption* [Wan11]. Here we report the explicit expressions for ordinary

[11] In principle, as already discussed in Sect. 2.1.1, the system eigenfrequencies describing the free decay of the coupled resonators are given by the poles $\omega_\pm$. However, when looking at the system evolution upon external drive, a significant measure of the system's response is the resonant field enhancement, which can be accessed from the exterior through the absorbance, directly connected to the local field variables $a$ and $b$ via the formula $A \propto \gamma_{nr}|a|^2 + \gamma_{12}|b|^2$ (see Eq. 2.2).

[12] Transmittances from ports 1 and 2 are equal owing to reciprocity (see Footnote 7).

and joint absorbance derived from the $S$-matrix of the two-port coupled mode theory (Eq. 2.20):

$$A_{1,2}(\omega) = \frac{A_{1\text{port}}(\omega)}{2}(1 \pm rx) \tag{2.23}$$

$$A_{\text{joint; min,max}}(\omega) = \frac{A_{1\text{port}}(\omega)}{2}\left(1 + rx\xi \pm \sqrt{(1-r^2x^2)(1-\xi^2)}\right). \tag{2.24}$$

The key quantity is the absorption spectrum $A_{1\text{port}}$ of the one-port system, whose explicit expression is given in Eq. 2.7. Notice that this spectrum does not depend on the lineshape-governing parameter $r$. The dependence from $r$ and $x$ is limited to a multiplying factor, both when considering ordinary and joint absorbance. In the latter the new variable $\xi$ appear: this is introduced in the general CPA theory (Appendix A) for a quantification of the unbalance between the input beams, and is defined as $\xi = (|s^+_{0,1}|^2 - |s^+_{0,2}|^2)/(|s^+_{0,1}|^2 + |s^+_{0,2}|^2)$. Notice that the ordinary absorbances are recovered from the joint absorbance by setting $\xi = \pm 1$: actually, these choices correspond to single-beam excitation from either port 1 or 2.

Let us first consider a symmetric system ($x = 0$) upon symmetric excitation ($\xi = 0$). The above expressions now read

$$\begin{array}{rcl} \text{symmetric system} & & A_1(\omega) = A_2(\omega) = A_{1\text{port}}(\omega)/2 \\ & \rightarrow & A_{\text{joint; min}}(\omega) = 0 \\ \text{symmetric excitation} & & A_{\text{joint; max}}(\omega) = A_{1\text{port}}(\omega) \end{array} \tag{2.25}$$

Since $0 \leq A_{1\text{port}}(\omega) \leq 1$, the ordinary absorption cannot exceed the value[13] of $1/2$. Indeed, this limiting value is reached only for a frequency $\omega$ such that $A_{1\text{port}}(\omega) = 1$, i.e. when the strong or weak critical coupling conditions (Eqs. 2.16 or 2.17) are fulfilled. Critical coupling also implies that the joint absorbance sweeps from 0 to 1, that is, upon a sweep of the input beam dephasing $\Delta\phi$ both coherent perfect absorption and coherent perfect transparency (CPT) are observed. Notice that here CPT is *always* attained, independently of the values of the parameters ($\Omega$ and $\gamma$'s), while CPA occurs only when the damping rate matching is fulfilled, and only for the frequencies that set to 1 the one-port absorption. Recalling Eq. 2.7, the condition of unity one-port absorption coincides with the condition of zero one-port reflectance, i.e. a zero

[13] Absorption smaller than $1/2$ is a limitation specfic to a resonator having a single mode which can be driven from the exterior, as detailed in [Chutinan08, Peretti12].

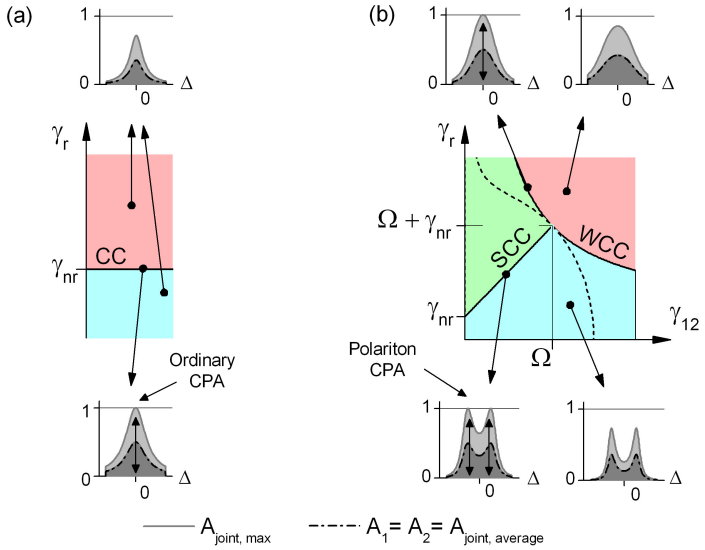


Figure 2.6: Absorbance of the two-port system at different points of the phase diagram. At the conditions for which the single-port system exhibited zero reflectance (*critical coupling*), the two-port system exhibits coherent perfect absorption (see also Figs. 2.2 and 2.3). Panel (a) describes the uncoupled case ($\Omega = 0$), while in panel (b) the coupled case ($\Omega \neq 0$) is analyzed. A symmetric system ($x = 0$) is considered, and the joint absorbance is calculated for equal-amplitude excitation ($\xi = 0$).

of the one-port reflection amplitude (Eq. 2.5). This is consistent with the CPA condition $\det S = 0$, since the analytical expression of the determinant (Eq. 2.22) coincides with the one-port reflection amplitude (Eq. 2.5), apart from an irrelevant phase factor. This phenomenology is summarized in Fig. 2.6: the phase diagrams are the same as in Figs. 2.2 and 2.3, while the insets report the ordinary and joint absorbances corresponding to different parameter choices. In substance, CPA is the exact counterpart of the critical coupling occurring in the one-port system.

This is true when the comparison is made both with the ordinary critical coupling (Sect. 2.1.2) and with the strong critical coupling (Sect. 2.1.3). In the first case, schematized in Fig. 2.6 (a), the optical resonator is decoupled from the matter oscillator ($\Omega = 0$) but exhibits intrinsic non-resonant losses ($\gamma_{nr} \neq 0$). When the critical coupling condition ($\gamma_r = \gamma_{nr}$) is fulfilled, the joint absorbance – which in this case

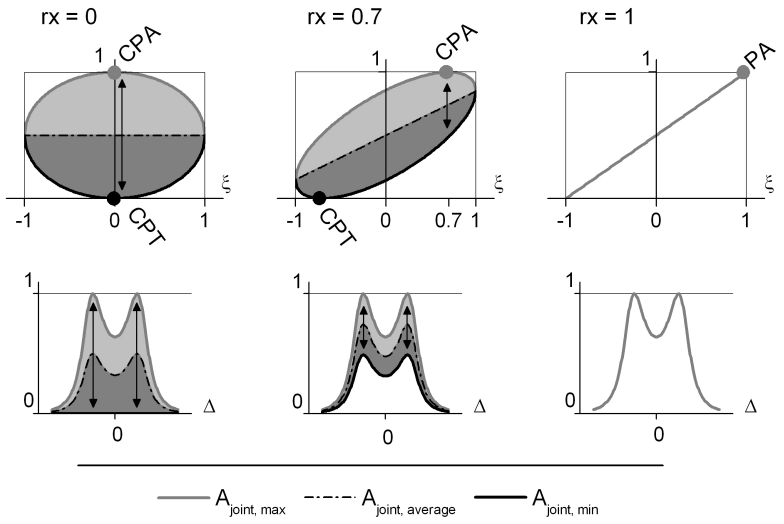


Figure 2.7: Coherent perfect absorption and coherent perfect transparency (CPA and CPT) for a two-port system at strong critical coupling, with the transition from a symmetric one ($x = 0$) to a fully asymmetric one ($rx = 1$, coincident with the one-port system). When the excitation asymmetry $\xi$ is swept (upper panels, see text for the definition of $\xi$), CPA and/or CPT conditions are found, as reported in the joint absorption spectra (lower panels). Notice that CPA and CPT occur simultaneously only for the symmetric system (left panels), while in the one-port system (right panels) the joint absorption modulation depth is lost and the perfect absorption (PA) is attained for a fully asymmetric excitation ($\xi = 1$), hence losing the *coherent* character.

has always a Lorentzian lineshape – can be modulated from zero to one, hence showing CPA and CPT at the resonance frequency. This corresponds to the first experimental evidence of CPA in a Fabry-Pérot slab resonator [Wan11].

In the case of non-zero cavity-matter coupling ($\Omega \neq 0$), reported in Fig. 2.6 (b), observation of *polaritonic CPA* is possible. Indeed, when the *strong critical coupling* condition (Eq. 2.16) is fulfilled, the joint absorbance shows a double-peaked spectrum, and at the resonance frequencies it can be modulated from zero to one.

The parallelism between *critical coupling* in the one-port system and CPA in the two-port system is not a fortuity, since there is a continuous transition between the one- and two-port situations. As already

hinted, the choice of parameters $r = 1$ and $x = 1$ ($x = -1$) make the two-port theory exactly equal to the one-port theory, in the sense that only port 1 (port 2) is coupled with the photonic resonance and in turn with the matter oscillator. This is confirmed by looking at Eq. 2.23, which essentially tells that the energy is absorbed only when the "correct" port is excited. Meanwhile, a look at Eq. 2.24 reveals that when $rx = \pm 1$ the square root term is canceled out, implying that the joint absorbance modulation is lost; in other words, the "uncoupled" port does not play any role in exciting the resonance.

In the intermediate situations the physics is slightly more complicate, and a summary is given in Fig. 2.7. The upper panels report the factor $f_\pm(rx, \xi) = 1 + rx\xi \pm \sqrt{(1 - r^2x^2)(1 - \xi^2)}$ appearing in Eq. 2.24, for three significant values of $rx$. If $rx = 0$ one falls back in the symmetric case discussed above: at $\xi = 0$ one has $f_- = 0$ (that is CPT) and $f_+ = 1$ (that is CPA *if* $\det S = 0$). A sweep of $\xi$ towards $\pm 1$ induces a reduction of the absorbance modulation amplitude, and eventually the min/max joint absorbance reaches the ordinary absorbance. If $0 < rx < 1$, the ellipse described by $f_\pm$ is tilted, and the CPA/CPT points no more occur at the same $\xi$ value. This means that – although CPT can be always observed, and CPA can be attained when $\det S = 0$ – the maximum absorbance modulation amplitude does not occur simultaneously with CPT and CPA. In substance, the asymmetry limits the absorption modulation capability. This is further understood by looking at the right panel, where the ellipse degenerates in a line for the fully asymmetric system, i.e. the one-port system. The modulation depth is completely lost, CPT does not have sense any more and CPA loses its *coherent* nature becoming *perfect absorption*, i.e. the zero reflectance of the one-port system.

A final remark on the phases is due, which also clarifies the role of the $\pm$ sign in Eq. 2.21. Until now, we talked about minimum and maximum joint absorbance without giving details on which is the corresponding input beam dephasing $\Delta\phi = \arg(s^+_{0,2}/s^+_{0,1})$. It can be shown that, for a symmetric cavity ($x = 0$), when the $+$ sign is chosen in Eq. 2.21, maximum joint absorbance is observed for $\Delta\phi = 0$ and minimum joint absorbance when $\Delta\phi = \pi$; the reverse occurs when the other sign is chosen. In substance, that sign – which appeared from the general abstract solution of equation 2.19 – is connected with the even/odd character of the resonant modes.

## 2.3 Conclusions

In conclusion, we developed a coupled-mode theory (CMT) which describes in a semiclassical way a photonic resonator coupled to a matter oscillator, the former being coupled to two scattering channels which provide an access for driving the system's resonances. After the observation that the weak and strong coupling regimes of the light-matter interaction are correctly described, we focused our attention on the ability of the system to absorb the incoming energy. It turned out that the system can behave as a perfect absorber when certain matching relations on the damping rates are satisfied. These conditions generalize the known *critical coupling* condition to a strongly-coupled system, inducing the definition of *strong critical coupling*.

A feature of the theory is the possibility to describe a general, asymmetric two-port cavity, which in a limiting case degenerates in a one-port cavity. The perfect absorption implied by the critical coupling is read in different ways according to the symmetry degree of the cavity: while a critically coupled one-port cavity exhibits the usual zero reflectance (and hence unit absorbance), in the symmetric two-port cavity the critical coupling implies perfect absorption only upon coherent excitation from both ports, i.e. *coherent perfect absorption* (CPA). Meanwhile, by controlling the phase of the input ports, the absorption can be switched from 0 to 1, hence also realizing the *coherent perfect transparency* (CPT) and full *interferometric control of absorption*.

All of this may happen in a *polaritonic* fashion, provided that the light-matter coupling strength is sufficiently large. We will show in the next Chapter that most of the phenomenology observed in linear experiments on photonic-crystal based intersubband polariton samples can be interpreted within the current CMT framework, both when the resonator is empty (no light-matter coupling), when the resonator has non-resonant losses (weak coupling), and when the resonator is strongly coupled with a matter oscillator (an intersubband transition). In particular, we observed strong critical coupling in a two-port sample, i.e. polariton CPA. This is an important result in that it unifies different concepts (strong coupling, critical coupling, and CPA), and since perfect energy feeding into polariton states is relevant for a class of experiments where optical excitation of polariton states is a basic step for the observation of other phenomena, like stimulated scattering between polariton states [De Liberato09c] or terahertz lasing based on polariton-polariton transitions [De Liberato13].

# Chapter 3

# Linear spectroscopy of intersubband polaritons in photonic crystal resonators

The aim of this Chapter is to report on the design of intersubband polariton photonic crystal slab (PhCS) devices, and to analyze the results of their characterization performed by means of optical measurements in the linear response regime. We started being interested in photonic crystal slab resonators for having access at the resonance from the surface of the device rather than from the facet of a prism-based sample, in order to have a simpler geometry when performing ultrafast pump-and-probe experiments (see Section 4.2). It turned out then that the general framework of photonic crystal-based cavities entails a set of features which are valuable also in view of other physical processes involving intersubband polaritons. For instance, having a polaritonic dispersion which goes to a finite energy value at the center of the Brillouin zone removes a difference between the existent intersubband polariton systems and the exciton-polariton ones, where the *bottlenecking* due to the peculiar shape of the lower polariton branch enhances the emission of light from the polariton states [Tassone97].

In our opinion, however, the most important result is the development of tuning tools for the radiative decay rate of the photonic resonance, and the observation of perfect polaritonic absorption when cavity and transition decay rates are matched (Sect. 3.1.5). In parallel to the need of damping rate *matching*, which follows from the cou-

pled mode theory exposed in Chapter 2, in Chapter 4 it will turn out that damping rate *mismatch* plays a role too: actually, it triggers certain nonlinear responses that may be employed for saturable filters featuring a sharp response and even bistability. Hence, the ability to *increase* or *decrease* the radiative decay rate of a given photonic structure is an invaluable tool, and in Sects. 3.1.2 and 3.3.1 we are going to detail two mechanisms that lead to such control. In Sect. 3.1.2, the underlying idea is that of a defect-mode resonance, implemented in the suspended-membrane photonic crystal framework which is the global topic of Sect. 3.1. In Sect. 3.3.1, the idea is that a controlled etching of the photonic crystal semiconductor layer leads to a larger radiative decay rate of the resonance. This last approach works well on the double-metal photonic crystal framework, which is the global topic of Sect. 3.3, and which – as opposed to the suspended-membrane approach – can be scaled to the terahertz (THz) photon energy range.

The development of both suspended membrane PhCS (Sect. 3.1) and double-metal PhCS (Sect. 3.3) cronologically followed that of PhCS lying on a dielectric substrate, about which we report in Sect. 3.2. While the former have clear advantages – like sharp spectral features, high mode confinement, and possibility of direct optical access from both sides (suspended membrane), or THz operation and ultra-high mode confinement (double-metal) – the latter are easily fabricated and their design directly follows from the perturbation theory applied to the homogeneous metal-dielectric slab waveguide. However, the interpretation of the spectral features emerging from this sample design entailed the puzzling phenomenon of *lineshape inheritance*, which was not fully understood until the development of the coupled mode theory (Chapter 2). This theory hence turned out to induce a significant, unifying vision of the polariton physics in photonic cavities, and all the results given in this Chapter have been interpreted by means of that.

Exception made for the double-metal devices described in Sect. 3.3, which have been realized and measured in Paris[1], and for the epitaxial growth of all the other heterostructures, performed in Trieste[2], all the other design, fabrication, characterization, and result interpretation steps have been performed by the author at the NEST laboratory

[1]The epitaxial growth has been performed by I. Sagnes and G. Beaudoin at the Laboratoire de Photonique et Nanostructures, Marcoussis; the further processing steps and the measurements have been performed in collaboration with J.-M. Manceau and R. Colombelli at the Institute d'Electronique Fondamentale, Orsay.

[2]The heterostructures for suspended-membrane and on-substrate photonic crystals have been grown by G. Biasiol at the CNR-IOM, Basovizza.

in Pisa. Technical details about the fabrication technology are given in Appendix B.

## 3.1 Free-standing metal-dielectric photonic crystal slabs

Strictly speaking, a photonic crystal is an arrangement of light-scattering elements periodic along 1, 2 or 3 spatial dimensions, and traslationally invariant along the remaining ones [Joannopoulos95]. Being that concept omnipresent in photonic science, there is no need to spend much time about that here; just for introductory purposes, it suffices to say that their peculiar property is the presence of *photonic bands*, possibly dispersive, separated by *band gaps*. It is especially the presence of band gaps that deserves a special interest, since it leads to a light confinement mechanism intrinsically different from those of reflection by a metallic boundary or total internal reflection between dielectrics having different permeability.

A photonic crystal *slab* (PhCS) is rather a structure where there is one spatial dimension along which the light is confined by means of a waveguide mechanism (either dielectric or metallic), while periodicity is implemented only along one or two of the remaining dimensions. The photonic crystal slab concept draws the interest of both pure and applied scientists, since they maintain the main feature of photonic crystals – that is the *photonic gap*, hence allowing to design *waveguides* and *resonant cavities* based on that confinement mechanism – while their fabrication process involves only planar techniques. Indeed, on one side the efforts of a branch of telecommunication research are today devoted to implement on-chip PhCS components for fast information processing, and on the other side physicists are now able to integrate such wavelength-scale resonators with single quantum emitters hence paving the way for quantum optics experiments and computation protocols. Further interest in PhCS physics relies on the development of efficient sensing devices. Last, but not least, the weight scale of the membranes on which certain PhCS designs rely triggered interest towards the rapidly growing field of nano opto-mechanical systems, where new physics inherent to the quantum world is still emerging.

Among the electromagnetic resonances of photonic crystal slabs or related devices, there are two main classes that we are going to deal with. The first is observed in an ideally infinite PhCS, with a simple

unit cell: these are the *quasi-guided resonances* lying above the substrate and superstrate light cones [Lourtioz08]. These resonances can be excited by shining a light beam on the surface of the sample, and appear as sharp features in the transmittance or reflectance spectra [Fan03]. Their character is inherited both from the underlying mode structure of the photonic waveguide, and from the band structure of the corresponding ideal photonic crystal: this will be clarified in Sect. 3.1.2. The second class of resonances is observed in a PhCS where the periodicity is broken and a *defect* is introduced: these are *defect mode* PhCS resonances. Again, for our purposes we designed defect mode resonances that can be excited from the sample surface. The main mechanism lying below the desired quasi-normal-incidence operation is the *second order Bragg diffraction*, i.e. the photon incident on the sample surface couples to the slab waveguide mode via *one* Bragg vector of the reciprocal lattice. Again, also this concept will be clarified later, in Sect. 3.1.1.

As opposed to the majority of studies involving photonic crystal slabs, where the constituents are only dielectrics, we are going to deal with *metallo-dielectric* PhCS. The presence of metal stems from the fact that intersubband transitions couple only with light polarized along the epitaxial growth axis, and hence the metallic surface close to the quantum well region helps to accomplish that constraint. While periodically patterned metallic structures have been the topic of many works and intense discussions, especially in connection to the *extraordinary transmission* phenomenon and the connected role of *surface plasmon polaritons*[3], proper *metallo-dielectric* PhCS have been the topic of a limited set of papers, mostly authored by the group of H. Giessen. In these works, the main topic was the development of a photonic band gap [Christ03, Christ04], the study of "defects" [Zentgraf06], or the influence of disorder [Nau07]. The employed material platform was a dielectric oxide grown on glass, working at visible wavelengths.

Although we started from these concepts, in the present work we achieved two significant advances. First, from the purely photonic point of view, the band structures of our samples show larger band

[3]In 1998 it has been discovered that an array of holes drilled in an optically thick metallic membrane shows a transmittance much larger than that expected by a naif calculation based on the ratio between the hole area and the total membrane area [Ebbesen98]. This phenomenon is somehow the tip of the iceberg, since a connection exists with the surface plasmon electromagnetic mode supported by a metal-dielectric interface, with Wood anomalies, and with resonant modes in the metallic holes [Martín-Moreno01, Cao02, Marquier05, Sarrazin03].

gaps (Sect. 3.1.1) and true defect modes, i.e. resonances where the field is spatially confined and enhanced (Sect. 3.1.2). Second, our structures embed quantum wells, here for the passive observation of intersubband polaritons, but with the possibility of developing active devices like infrared detectors or emitters – perhaps based on the polariton physics.

### 3.1.1 Quasi-guided photonic crystal modes

The first photonic crystal slab geometry we are going to explore is schematized in Fig. 3.1. It consists of a semiconductor layer patterned with an array of equispaced gold stripes. The semiconductor layer is a multi-quantum well (MQW) based on the $GaAs/Al_{0.33}Ga_{0.67}As$ material system: if there is no doping, it acts as an ordinary lossless dielectric[4], while a certain amount of $n$-type dopants populates the first conduction subband in the quantum wells, hence activating the intersubband transition and eventually leading to intersubband polaritons. Being the aim of this Section to analyze the bare PhCS resonances, we will only make reference to the undoped samples.

While the details of the fabrication process are reported in Appendix B, here we just recall the typical values of the geometrical parameters employed for the samples analyzed in the present and the following Sections. The membrane thickness is in the range $t = 1.5 \div 2$ μm, the photonic period $a = 3 \div 4$ μm, and the metal fill factor is always $f = 0.8$.

In the photonic crystal slab philosophy, the working principle of the device can be interpreted by first considering the confinement along the $z$ direction [Gerace04]. In this sense, the membrane is an alternance of (air)/metal/dielectric/air (MD)[5] and air/dielectric/air (AD) slab waveguides, each of them characterized by a set of guided modes with effective permittivity $\bar{\varepsilon}$ (Fig. 3.1, right panel); given the interest in coupling with the intersubband transition, the sole TM polariza-

[4] In principle the alternance well/barrier material induces an anisotropy in the dielectric constant. This can be quantified by means of Eq. 1.44, and it turns out that for the actual values the anisotropy is of the order of 1 %.

[5] The presence of air above the metal can be neglected since the penetration depth in the metal is smaller than its thickness (of the order of 50 nm, see Appendix B for fabrication details).

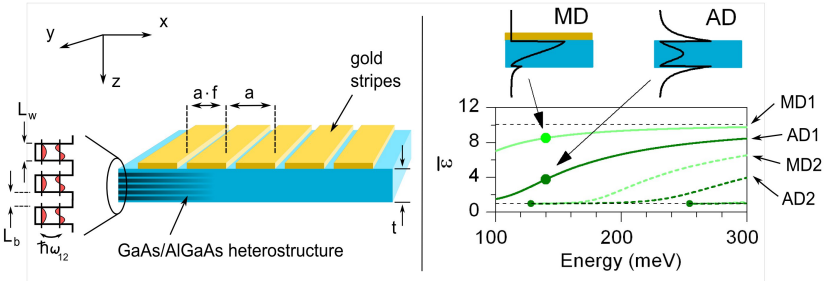


Figure 3.1: *Left panel:* Schematic of a metallo-dielectric photonic crystal slab free-standing membrane. The membrane consists of an alternance of few nanometer thick GaAs and $Al_{0.33}Ga_{0.67}As$ layers, hence implementing a multi-quantum well. *Right panel:* Guided modes of the planar slab waveguide obtained under the hypothesis that the photonic crystal is fully covered by metal ($f = 1 \rightarrow$ metal-dielectric mode, MD) or completely free from metal ($f = 0 \rightarrow$ air-dielectric mode, AD). The effective dielectric constants $\bar{\varepsilon}$ of the first few modes are reported.

tion is considered[6]. Here, the dispersion relations[7] $\bar{\varepsilon}(\omega)$ refer to the membrane obtained from the wafer HM 3311, which has a thickness $t \simeq 1.5$ μm and a bulk permittivity $\varepsilon = 10$, and whose target operation energy – given by the QW sublevel design – is 140 meV. At this photon energy, both MD and AD waveguides are substantially single-moded, and the contrast between their effective permittivities $\bar{\varepsilon}_{\mathrm{MD1}}$ and $\bar{\varepsilon}_{\mathrm{AD1}}$ is quite large. Hence, we expect that the patterned membrane will mimick a real 1-d photonic crystal, with photonic bands separated by a stop band in which a defect mode could be eventually promoted.

In order to observe the quasi-guided mode resonance of the photonic crystal slab, we performed spectrally- and angularly-resolved transmission measurements on a first sample, whose nominal lattice spacing is $a = 3.2$ μm (Fig. 3.2, left panel); the choice of this lattice spacing stems from requiring operation close to the second-order Bragg stop band. The spectra, measured with $p$-polarized light incident on the $xz$ plane[8] are arranged in a color-map plot by employing

[6]Notice that, for PhC slab modes propagating along the sole $x$ direction, the same TE/TM polarization factorization scheme of a slab waveguide applies. Here, a TM mode has non-zero field components $E_x$, $E_z$ and $H_y$.

[7]The dispersion relation has been calculated by searching for the zeroes of the transfer matrix, starting from the formalism given in [Born99].

[8]Since the incidence plane is $xz$, the PhC modes with $k_y = 0$ are probed, and it can be shown that upon $p$-polarization input only the TM modes are excited. In addition, the

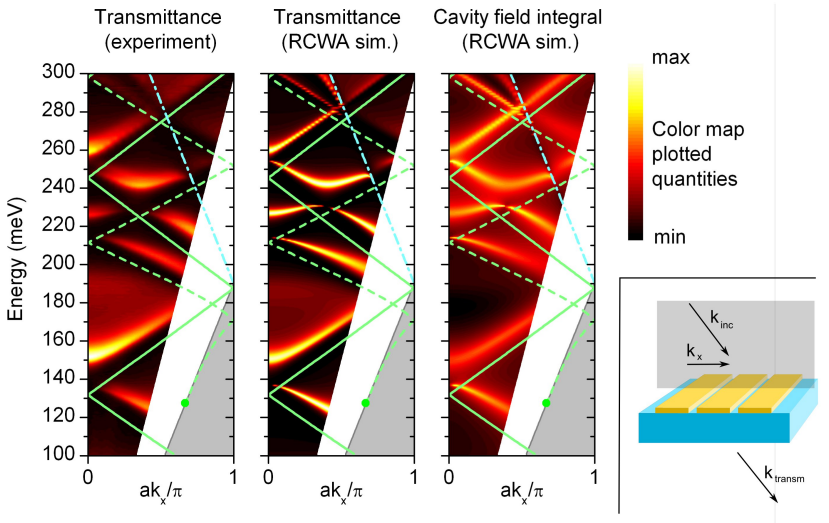


Figure 3.2: Photonic bands (i.e. *quasiguided modes*) of a metallodielectric photonic crystal membrane. The color maps report the result of an actual experiment (FTIR) and of numerical simulations (RCWA), while the superimposed lines have been obtained by means of a band folding scheme.

the relation $k_x = k_0 \sin(\theta)$, where $k_0$ is the light wavevector in vacuum and $\theta$ the incidence angle measured with respect to the normal to the sample surface. A set of high-transmittance bands can be noticed, and a gap feature separating two isolated bands clearly appears close to 140 meV.

Before introducing models which can describe the opening of a photonic gap, the photonic resonances will be interpreted within a simple mode folding scheme. Since we are working with large metal fill fraction $f$, the PhC slab can be regarded as a perturbation of the unpatterned MD slab waveguide, and the resonances are expected to appear when an incident photon couples with one of the MD guided modes. This process is allowed when the in-plane component of the wavevector $k_x$ matches the waveguide modal propagation constant $\beta = k_0\sqrt{\bar{\varepsilon}}$, thanks to the contribution of a reciprocal lattice wavevector:

$$|k_x + mg| = k_0\sqrt{\bar{\varepsilon}} \tag{3.1}$$

where $g = 2\pi/a$ and $m = 0, \pm 1, \pm 2 \ldots$ The second-order Bragg condition, $a/\lambda_0 = 1/\sqrt{\bar{\varepsilon}}$, follows from the above equation for $|m| = 1$ and

transmitted and reflected beams are still $p$-polarized and propagate along the $xz$ plane.

$k_x = 0$. The full solutions of the above equation, for different $m$'s and for $\bar{\varepsilon} = \bar{\varepsilon}_{\mathrm{MD1}}$, $\bar{\varepsilon}_{\mathrm{MD2}}$ are reported as green lines superimposed to the color plots in Fig. 3.2. The solid line corresponds to the mode MD1, while the dashed line corresponds to MD2. In essence, in correspondence to these points of the $k_x$-$E$ plane, an incident photon can enter the membrane, dwell for a certain time as a waveguide photon, and be re-radiated as a free photon towards the bottom semispace. This is a first interpretation of the transmittance features, both below and above 180 meV, i.e. where one or two MD modes are involved. It can also be noticed that additional features appear in correspondence to the cyan dash-dot line, which represents the folded air light cone, i.e. the first-order diffraction limit.

Being this model very simple – it is basically a zero-order perturbation theory – further features of the PhCS quasiguided modes like band gaps, radiative coupling efficiency, or spectral lineshapes, cannot be predicted. These limitations can be overcome by a much more accurate modeling tool: the rigorous coupled wave analysis (RCWA)[9]. This method takes as input the actual geometric parameters and dielectric properties of an arbitrary multilayer periodic structure and solves the Maxwell equations with incoming plane waves as boundary conditions. Although it gives no insight into the mechanisms at the origin of photonic resonances, it is a very useful tool to be used either before or after an actual experiment in order to refine the structure parameters around an initial guess, or to figure out whether a sample actually meets the fabrication parameters.

In the central panel of Fig. 3.2 we report the transmittance spectra calculated from RCWA for the sample parameters corresponding to experimental conditions[10]. The high-transmittance bands are cor-

[9] Since at the beginning of this thesis work we were not aware of the availability of free implementations of this method (see the Wikipedia page *Rigorous coupled wave analysis* for a set of links), we implemented the method first in Fortran and then in Matlab. Having thus direct access to the code structure, it was possible to deeply optimize it for the special case of one-dimensional structures working in TM polarization. The theory was taken from [Granet96, Whittaker99, Liscidini08].

[10] Actually, we performed two rounds of RCWA simulations. Before the sample fabrication we started by tuning the sample parameters $t$, $a$ and $f$ around initial guesses given by the band folding scheme in order to observe a clear resonance around 140 meV at normal incidence. After having measured the transmittance spectra, and observed that it did not perfectly match the design requirements, we performed a fit over the parameters $t$ and $a$. This is justified by the fact that $t$ is affected by uncertainties in the epitaxial growth and $a$ is affected by a slight uncalibration of the lithography system. The fill fraction $f$ has instead been accurately measured with scanning electron microscopy: being $f$ the ratio between lengths, it is unaffected by errors in the measure

rectly reproduced: in the RCWA certain features like band anticrossings are even more clear than in the experiment. For instance, look at the energy region between 120 and 170 meV, where the second-order Bragg resonance occurs. Remarkable matching between experiment and RCWA is attained on the upper transmittance band (extending from 150 to 170 meV), while the lower transmittance band is clearer in the RCWA than in the experiment. This can be ascribed to the non-planarity of the photonic crystal slab, which is of the order of 5° on the whole membrane[11]: being the involved features spectrally narrow and angularly dispersive, a smoothing in the experimental data occurs. The smoothing of narrow features can be also attributed to other sample inhomogeneity sources, like membrane thickness fluctuations or lithography inaccuracies[12]; finally, the finite aperture of the optics in the spectrometer contribute to the phenomenon[13]. Such smoothing also occurs at the higher-order band gaps, where the lower bands seem to disappear in the experimental spectra. Indeed, the lower band exists, but its linewidth approaches zero at the band gap due to symmetry reasons. This is clear at the second Bragg resonance, where the sole MD1 mode is involved: the higher-order terms in the perturbation theory induce a splitting of the two degenerate unperturbed folded modes into a doublet of modes, having opposite parity (in the sense of $x \to -x$ exchange) and hence one of them is inhibited from radiatively coupling with the far-field [Fan06].

In the above discussion the folded MD modes have been compared with the transmittance peaks, assuming that the latter are a direct fingerprint of the photonic crystal slab quasiguided modes. This picture can be justified by recalling the coupled-mode theory (CMT) for photonic resonances [Fan03], which predicts the transmittance lineshape given by Eq. 2.20 – a generalized Fano lineshape – when the light-matter coupling $\Omega$ is set to zero. When the background reflectance $r$ is set to 1 – a reasonable choice since the large-$f$ metallic layer acts as a mirror when the resonance condition (3.1) is far from being satisfied – the transmittance from CMT is a Lorentzian peak, very close to the

of absolute lengths.

[11] Membrane non-planarity is attributed to crystalline stress in the epitaxial layers, released when the substrate is removed.

[12] In principle, metal losses could be another source of spectral feature smoothing, but the comparison of RCWA performed with and without metal losses exclude this possibility. For this reason, all the RCWA calculations relative to mid-infrared samples are carried out neglecting the metal losses.

[13] An $f/30$ optical system was employed.

experimental observations.

In addition to transmittance calculations, RCWA also provides an additional tool for directly figuring out the presence of a PhCS quasi-guided mode. By including a small imaginary part (say 0.01) in the $z$-component of the dielectric tensor of the semiconductor membrane, the RCWA outputs an *absorbance* which is proportional to the $|E_z|^2$ field integral in the membrane[14]. This quantity is plotted in the right panel of Fig. 3.2, and it clearly appears that the transmittance peaks correspond to the excitation of PhC slab quasi-guided modes.

In conclusion, we realized a photonic crystal slab based on a metallo-dielectric guided mode. The main feature of 1-d photonic crystals have been observed, i.e. dispersive bands reaching a finite energy value at the $k = 0$ point (Brillouin zone center), and separated by an energy gap.

### 3.1.2 Defect modes in the second-order stop-band

Defect modes lying in the photonic gap of a photonic crystal or of a photonic crystal slab are well known and studied since many years [Joannopoulos95, Lourtioz08]. Among their most relevant applications in view of the light-matter coupling, one can cite the control of spontaneous emission of single quantum emitters [Noda07], and the observation of the strong coupling regime between a single emitter and the cavity [Yoshie04, Reithmaier04]. While the above cited applications rely on dielectric structures, in this Section the same concepts are exported to the metallo-dielectric photonic crystal slab geometry analyzed in the previous Section. By these means, we show that it is possible to independently tune both the radiative lifetime (and hence the transmission linewidth and field enhancement) and the angular acceptance (i.e. the extension of the bands in the Brillouin zone) of the PhC slab.

Devices relying on similar physical grounds are the photonic crystal quantum cascade lasers proposed in [Chassagneux10, Xu12], where a $\pi$-shift or an adiabatic modulation of the periodicity of a double-metal photonic crystal structure forces the light to be confined in a certain region of the photonic crystal; in parallel, the directional properties of the coupling with the far-field and the radiative Q-factors are

[14] This trick enables to avoid time-consuming field integrations, and relies on the easy access to the absorbance of the structure within the RCWA method [Zanotto10]. By employing the dipolar dissipation formula $w(\mathbf{r}) = \omega/4\varepsilon_0\ \mathrm{Im}[\varepsilon(\mathbf{r})]\ |\mathbf{E}(\mathbf{r})|^2$, one can get the field integral in absolute units.

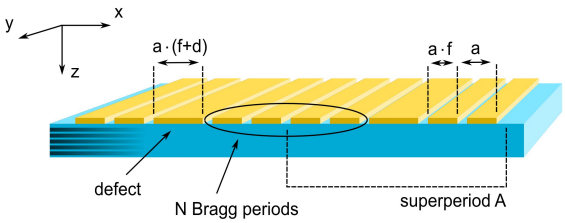


Figure 3.3: Supercell photonic crystal slab. The only difference with respect to the philosophy of Fig. 3.1 is the metal stripe arrangement.

tuned according to the needs. Here we analyze a prototypical passive device, with the main aim of studying how the defect resonances interact with the far field (in terms of Q-factors and angular acceptance), and how the local field is distributed inside the photonic crystal. These concepts can be applied to infrared devices like guided-mode resonance filters with tunable band-pass properties, giving more freedom to the system described in [Sakat11, Sakat12], or to photonic crystal quantum well infrared photodetectors (PhC-QWIPs) [Schartner08, Kalchmair11, Gansch11]. The simultaneous presence of metal (acting as a contact) and absence of etching (that introduces scattering centers and removes active region material) could lead to improved performance, following the guidelines sketched in [Rosenberg10]. The large intracavity field can also play a significant role in two-photon QWIPs, until now never realized in the photonic crystal configuration [Schneider08]. For our purpose, however, the main application of defect modes is the realization of intersubband polariton states which will be studied in detail in Sect. 3.1.4 (with the analysis of splitting and lineshape contrast) and in Sect. 4.1.4 (with the proposal of saturable filters featuring sharp transition efficiency, or bistable devices).

The scheme of the device is reported in Fig. 3.3. It derives from that of Fig. 3.1, by modifying a fraction $d$ of the width of one stripe each $N+1$. The remaining $N$ stripes act as a Bragg mirror for the photonic crystal quasiguided mode propagating in the membrane along the $x$ direction. In this way, a supercell arrangement is obtained: the system is still periodic, with period $A = (N+1+d) \cdot a$. Notice that the special case $d = 0$ corresponds to the PhCS without the defect.

Given the super-periodicity, the new system can still be studied with the RCWA method, provided that the new geometry is imple-

mented. However, the larger unit cell implies larger times needed for the calculation[15], and a simpler method would be preferred, at least for getting some insights into the possible existence of the defect mode. Being the mode folding scheme not capable of predicting the photonic band gap, the existence of defect modes cannot be inferred by Eq. 3.1. In essence, one needs to keep into account the presence of the photonic crystal regions below the air slits at a perturbation order higher than zero. This can be accomplished by considering a simple 1-d photonic crystal model, where the photonic crystal slab (translationally invariant along the sole $y$ direction) is replaced by a stack of effective dielectric layers translationally invariant along both $y$ and $z$. The scheme is reported in the top left of Fig. 3.4: a set of layers having the thicknesses and the effective permittivities of the corresponding metal/dielectric/air and air/dielectric/air regions of the real photonic crystal slab is the new, effective physical system under consideration. This system can be studied by means of the ordinary transfer matrix formalism, as reported, for instance, in [Yariv07].

Clearly, this is an approximation, perhaps quite rude under certain points of view. Firstly, in the 1-d photonic crystal model the waves propagating along the $x$ direction are plane waves, while in the real PhCS they are the MD and AD waveguide modes, which feature different field profiles. Secondly, here we consider the sole MD1 and AD1 modes, disregarding the upper modes – but this has less relevance when one restricts to the region below 170 meV, where the MD2 mode enters the first Brillouin zone above the air light cone. Finally, and perhaps most importantly, in the effective PhC model the radiative decay intrinsic in the photonic crystal slab physics is completely disregarded.

However, analyzing the results reveals the reliability of the approach. Let's compare panels (b) and (d) of Fig. 3.4: in the latter we simply replotted the transmittance bands of the photonic crystal slab without defect calculated by RCWA (cfr. Fig. 3.2, central panel) in the relevant energy range, while in the former the results of the 1-d

[15]In the RCWA method the convergence is guaranteed by employing a sufficiently large number of plane wave states over which the fields are expanded. Being $N_{\mathrm{PW}}$ this number for an ordinary photonic crystal with periodicity $a$, a supercell arrangement with superperiod $A$ will require $N'_{\mathrm{PW}} \simeq N_{\mathrm{PW}} \cdot A/a$ plane waves for convergence. Since matrix factorization and products are involved, the overall time goes as the third power of the number of plane waves, and the method can become unpractical. Important improvements are achieved by employing the correct *factorization rules* for products of discontinuous functions in the reciprocal space [Li96, Lalanne96].

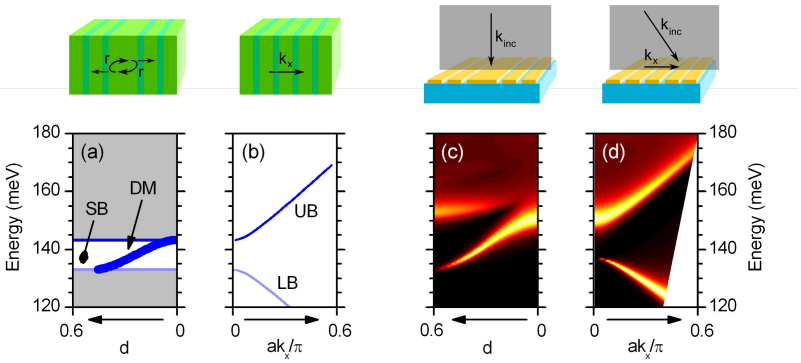


Figure 3.4: Photonic bands and promotion of a defect mode. *Panels* (a) *and* (b), eigenmodes calculated with a one-dimensional photonic crystal approach. *Panels* (c) *and* (d), transmittance of the corresponding real photonic crystal slab calculated by means of rigorous coupled wave analysis (RCWA). As the defect strip width $d$ is increased (see Fig. 3.3), a defect mode (DM) lying into the photonic stop band (SB) emerges from the bottom of the upper photonic branch (UB) and eventually collapses into the lower photonic branch (LB).

PhC model are proposed. Apart from a slight energy shift and a narrower gap, the 1-d model correctly predicts the presence of a gap and the band curvature. This motivated us to search for the defect modes in the 1-d approximation framework. The idea is that the light has to travel an integer number of round trips inside the cavity defined by the defect layer and the distributed Bragg mirrors (DBR): with reference to the upper left schematic in Fig. 3.4, we write

$$2\arg(r) + 2k_{\text{def}}L_{\text{def}} = 2m\pi \tag{3.2}$$

where $\arg(r)$ is the phase of the reflection amplitude of the (semi-infinite)[16] DBR; $k_{\text{def}} = k_0\sqrt{\varepsilon_{\text{MD1}}}$ is the wavevector in the defect effective medium, $L_{\text{def}} = a \cdot (f + d)$ is the defect thickness and $m$ is an integer[17]. The solution of this equation for $m = 1$ as a function of $d$ is reported in Fig. 3.4 (a): the defect mode is promoted from the $k_x = 0$ upper branch extremal point as $d$ increases, and eventually disappears at $d \simeq 0.5$ collapsing in the lower branch.

On these bases, we moved back to the RCWA to check whether the

[16] In the calculation $r$ has been obtained for a 20-layer stack DBR; this differs to a very small extent from the behaviour of an ideal semi-infinite DBR.

[17] Notice that our formula 3.2 corrects for a misprint in [Lourtioz08].

defect mode actually has a radiative coupling with the waves incident on the photonic crystal surface. For this purpose we calculated the transmittance spectrum of a defect-embedding PhC slab with variable $d$, under normal-incidence conditions. The ideal, isolated defect situation is mimicked by employing $N = 6$ Bragg periods, which required around one night of computing time on an ordinary office PC. Larger values of $N$ would have required impractical times when performing a refined $d$-sweep; however, further simulations performed on a selection of $d$ values showed that neither the defect mode frequency nor the linewidth significantly change when $N > 6$. These spectra are reported in Fig. 3.4 (c), showing that the defect mode promotion actually happens, and that its radiative coupling (linewidth) is continuously tuned from a maximum to zero without affecting the transmittance contrast. Again, the energy scales are slightly shifted, but the main physics is unaffected by the 1-d model approximations.

With these theoretical insights we fabricated a set of 3 samples, employing the heterostructure HM 3311 already used for the photonic crystal without defect, and using the the same $a = 3.2$ μm. The samples differ by the number of the Bragg mirror periods, which are 2, 4 and 6, while the defect stripe width parameter $d$ is always kept fixed at 0.4. The choice $d = 0.4$ is motivated by the interest in observing a sufficiently narrow transmission peak, without incurring in the strict fabrication requirements that would have been needed if we chose a value closer to the region $d \simeq 0.5$, where the transmission feature starts vanishing.

In Figure 3.5, right panel, the absolute transmittance spectra measured at normal incidence on the whole set of samples is reported, together with the RCWA spectra. For $N \neq 0$, the single spectral peak observed on the sample without defect (the upper photonic branch (UB) at Brillouin zone center) splits into two peaks, a narrow one at a lower energy and a broad one at a higher energy. The broad one gains contrast as $N$ is increased – and will eventually become the UB upon very large $N$. The narrow one, which is the defect mode (DM), gets narrower as $N$ is increased. Actually, this narrowing is clearer from the theory than from the experiment: this probably stems from the sample non-planarity which already led to the "washing out" of certain spectral features, as discussed in the previous Section. The localized nature of the defect mode is apparent from the field plots reported in Fig. 3.5: upon excitation with resonant light (photon energy at the peak of the transmission spectrum), the $z$-component of the electric field in-

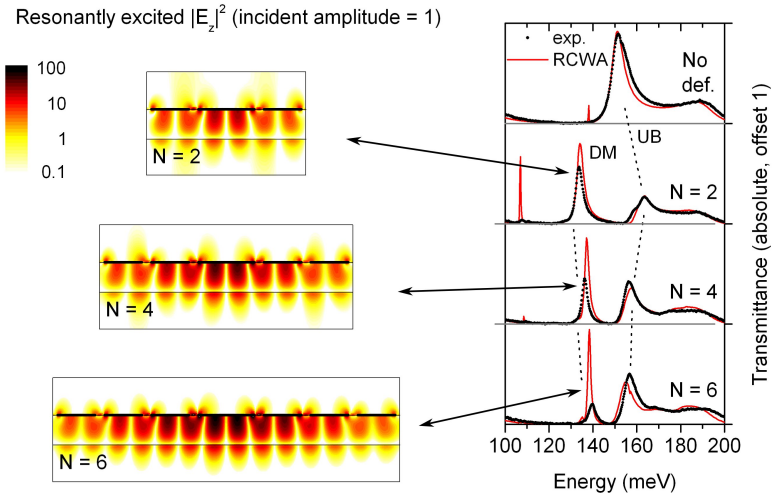


Figure 3.5: Effect of the number of Bragg periods $N$ (see Fig. 3.3). Starting from a sample without defect, the upper photonic branch resonance (UB) splits into two resonances, one of which is the defect mode (DM). This behaviour is confirmed by the resonant field distribution inside the membrane.

side the cavity is strongly enhanced, and is mostly concentrated below the defect stripe.

As already mentioned in the introdution of this Section, the defect mode photonic crystal slab can be employed as a guided-mode-resonance spectral band-pass filter. For this kind of application, control over lineshape and angular acceptance are crucial. This motivated us to analyze the angular response of our samples, with the by-product of further understanding the device physics within the 1-d photonic crystal model. In Fig. 3.6, upper panels, we report the measured transmittance spectra, as usual displayed in the $k_x$-$E$ plane, in the energy region of the second order photonic stop band. Correspondingly, in the lower panels we plotted the photonic bands calculated in the 1-d photonic crystal model, for the supercell with the proper number of Bragg periods $N$.

In the upper panels, the photonic band highlighted by an arrow is the evolution in the Brillouin zone of the normal-incidence defect mode (DM in Fig. 3.5). By comparing the observed spectral features and the calculated photonic bands it can be observed that the former

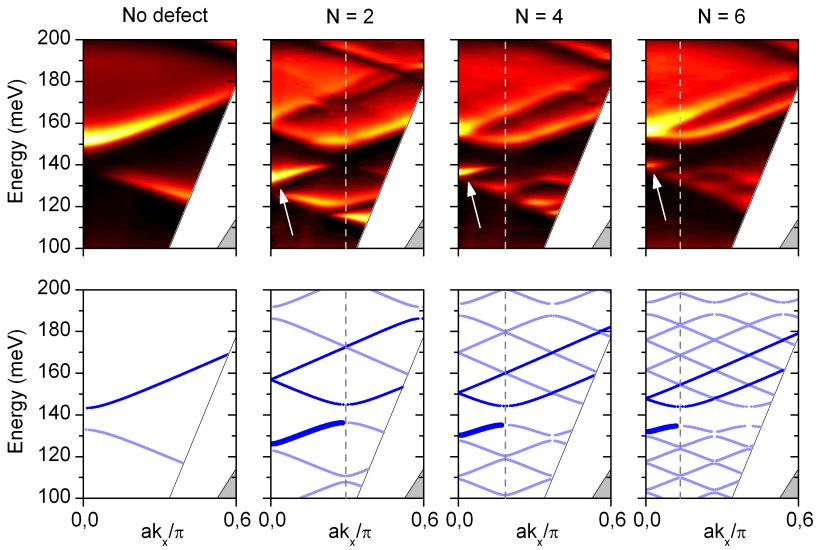


Figure 3.6: Photonic band structure observed by transmittance measurements on a set of fabricated membranes (*top panels*) and calculated by means of the one-dimensional photonic crystal approximation (*bottom panels*, see also Fig. 3.4). The white arrow highlights the defect mode, which corresponds to the band evidenced as a thick blue line in the bottom panels.

correspond to a subset of the latter. This means that not all the photonic bands obtained in the 1-d PhC model have a radiative coupling with the far-field. For instance, the defect mode corresponds to the band which is evidenced by a thick line, extending until the point $ak_x/\pi = a/A$. Instead, the upper branch of the photonic crystal slab without defect keeps extending across the whole Brillouin zone also when the defect is introduced. It actually consists of a doublet of bands, highlighted in dark blue in the lower panels, which tend to merge when $N$ is increased.

In conclusion, we designed, realized and characterized a set of photonic crystal samples where the periodicity is perturbed by the introduction of a defect, which leads to additional spectral features corresponding to resonant modes, whose field profile is spatially localized. The peculiarity of these modes is that both their radiative linewidth (i.e. the resonance Q-factor) and their angular acceptance can be tuned independently by means of fabrication parameters such as the defect stripe width and the number of Bragg periods. Among the possible ap-

plications for narrow band-pass mid-infrared spectral filters with tunable angular response, and for infrared radiation detectors, the large Q-factor (with comparison to that of typical intersubband transitions) will be the key for designing a sharp saturable filter, or a bistable device. Indeed, by turning on the intersubband transition of the QWs embedded in a defect-mode PhCS, defect-mode intersubband polaritons are observed (Sect. 3.1.4). Furthermore, in Sect. 4.1.4 it will also be shown that a saturation phenomenon occurs, on a very narrow range of values for the intensity incident on the device.

### 3.1.3 Intersubband polaritons with quasi-guided photonic modes

With the device geometry described in Sect. 3.1.1, we now demonstrate that intersubband polariton features clearly emerge when the quasi-guided photonic mode above the second-order stop-band (upper photonic branch in the notation of Fig. 3.4) is brought in resonance with the active intersubband transition of doped quantum wells embedded in the photonic crystal membrane.

Starting from two heterostructures which only differ by the presence of doping in the wells (HM 3227 and HM 3231), we fabricated two identical photonic crystal membrane samples having $a = 4.35$ μm, $f = 0.8$ and $t = 2$ μm. These choices allowed to implement an isolated photonic band extending around the energy $E \simeq 120$ meV. In this way, the photonic band is in resonance with the intersubband transition, whose energy follows from the choice of the well thickness $L_w = 8.3$ nm. In order to avoid an overlap between the electronic wavefunctions of adjacent wells we chose a barrier thickness $L_b = 30$ nm. Hence, the MQW approximation holds and Eqs. 1.32, 1.33 and 1.42 can be used to predict the normal mode splitting. By employing $f_0 = 1$ (good approximation for a real two-level QW), $\Gamma = 0.8$ (as it follows from the RCWA), and $\Delta n = 5 \cdot 10^{11}$ cm$^{-2}$ (from the sample nominal doping, chosen in order to safely avoid population of the second subband occurring at $\Delta n = 3.4 \cdot 10^{12}$ cm$^{-2}$), a Rabi splitting $2\Omega_R = 14.7$ meV is expected.

In Figure 3.7 measurements show that the upper photonic band of the bare photonic crystal splits in two polaritonic bands when the sample is doped. According to the lineshape inheritance concept predicted by coupled mode theory (Sect. 2.2.1), the transmittance *peak* splits in two transmittance *peaks* whose separation is a signature of the strong

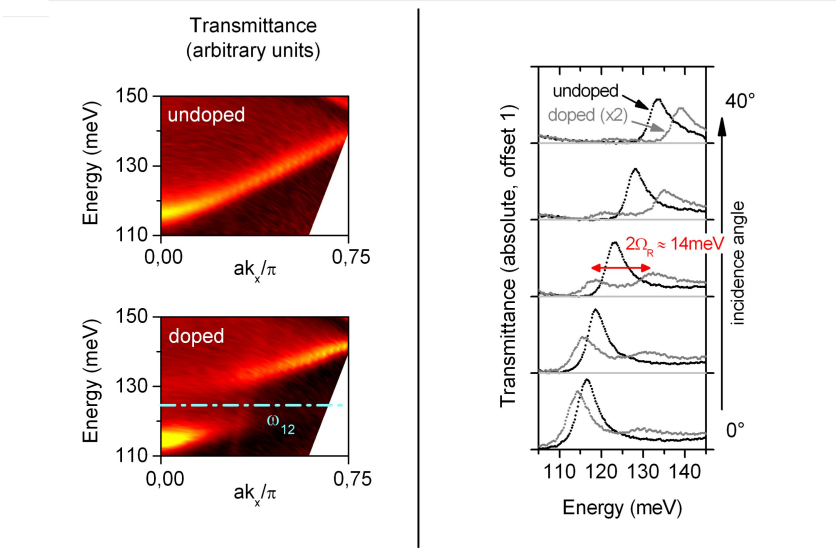


Figure 3.7: Intersubband polaritons observed in a metallodielectric photonic crystal slab. *Left panels*, angluarly-resolved transmittance measurements reveal that the photonic band splits when dopants are introduced in the wells (see also Fig. 3.1). *Right panels*, selection of fixed-angle spectra.

coupling regime. The observed peak splitting is close to 14 meV, consistent with the Rabi splitting estimated above. Actually, speaking of *Rabi splitting* neglects a set of details discussed in the theoretical chapters (Chapt. 1 and 2). First, in presence of damping – either radiative or non-radiative – the transmission peaks in general do not correspond to the polariton energy eigenvalues (Sect. 2.2.1). Second, the real splitting should be read out from the $k$-$E$ dispersion rather than from the fixed-angle spectra. Third, when the intersubband polaritons are interpreted in the ultra-strong coupling framework (Chapter 1) it turns out that the normal mode splitting is not the sole relevant quantity, while both the plasma frequency $\omega_P$ *and* the overlap factors $f_0 f_w$ should be separately considered (see Fig. 1.5 for an overview). In this approach, the original concept of vacuum Rabi frequency loses its centrality.

Anyway, these concerns can be overcome and the usual expressions can be used with consistence. First, being the transmittance peak separation sufficiently larger than the peak width, and the incidence angle sufficiently small such that the $k-$ vector mismatch between upper and lower polariton can be neglected, the first two concerns can

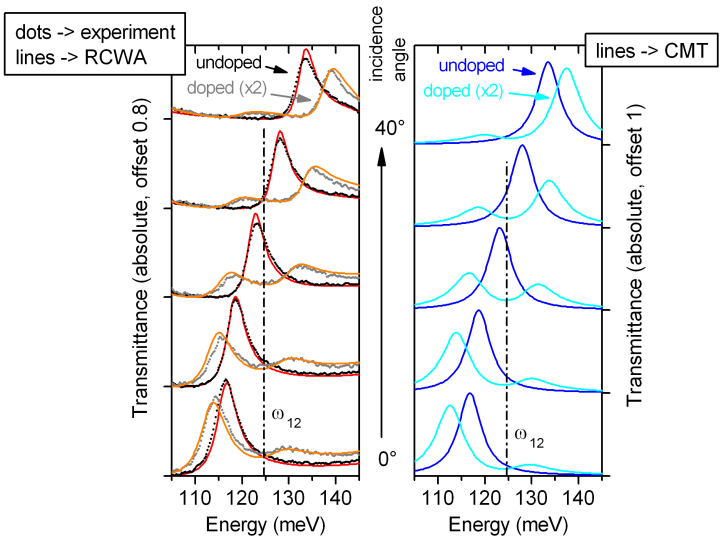


Figure 3.8: Experimental and theoretical polaritonic spectra. *Left panel*, comparison with the rigorous coupled wave analysis (RCWA); *right panel*, comparison with the coupled mode theory (CMT).

be disregarded. In addition, being the peak splitting of the order of 10 % of the ISB transition frequency, the ultra-strong coupling related concerns are of lesser importance, and the concepts of *vacuum Rabi splitting*, *minimum splitting between polaritonic branches*, and *peak splitting* can be overlapped. In essence, the data of Fig. 3.7 show the feasibility of a polaritonic sample featuring band dispersion, finite energy value at $k = 0$, and surface access, by means of a reproducible and stable fabrication process.

As it already turned out when dealing with the bare PhC slab, the realization of the polaritonic sample has been deeply guided by the RCWA simulations. Here the response of the doped QW is treated semiclassically by means of the effective medium approach outlined in Sect. 1.4: basically, the intersubband transition induces a Lorentz-like form on the component $\varepsilon_z$ of the anisotropic dielectric function of the MQW. In Fig. 3.8, left panel, we report the same set of experimental spectra shown in Fig. 3.7, with superimposed the result of the RCWA simulation. Remarkable agreement is reported, both for the undoped and the doped samples. This excellent overlap follows from a fitting procedure where the QW parameters $\tilde{\omega}_{12}$, $\gamma_{12}$ and $\Delta n$ entering Eq. 1.44

have been optimized until minimization of the root mean square difference between theoretical and experimental traces. The fitted parameters are $\hbar\tilde{\omega}_{12} = 124.6$ meV, $\gamma_{12} = 5.4$ meV and $\Delta n = 6.4 \cdot 10^{11}\text{cm}^{-2}$, in good agreement with the design parameters[18].

While RCWA is a very powerful tool for modeling multilayered periodic structures, since it basically solves Maxwell's equations for a given device geometry and dielectric response, it does not give any insight into the underlying physical mechanisms leading to the presence of resonances. A complementary description is the coupled mode theory (CMT) developed in Chapter 2, where the stress is now on the resonances themselves (photonic and intersubband ones), and on their coupling mechanisms between each other and with the far-field radiation (scattering channels). Here, the two-port theory of Sect. 2.2 applies.

Starting from the undoped sample, by considering the position and the width of the transmission peaks one directly gets $\omega_c$ and $\gamma_c = \gamma_r + \gamma_{nr}$. While $\omega_c$ sweeps from 120 to 135 meV, the half cavity linewidth is always $\gamma_r \simeq 3$ meV. The background reflectance has to be chosen $r = 0$ in order to have Lorentzian lineshapes; the fact that the experimental peaks have contrast close to unity imply with good approximation $\gamma_{nr} = 0$ and $x = 0$ (see Sect. 2.2.1). Notice that, despite the sample geometric asymmetry upon exchanging $z \to -z$, the coupling between the resonant mode and the scattering channel is *symmetric* ($x = 0$). The spectra corresponding to these parameters are reported in Fig. 3.8, right panel, as blue lines. After this fitting procedure, the polaritonic spectra of the doped sample have been reproduced by setting $\Omega = 7$ meV, $\tilde{\omega}_{12} = 124.6$ meV, and $\gamma_{12} = 5.4$ meV in the CMT equations.

The success of this independent approach[19] for interpreting the po-

[18] Indeed, before the membrane processing we ckecked whether the ISB transition parameters were compliant with the design requirements by means of ISB absorption measurements in the prism multipass geometry. We got an absorption dip centered at 121 meV with FWHM of 16 meV. While the former is fairly consistent with the RCWA-extracted value, the latter would correspond to $\gamma_{12} = 8$ meV, not compatible with the RCWA estimate. This is because the large number of QWs led to a saturated absorption lineshape. For the same reason it was not possible to estimate $\Delta n$ from the multipass-absorption measurement.

[19] Actually, the CMT polaritonic spectra are obtained with the RCWA-estimated values $\tilde{\omega}_{12}$ and $\gamma_{12}$. In principle, a fully independent approach would have relied, for example, on employing the values from multipass prism absorption, but this was not feasible (see footnote 18). Notice also that in the CMT we enter the intersubband transition frequency *with* the depolarization shift included.

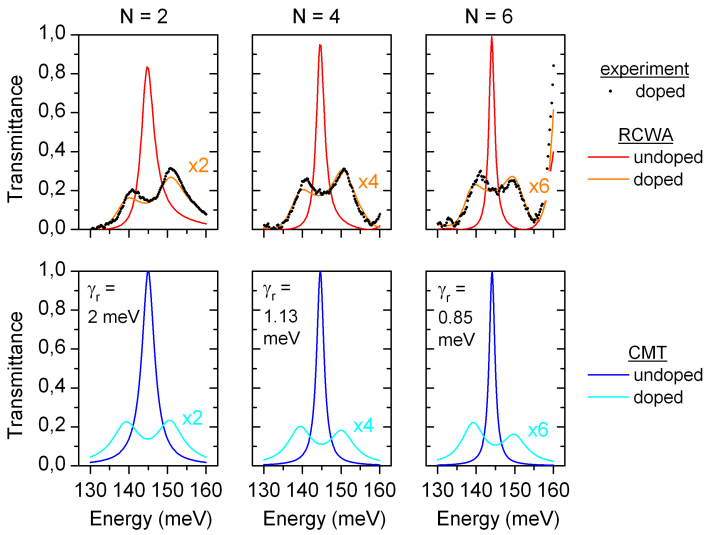


Figure 3.9: Polaritons in a defect-mode photonic crystal slab resonator. As the number of Bragg periods is varied (see also Fig. 3.5), the radiative linewidth of the photonic mode is tuned and the polaritonic contrast varies accordingly. *Top panels*, experimental data and rigorous coupled wave analysis curves; *bottom panels*, results from the coupled mode theory (CMT).

laritonic spectra justifies its use to predict whether a sample is close to the strong critical coupling phenomenon outlined in Chapter 2, and more in general gives solid grounds to the relevance of damping rate matching or mismatch in polaritonic systems.

### 3.1.4 Intersubband polaritons with defect modes

Relying on the concept of photonic band gap for waves propagating *in* the photonic crystal slab plane, in Sect. 3.1.2 we developed a device which exhibits a defect-mode photonic resonance whose radiative linewidth can be tuned within a fairly large range. Now we experimentally analyze what happens if the defect mode is brought into resonance with the intersubband transition, and observe how polaritons appear when a (large) mismatch between the radiative and the intersubband damping rates is present.

In Figure 3.9, upper panels, we report the transmittance measured from three different polaritonic samples characterized by an increasing

number of Bragg periods, which leads to a narrowing of the defect-mode transmission lineshape and hence to smaller and smaller $\gamma_r$ (see Fig. 3.5 and the related discussion). The red lines are the RCWA simulations employed at the design stage in order to tune the defect mode in resonance with the nominal intersubband transition frequency of heterostructure HM 3496 [20]. The dotted traces are the result of the transmission measurement performed on the doped sample, and the orange curves are obtained by the RCWA upon fitting of the QW parameters, which led to $\tilde{\omega}_{12} = 144.9$ meV, $\gamma_{12} = 6.4$ meV and $\Delta n = 2.39 \cdot 10^{11}$ cm$^{-2}$. Incidentally, the RCWA-fitted $\tilde{\omega}_{12}$ and $\gamma_{12}$ are here in excellent agreement with those obtained from multipass prism absorption. Apart from a slight detuning of the cavity mode, which leads to slight differences in the height of the polaritonic peaks, it clearly appears that the damping rate mismatch does not substantially affect the polaritonic splitting, while it significantly affects the transmittance contrast. This is in agreement with the general features outlined in the coupled-mode theory (Sect. 3.2.2).

Indeed, on one hand, in the coupling constant the only sample-dependent parameter is the field confinement factor $\Gamma$. As it can be deduced from Fig. 3.5, this quantity does not significantly change with the increase of the Bragg period number $N$. On the other hand, as detailed in Chapter 2, the mismatch between $\gamma_r$ and $\gamma_{12}$ (notice that $\gamma_{nr}$ is here negligible) reduces the spectral feature contrast as well as the polaritonic absorbance (not plotted here); this behaviour is quantitatively confirmed by the coupled-mode theory traces plotted in the lower panels of Fig. 3.9.

Hence, at a first glance, it appears that the development of strongly $\gamma$-mismatched cavities does not satisfy any need. This is true in the linear optical regime, where the properties of the media do not depend on the field intensity; when one instead looks at nonlinear phenomena the damping rate mismatch may enable features otherwise not attainable. In particular, in Sect. 4.1.4 we will show that the defect-mode intersubband polaritons may lead to novel ultra-sharp saturable filters and to bistable optical devices working in the mid-infrared spectral range.

[20] For this experiment we employed an heterostructure identical in all details to that described in Sects. 3.1.1 and 3.1, with the sole addition of doping in the wells.

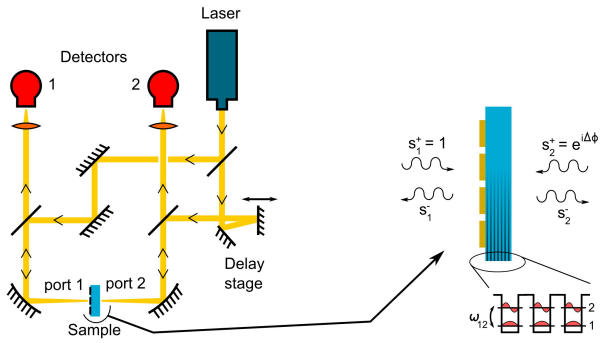


Figure 3.10: Experimental setup for double-beam probing of a polaritonic photonic crystal membrane. By means of a delay stage, the relative phase $\Delta\phi$ between the input beams can be swept, while the output beam intensities $|s_{1,2}^-|$ are recorded by the detectors.

### 3.1.5 Intersubband polariton coherent perfect absorption

In Sections 2.1.3 and 2.2.2 the concepts of *strong critical coupling* and *polariton coherent perfect absorption* have been introduced, highlighting the relevance of a situation where all the radiation incident on a polaritonic system can be completely absorbed and eventually converted into polariton quasiparticles. Strong critical coupling occurs when the photonic crystal cavity radiative damping rate is equal to the sum of cavity non-radiative damping rate plus the intersubband damping rate: $\gamma_r = \gamma_{nr} + \gamma_{12}$. We showed in Sect. 3.1.3 that the photonic crystal quasi-guided mode lying above the second-order stop-band has a radiative linewidth comparable to that of the intersubband transition: $\gamma_r \simeq 3$ meV, $\gamma_{12} \simeq 5$ meV. In the following we will show that this small damping rate mismatch does not hinder the observation of a large interferometric control of absorption. On the contrary, polaritonic coherent perfect absorption (CPA) and coherent perfect transparency (CPT) are not far from experimental reality.

In order to observe these phenomena we designed a device starting from a regrowth of the heterostructure described in Sect. 3.1.3. From this epitaxial wafer (HM3580) we fabricated a photonic crystal membrane with a photonic period such that the lower edge of the upper photonic band is resonant with the ISB transition. The sample can thus be operated at normal incidence, avoiding the necessity of non-collinear beam propagation in the double-beam setup. The opti-

cal bench layout is schematized in Fig. 3.10: it starts with an external-cavity tunable mid-infrared quantum cascade laser from Daylight Solutions, whose beam is split in two by means of a double-polished GaAs commercial wafer which acts with good approximation as a 50/50 beam-splitter. One of the two beams is directed towards the patterned side of the membrane sample, while the other reaches the semiconductor side of the membrane after passing through a path delay modulated by a moving mirror. Again, two GaAs beam-splitters are inserted in the beam paths in order to direct the radiation which exits from the two surfaces of the sample towards the detectors – two mercury-cadmium-telluride (MCT) devices cooled at liquid nitrogen temperature manufactured by Judson.

If one of the two input beams is blocked, after a proper normalization the signals read at the two detectors are the ordinary transmittance and reflectance. In Fig. 3.11 we report as colored dots the measured transmittance and reflectance spectra, unfortunately covering only the lower polariton peak due to the limited laser tuning range. A broadband measurement of the transmittance has been performed by Fourier-transform infrared spectrometry (grey trace). Very good agreement with the RCWA spectra is observed[21], while a mismatch with the coupled-mode theory appears both in transmittance and in reflectance. Indeed, CMT predicts the same reflectance for both ports[22]. The mismatch between experiment and CMT is attributed to the presence of a second photonic resonance, located at about 150 meV, analogous to the weak band observable at about 185 meV in Fig. 3.2. The presence of the second photonic resonance goes beyond the CMT developed in Chapter 2, making the actual reflectance/transmittance spectra not fully reproducible by the CMT.

However, by analyzing the absorption spectra – which are of much more relevance for our purposes – the good sample characteristics appear. Since the sample has an asymmetric response, we have to focus on the *average* single beam absorbance $(A_1 + A_2)/2$, whose vicinity to the value of $1/2$ means that the system is potentially close to CPA and CPT (see Fig. A.2 in Appendix A). This is what actually happens, as it can be deduced from the right panel of Fig. 3.11. In that plot it can be also noticed that the theoretical CMT trace is very close to the RCWA

[21] RCWA spectra are obtained by fitting over the usual parameters $\Omega_{12}, \gamma_{12}, \Delta n$ the transmission spectrum measured by FTIR spectroscopy (grey trace in Fig. 3.11).

[22] As recalled in the main text, the asymmetry parameter in the CMT has to be set to zero: $x = 0$. The other parameters entering the CMT are $\bar{\omega}_{12} = \omega_c = 124.5$ meV, $\gamma_r = 3$ meV, $\gamma_{12} = 5$ meV, $\gamma_{nr} = 0$, $\Omega = 8$ meV.

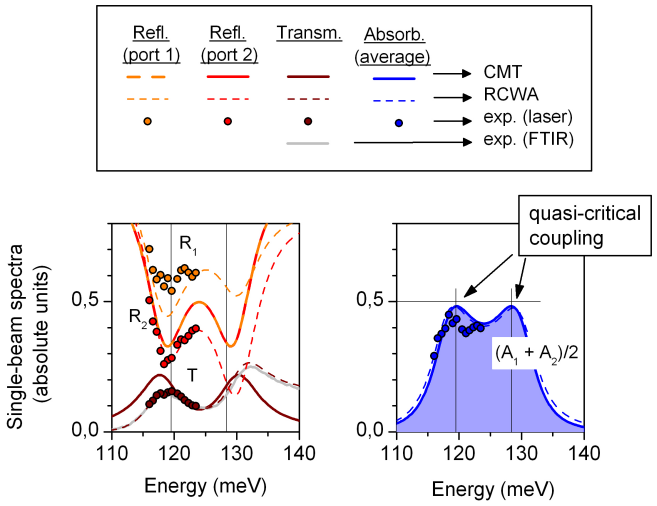


Figure 3.11: Single-beam spectra measured by means of the setup sketched in Fig. 3.10 and by means of a Fourier-transform spectrometer (FTIR). Double-beam spectra are observed both in transmittance, reflectance and absorbance. Comparison with rigorous coupled wave analysis (RCWA) and coupled mode theory (CMT) is also provided.

curve, enforcing the idea that CMT is anyway capable of describing the absorption properties of the sample despite the presence of the spurious photonic mode at about 150 meV.

Now, by turning on both input beams, coherent modulation of absorption is expected. In Fig. 3.12, left panels, we report the signal at the detectors as a function of the phase delay induced by a linear sweep of the moving mirror (a loudspeaker coil actuator driven by a triangular function generator). The signals are normalized in such a way that if there were no sample a value of 1 would have been measured[23]. In all the panels – corresponding to different laser wavelengths – a strong modulation of both individual signals and of the sum signal is observed: this is *interferometric control of absorption*, here observed for the first time in the mid-infrared range and in a polaritonic system. Again, at all the three considered wavelengths there is an input beam phase delay $\Delta\phi$ that gives an output signal close to 2: the sample is there very

[23]Clearly, in absence of sample no modulation is observed, neither in the individual signals nor in the sum signal.

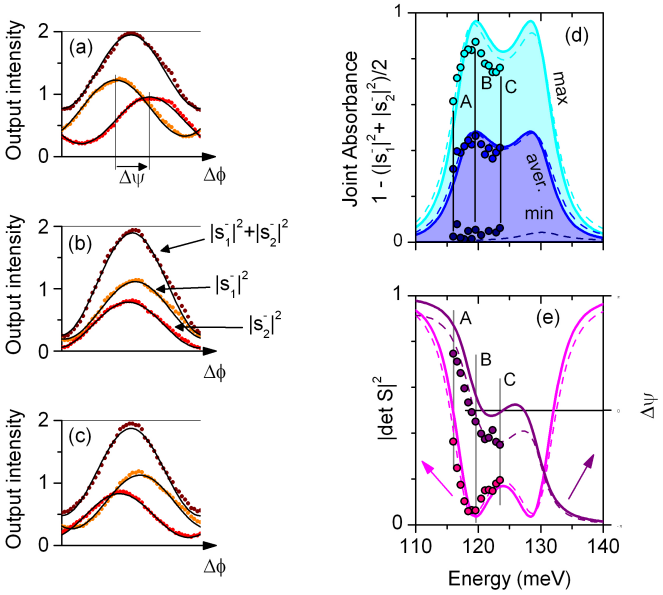


Figure 3.12: Polaritonic coherent perfect absorption and coherent perfect transparency. *Panels (a) - (c)*, individual output intensities measured at the two detectors, and total output intensity, as a function of the input beam dephasing $\Delta\phi$. The panels correspond to different laser wavelengths. The global output intensity can always reach 2, i.e. *coherent perfect transparency* (CPT), while the condition for *coherent perfect absorption* (CPA), i.e. zero total output intensity, is quasi fulfilled for the sole wavelength of panel (b). *Panel (d)*, joint absorbance spectra revealing polaritonic CPA and CPT. The points labeled *A*, *B* and C originate from the data of panels (a), (b) and (c). *Panel (e)*, spectral dependence of the scattering matrix determinant and of the output beam dephasing. The theoretical spectra in panels (d) and (e) are calculated by means of RCWA (dashed lines) and CMT (solid lines).

close to CPT. If one instead looks for an output signal close to zero, this occurs only at the wavelength corresponding to panel (b): under this condition, the sample is close to CPA. Indeed, at this wavelength the phase shift $\Delta\psi$ between the signals at detectors 1 and 2 is close to zero, while at the other wavelengths it is not – a fact that prevents the observation of CPA.

From the maximum, minimum and average output signals measured for a denser set of laser wavelengths the joint absorbance spectra

of Fig. 3.12 (d) are obtained. Very good agreement between theory and experiment is reported, enforcing the coupled-mode theory picture and revealing that the damping rate mismatch ($\gamma_r - \gamma_{12} \simeq 2$ meV) does not lead to a significant departure from polaritonic CPA. Indeed, even if exact damping rate matching was fulfilled, the intrinsic experimental limitations, which imply a systematic error[24] of about $\pm 5\,\%$, would have anyway prevented an experimental proof of "exact" CPA or CPT.

Besides the spectral dependence of the joint absorbance as a clear evidence of strong critical coupling, the very fact that the phenomena are occurring in the sample and are not spurious effects due to other components in the optical bench is provided by analyzing the spectral dependence of the phase difference $\Delta\psi$. Its peculiar dispersion is reported in Fig. 3.12 (e), showing remarkable agreement with the RCWA curve; the mismatch with the CMT is again attributed to the second photonic mode at about 150 meV. Finally, in the same panel we propose an estimate of the scattering matrix determinant based on the measured single-beam spectra and on the $\Delta\psi$ measured from the double-beam experiment[25]. Again, remarkable agreement between experiment and theory is reported; the presence of two dips close to zero is another way of viewing that the sample is close to polariton CPA. Indeed, it should be recalled that *within the CMT* the joint absorption spectra and the spectral dependence of the determinant are given by the same function (see Eqs. 2.5, 2.7, 2.22, and 2.24).

In conclusion, we have shown that strong critical coupling in a two port system, with the attendant phenomena of coherent perfect absorption, coherent perfect transparency and maximal modulation of absorption into polariton states, are close to the experimental reality of an intersubband polariton photonic crystal sample. Further RCWA simulations (not reported here) show that the slight damping rate mismatch and sample asymmetry observed in the realized device could be overcome by a more refined design of the photonic crystal resonator, potentially leading to 100 % absorption and modulation.

[24] The sources of errors in this experiment are mainly due to alignment issues. First, if the input beams are not perfectly overlapped the absorption modulation contrast diminishes accordingly. Fine alignment of input beams is performed with the help of a knife-edge beam profiler mounted in close vicinity of the sample, and allows for an estimated beam overlap not better than 90 %. Second, being the sample a non perfectly planar membrane, perfect matching with the flat incident wavefronts is not attained.

[25] As detailed in Appendix A, the equality $|\det S| = |\sqrt{R_1 R_2} e^{i\Delta\psi} - T|$ holds.

## 3.2 On-substrate metal-dielectric photonic crystal slabs

Despite the chapter starting with the analysis of the suspended-membrane photonic crystal approach, the first sample geometry that was delevoped in the doctoral work was that of a photonic crystal slab directly lying on a solid substrate. The idea of folding the unperturbed photonic crystal bands into the first Brillouin zone was actually born thinking about a perturbation of the planar, on-substrate slab waveguide design originally employed for intersubband polariton devices (Fig. 1.6). Although the suspended membrane system is fairly better since it entails larger field confinement and larger lineshape contrast, and since the strong critical coupling – which is perhaps the most relevant result of the doctoral work – was observed on that platform, the on-substrate photonic crystal system still deserves some interest. First, from an "historical" point of view: the success in observing polaritons in the on-substrate photonic crystals motivated us to develop the more complicated processing of the suspended membrane. Second, because the phenomenon of *lineshape inheritance* was observed already in this configuration, giving a further confirmation of the predictive character of the coupled-mode theory developed in Chapter 2.

### 3.2.1 Photonic resonances and lineshape tuning

In this Section we deal with the bare photonic crystal resonance observed in a sample without quantum wells. The sample is schematized in Fig. 3.13 (a): the semiconductor layer which was a suspended membrane in Fig. 3.1 now lies on a low-index $Al_{0.95}Ga_{0.05}As$ cladding layer which optically separates the first layer from the high-index GaAs bulk substrate. Optical characterization can still be performed in transmittance after polishing of the wafer back side. The thicknesses of the layers, both core and cladding, are again of the order of 2 μm.

We will here mainly focus on the aspect of *lineshape tuning*, i.e. the phenomenon which leads to a span of the Fano lineshape manifold predicted by the coupled mode theory (Sect. 2.2.1) upon a simple sweep of a single geometric parameter in the sample. This parameter is the ratio $f = b/a$ between the metal stripe width and the photonic crystal lattice spacing: in Fig. 3.13 (b) we report a set of spectra corresponding to different metal patternings realized on the same piece of heterostructure. When $f$ is increased (see Table 3.1 for the actual val-

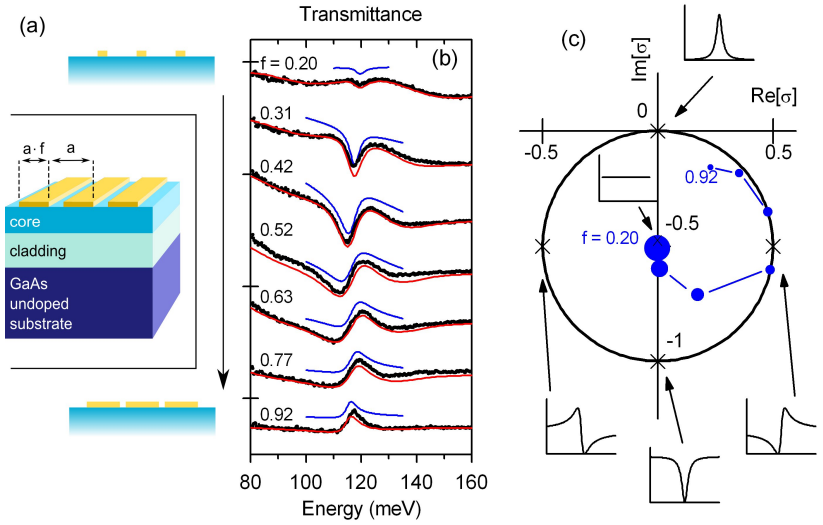


Figure 3.13: Lineshape tuning observed in an on-substrate photonic crystal slab. As the metal fill fraction $f$ is tuned, the resonance shows up as a dip, a peak, or a hybrid lineshape. This is interpreted by means of a simple-pole function, whose key parameter $\sigma$ (see Eq. 3.3) describes a spiral in the complex plane.

ues of $f$), the photonic resonance transmittance spectral feature sweeps from a dip to a peak, passing through asymmetric shapes.

Superimposed with the experimental spectra (black dots) we plot the spectra obtained by RCWA with no fitting parameters[26] (red lines). After having noticed an excellent agreement between RCWA and the experiment, let us focus on the blue curves slightly offset from the other spectra. These are the result from a fit obtained with the following analytic formula:

$$T(\omega) = \left| \frac{\bar{r}}{\omega - \omega_c - i\hbar\gamma_c} + \bar{s} \right|^2 + \tau \frac{\omega - \omega_c}{\gamma_c} = |\rho|^2 \frac{|1 + \sigma(\epsilon - i)|^2}{\epsilon^2 + 1} + \tau\epsilon. \tag{3.3}$$

This is the most general simple-pole transmittance function (plus a linear background), and was introduced for interpreting the experimental data when the coupled mode thory of Sect. 2.2 was not already

[26]The lattice spacing $a$ was here determined independently by stylus profilometry, while the values of $f$ descend from scanning electron microscopy.

| $f$ | $\omega_c$ meV | $\gamma_c$ meV | $\lvert\rho\rvert^2$ | Re$[\sigma]$ | Im$[\sigma]$ |
|---|---|---|---|---|---|
| 0.20 | 119.5 | 1.94 | 2.79 | -0.002 | -0.51 |
| 0.31 | 117.7 | 2.13 | 1.59 | 0.007 | -0.60 |
| 0.42 | 116.5 | 3.57 | 0.73 | 0.17 | -0.71 |
| 0.52 | 116.1 | 4.71 | 0.30 | 0.49 | -0.60 |
| 0.63 | 116.8 | 4.28 | 0.24 | 0.48 | -0.35 |
| 0.77 | 117.1 | 3.66 | 0.20 | 0.35 | -0.18 |
| 0.92 | 115.7 | 2.38 | 0.17 | 0.23 | -0.16 |

Table 3.1: Fitted parameters of Fano lineshapes.

developed. Apart from $\tau$, which quantifies the influence of the linear background, the above lineshape function depends on the three real parameters $|\rho|^2$, Re$[\sigma]$ and Im$[\sigma]$, where $\rho = \bar{r}/\gamma_c$, $\sigma = \bar{s}/\rho$ and $\epsilon = (\omega - \omega_c)/\gamma_c$. The fitting values corresponding to the different samples are reported in Tab. 3.1 and, pictorially, in Fig. 3.13 (c): a spiral-like path in the complex $\sigma$ plane is observed. We constrained $\sigma$ to lie inside the highlighted circumference, although there is a one-to-one correspondence between points lying inside and outside. Indeed, if we call $\delta/2$ the distance from the center of the circle, the substitutions $\delta \to 1/\delta$ and $|\rho|^2 \to |\rho|^2\delta^2$ keep the lineshape unaltered. The points on the circumference correspond to lineshapes which have a zero, and the further assumption $|\rho| = 1$ entails a fully-contrasted lineshape.

One may now wonder whether there is a connection between this formalism and that of Sect. 2.2. Actually, the transmittance lineshape of Eq. 3.3 is equivalent to that obtained from Eqs. 2.20 – 2.21, with the correspondences

$$\begin{aligned} r^2 &= 1 - |\rho|^2 \left(\mathrm{Re}[\sigma]^2 + \mathrm{Im}[\sigma]^2\right) \\ x^2 &= 1 - \frac{\mathrm{Re}[\sigma]^2}{\mathrm{Im}[\sigma]^2}\frac{1-r^2}{r^2} \\ \left(1 + \frac{\gamma_{nr}}{\gamma_r}\right)^2 &= \frac{1 - r^2x^2}{|\rho|^2}. \end{aligned} \tag{3.4}$$

If these relations were applied to the data of Table 3.1, negative values of $\gamma_{nr}$ occur, and this is in contrast with the physical meaning of that parameter. Indeed, $\gamma_{nr}$ was introduced for quantifying the nonresonant photon losses into channels other than the two scattering ports – here, the plane waves propagating orthogonally with respect to the

sample surface. A possible explanation of this incoherence is the following: here, apart from the losses in the metal which are negligible[27], the photon undergoes diffraction into the substrate. Since the diffraction efficiency may depend on the photon energy, especially when it is close to the diffraction threshold[28], the coupled mode theory may have troubles when trying to describe with $\gamma_{nr}$ a frequency-dependent loss mechanism. This may be the reason why the parameters in Table 3.1 would lead to negative $\gamma_{nr}$'s, and why we needed to add the term $\tau\epsilon$ in Eq. 3.3. This last mismatch with the coupled mode theory of Sect. 2.2 may also be due to the non-ideal behaviour of the resonator in the case $f \to 0$. Indeed, while in the coupled mode framework a sample with $f \to 0$ should have a flat transmittance (no excitation of quasiguided mode photonic resonances), the spectrum in Fig. 3.13 corresponding to $f = 0.2$ reveals that there are some residual background fluctuations happening on an energy scale of 40 meV. These can be ascribed to Fabry-Pérot – like resonances of the multilayer dielectric, hence to further resonant degrees of freedom which are not correctly described by the coupled mode theory. Anyway, it turns out that Eq. 3.3 is able to describe the resonance lineshape with a simple-pole response function, hence agreeing with very general assumptions in the linear-response theory.

In the above, the discussion about the lineshape tuning was limited to spectra measured under normal-incidence conditions; however, the phenomenon has been observed across the whole dispersion of the photonic mode within the first Brillouin zone. As it can be noticed from Fig. 3.14, the dip (peak) in transmittance observed at normal incidence ($k_x = 0$) splits into two spectral features which have the same character. When a small fill factor is considered (left panel), one observes two dark bands over a bright background, while the reverse occurs for a large fill factor (right panel). It is also interesting to notice that the bands merge at the center of the Brillouin zone, without the

[27] This can be proved by RCWA.

[28] Recalling that the diffraction threshold is given, in terms of the vacuum wavelength $\lambda$, by $\lambda < a\sqrt{\varepsilon_{sub}}$, one gets a photon energy of about 101 meV (being the period $a = 3.75$ μm and the substrate permittivity $\varepsilon_{sub} = 10.7$), to be compared with the resonance frequencies $\simeq 115 \div 120$ meV (see Table 3.1). Indeed, this does not happen by chance. Relying on the zero-order perturbation theory (Eq. 3.1), the photonic resonance occurs at wavelengths $\lambda \simeq a\sqrt{\varepsilon_{\mathrm{MD}}}$ or $\lambda \simeq a\sqrt{\varepsilon_{\mathrm{AD}}}$, depending on the metal fill fraction $f$. Here, since the core and cladding layers have permittivities close to each other, and slightly smaller than those of the substrate, the values of $\varepsilon_{\mathrm{MD}}$ and $\varepsilon_{\mathrm{AD}}$ are similar and slightly smaller than $\varepsilon_{sub}$. Hence, for any $f$ one gets a resonance frequency slightly larger than the diffraction threshold into the substrate.

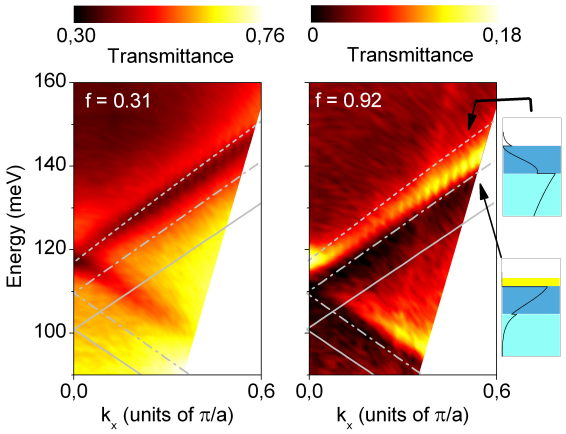


Figure 3.14: Photonic band dispersion observed in two on-substrate samples which differ by the metal stripe fill factor. The grey lines represent the guided modes of the corresponding planar slab waveguide, both in absence of the top metallization (dashed line) and in its presence (dash-dotted line). The solid grey line represents the diffraction threshold into the bulk substrate.

gap which characterized the suspended membrane samples studied in the previous Section. This can be attributed to the scarce contrast between the effective indices of the air-dielectric and metal-dielectric equivalent waveguides (see Sect. 3.1.1 for the definitions): as it can be noticed from the grey lines in Fig. 3.14, these two modes are very close to each other, and very close to the photonic resonance.

### 3.2.2 Intersubband polariton lineshape inheritance

Having developed a photonic crystal slab resonator featuring a transmittance peak or dip in correspondence to the resonant mode, we now experimentally prove that when the mode is brought into resonance with an intersubband transition the spectral feature splits into two, inheriting the original lineshape. At first glance, the splitting of a transmission *peak* is somewhat surprising, since the presence of two *peaks* in correspondence to the resonance of a lossy system (the doped quantum wells involve absorption) contrasts with the idea of energy loss. However, this phenomenon is not new in the physics of strongly coupled system; rather, it is not common when dealing with semiconductor structures. In atomic physics, a historical experiment

showed that the transmittance of a strongly coupled cavity features two peaks [Thompson92]. Indeed, the general coupled-mode theory of Sect. 2.2 suggests that both peaks and dips, either in trasmittance or in reflectance, are signatures of the strong coupling, and that the presence of peaks does not conflict with energy conservation. Indeed, the peak and dip heigths are such that the overall absorption is always positive and features a double-peak spectrum, which is the actual signature of coupling to polariton states.

Here we consider a set of samples, relying on the same scheme of Fig. 3.13, and fabricated on the heterostructure HM 3014 whose "core" layer consists of a multi-quantum well featuring 50 repetitions of GaAs and $Al_{0.33}Ga_{0.67}As$ layers with thicknesses 8.3 nm and 30 nm; doping in the wells provides the electrons needed for the light-matter coupling. The samples are arranged in two subsets: the first is characterized by a small metal fill fraction ($f \simeq 0.4$), while in the second $f \simeq 0.8$. Each subset consists of 9 patterned regions which differ by the period $a$: in such a way, the photonic resonance accessible at normal incidence is tuned across the intersubband transition. In Fig. 3.15, panels (a), (b) and (c), we report the spectra pertaining to the $f \simeq 0.4$ samples, while panels (d), (e) and (f) correspond to $f \simeq 0.8$. More in detail, in panels (b) and (e) we clearly observe the polaritonic anticrossing between dips or peaks, both from the experiment (black dotted traces) and from the RCWA simulations (orange lines). These simulations have been performed with no fitting parameters, as the geometrical parameters have been obtained from microfabrication techniques[29] and the intersubband transition parameters ($\tilde{\omega}_{12}$, $\Delta n$ and $\gamma_{12}$) have been extracted from an independent measure of polaritonic dispersion on an ATR-based prism sample (see Fig. 1.6 and the related discussion). The lineshape inheritance phenomenon clearly appears by comparing these spectra with those reported in panels (a) and (b), which follow from a RCWA run with $\Delta n = 0$.

Further confirmation of the coherence of this picture is gained by analyzing the polariton eigenfrequencies predicted by the Hamiltonian theory of Chapter 1, and the absorption spectra calculated by RCWA. At first, we fitted with Eq. 3.3 the bare resonator lineshape [panels (a) and (d)], getting the resonance frequencies $\omega_c$ for each sample; these are indicated in the figure by vertical ticks superimposed to the spectra. A RCWA run performed at the resonance frequencies provided then the overlap factor between the field and the MQW: these are the

[29] Stylus profilometry and SEM have been employed.

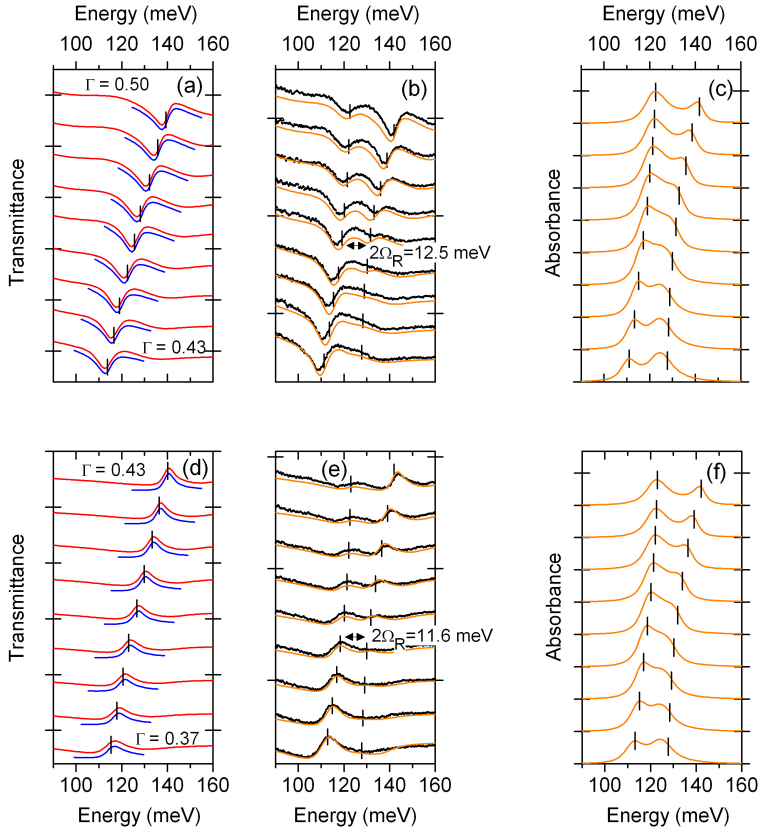


Figure 3.15: Intersubband polariton lineshape inheritance. In small-$f$ samples the bare photonic spectral feature observed in transmittance is a dip *[panel (a)]*, and evolves in a dip doublet when the intersubband transition is activated *[panel (b)]*. In large-$f$ samples the reverse is observed. Nonetheless, the absorbance spectra are always double-peaked *[panels (c) and (f)]*.

$\Gamma$ values reported in the graphs[30]. With these ingredients, the polaritonic eigenfrequencies are calculated according to Eq. 1.41, and reported in panels (b) and (e) as vertical ticks for comparison with the transmittance spectra: notice the correspondence between the spectral peak/dip and the tick. Finally, in panels (c) and (f) we report the calculated absorption spectra for the two series of samples. Here it clearly

[30]Notice that the overlap factor is here smaller with respect to those observed in the suspended-membrane photonic crystals: while there we observed $\Gamma \simeq 0.8$, here $\Gamma \simeq 0.4 - 0.5$.

appears that the absorption has always two anticrossing *peaks*, coherently with the coupled-mode theory.

This closes the circle embracing the three theoretical interpretations – Hamiltonian, coupled-mode theory, and the Maxwell equation approach with dispersive medium (implemented with the RCWA) – and the experimental observations.

## 3.3 Double-metal photonic crystal resonators

In this Section we are going to deal with a third species of metallo-dielectric photonic crystal slab resonances, i.e. those of a double-metal photonic crystal resonator. The double-metal geometry relies on the basic metal-insulator-metal (MIM) planar waveguide, which is also the base for engineered components in microwave technology (strip transmission lines [Pozar12]) and one of the possibilities for realizing the resonant cavity of the terahertz quantum cascade laser (THz QCLs [Williams03]).

The MIM waveguide has the strong advantage of being able to support a propagating mode at arbitrarily large wavelengths, without losing confining efficiency. This is the TEM mode, which behaves exactly as a plane wave, despite being confined along one direction on a scale that can be much smaller than the wavelength. Clearly there is a drawback, namely the losses in the non-ideal metal layers which sandwich the dielectric where the radiation is confined. However, it turns out that – at least in the spectral range spanning from the microwaves to the far infrared – this technology is the most convenient, as it is witnessed for instance by the widespread development of THz QCLs based on this approach.

Looking at the THz QCLs literature, starting from the plain MIM waveguide concept, more refined photonic resonator designs have been developed. As an example, 1-d or 2-d photonic crystal approaches have been succesfully attempted, with substantial improvements mainly on the far-field pattern [Fan06, Chassagneux09]. The far-field is governed by the near-field of the lasing mode, which is in turn dictated by the arrangement of the photonic crystal unit cell (or better, in general, supercell). Here, the main feature we are looking for is rather the dispersion of the photonic mode within the Brillouin zone: if a dispersion like that usually observed in exciton-polariton samples was attained, certain experiments like polariton luminescence or stimulated emission could be favored by the polariton bottlenecking occurring in the lower

branch [Tassone97].

Being the dispersion of the photonic mode a requirement, one may wonder why an approach like that of Sect. 3.1.1 – which leads to the required dispersion – has not been applied. The problem is the scalability of the semiconductor epitaxial layer thicknesses: recalling that the target photon energy was there $\simeq$ 100 meV, and the needed thickness of the guiding layer was $\simeq$ 2 μm, an analogous device working at $\simeq$ 10 meV (i.e. within the usual band for THz research devices) would require 20 μm of epitaxy, out of the practical range for molecular-beam epitaxy (MBE). Hence we focused on a device consisting on a dielectric layer of thickness $\simeq$ 10 μm, wafer-bonded to a substrate via a gold layer (which acts as back-mirror, i.e. as one of the metal claddings of the MIM waveguide), and patterned with gold stripes on the top surface. The choice of 10 μm for the dielectric layer allows to stay within the typical MBE thickness range for QCL-like devices, and meanwhile entails a dispersive photonic band structure. If the guiding layer thickness was instead reduced to $\simeq$ 1 μm, the photonic dispersion would have been lost, substantially making the device to be an array of patch cavities.

In samples based on patch cavities, whose resonance properties have been widely explored in the literature [Jouy11b, Todorov10b], intersubband polaritons have been observed both in the mid-infrared and in the THz spectral ranges [Jouy11a, Todorov09, Todorov10a]. However, a direct translation of an intersubband polariton device working at THz frequencies from the patch cavity framework to that of a dispersive MIM photonic crystal cavity turned out not to be straightforward. Indeed, a first set of RCWA simulations showed that the photonic peak essentially disappeared upon introduction of the QW response. It was this observation that actually triggered the need to understand the role of damping rate mismatch between the cavity and the ISB transition, and which led us to develop the coupled-mode theory of Chapter 2. As a matter of fact, patch cavities in the THz range have a resonance full-width of $\simeq$ 2 meV, mostly matched with the typical full-width of intersubband transitions occurring in that spectral region ($\gamma_{12} \simeq 4$ meV). On the other hand, the photonic resonance of a dispersive MIM cavity simply obtained by increasing the thickness of the dielectric layer of the patch-cavity design has a very narrow linewidth, of the order of 0.1 meV: when this is brought in resonance with the intersubband transition, no clear polaritonic features appear. Hence, if one looks for clearly contrasted polaritonic features – and for concurrent large po-

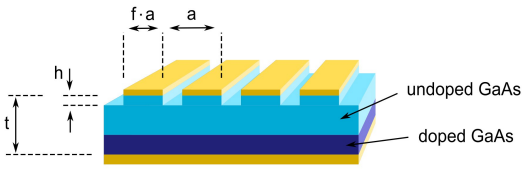


Figure 3.16: Schematic of a double-metal photonic crystal slab. The etching between the metal stripes induces a variation of the radiative coupling efficiency.

laritonic absorption – a mechanism for tuning the radiative decay rate of the dispersive MIM cavity is needed.

### 3.3.1 Radiative decay rate tuning and critical coupling

The ability to tune the radiative decay rate of a cavity working at THz frequencies which can embed an active region has a relevance both in view of polaritonic devices and when the intended application entails the weak light-matter coupling regime. For instance, this is the case of a radiation detector, where the active region is a broadband photon absorber. In this Section we focus our attention on the device schematized in Fig. 3.16, which implements this concept. A GaAs dielectric layer of total thickness $t = 10$ μm is sandwiched between a metal layer on the bottom and an array of metal stripes on the top. A 1 μm thick GaAs layer close to the bottom metal is doped with a nominal electron density of $n = 2.6 \cdot 10^{18}$ cm$^{-2}$, hence acting as a Drude conductor with a plasma frequency $\hbar\omega_P \simeq 70$ meV; it is this region which mimicks the detector active region, and which acts as a "probe" for the damping rate of the device. In this geometry, the radiative damping rate is tuned by progressively etching until $h \simeq 5$ μm the undoped semiconductor regions between the metallic stripes, by means of inductively-coupled plasma reactive ion etching (ICP-RIE). This technique defines vertical walls in correspondence to the metal stripe edges. Since the metal stripes have to act as a mask against the chemical attack (from the top), and simultaneously as a low-loss boundary for the electromagnetic field (from the bottom), their fabrication relies on a metallic bilayer based on gold and chromium.

The procedure of progressive etching allowed us to optically characterize the same sample at various etching depths $h$. In Fig. 3.17, left panels, we report the photonic bands obtained by angle-resolved re-

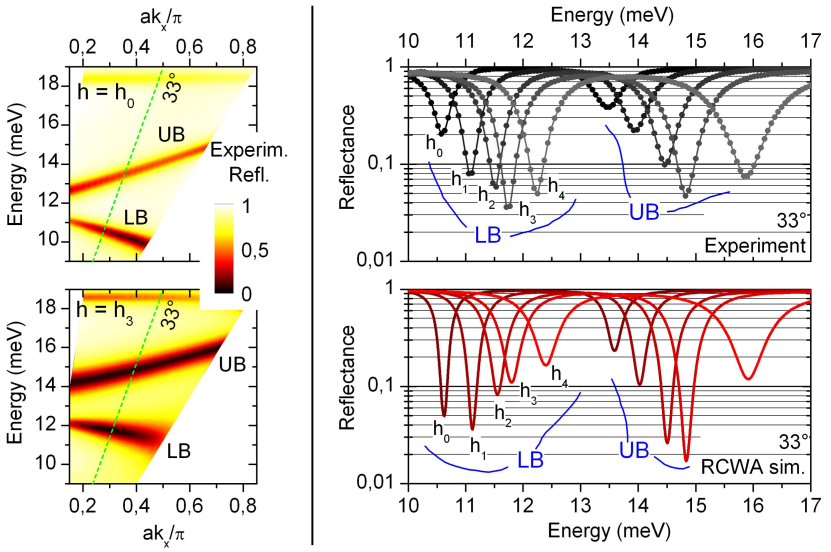


Figure 3.17: Photonic bands of a double-metal photonic crystal slab, and radiative tuning coupling. *Left panels*, angularly-resolved reflectance measurements taken from the sample before any etching ($h = h_0 = 0$) and after a number of etching steps ($h = h_3$). A lower and an upper photonic band are observed (LB and UB), whose coupling (i.e. the reflectance dip strength) is modified by the etching. *Right panels*, details of the effect of etching on the photonic bands observed at a fixed incidence angle. The minimum reflectance (reflectance at dip energy) first decreases and eventually increases

flectance measurements[31] on a sample having $a = 30$ μm, $f = b/a = 77\,\%$, for the two etching depths $h = h_0 = 0$ and $h_3 \simeq 3.25$ μm. Clear dispersive photonic bands are reported, with the upper and lower bands originating from the folding in the first Brillouin zone of the TEM mode of the MIM waveguide (Eq. 3.1 with $\bar{\varepsilon} = \varepsilon_{\mathrm{TEM}} \simeq \varepsilon_{\mathrm{GaAs}}$, where the last approximation stems from the presence of the doped layer and from the non-ideal behaviour of the real metal). The bands are here formed by reflectance spectral dips, according to the general coupled-mode theory for a one-port resonator (Sect. 2.1). Indeed, when the incident light is off-resonance, the homogeneous back metal acts as

[31] For this purpose we employed a Fourier-transform interferometer in vacuum manufactured by Bruker, equipped with an external Silicon bolometer cooled at liquid helium temperature, and with an automated inset for measuring reflection at variable angles. The plane of incidence was orthogonal to the metal stripes, and *p*-polarized light was employed.

a mirror, while upon resonance the reflectance dip is the counterpart of absorption, either in the metal or in the doped semiconductor. Notice that, given the subwavelength photonic period, no diffraction losses are involved. By comparing the two band-structures, it can be noticed that passing from $h_0$ to $h_3$ the dispersion of upper and lower branches (UB and LB) is diminished, and – most importantly – the reflectance at resonance is brought close to zero. This is the proof that etching brings the resonator closer to the critical coupling condition.

This effect is systematically explored by considering the evolution of the spectra at a fixed angle upon a fine sweeping of the etching depth. In Fig. 3.17, upper right panel, we show the experimental reflectivity obtained at an incidence angle of 33° for increasing etching depths $h = h_0 \dots h_4$: both UB and LB resonances show a continuous increase of the linewidth, while the reflectance at resonance first decreases and eventually increases. The passing through a reflectance minimum suggests that the critical coupling condition is being crossed, as it will be eventually confirmed by analysing the data by means of the coupled mode theory. Before going for that, we would like to stress once again that the RCWA simulations, performed with no fitting parameters[32], offer a very accurate prediction on the sample response, both in terms of resonance position, linewidth, and contrast (Fig. 3.17, bottom right).

The idea of tuning the radiative coupling efficiency by means of etching turned out to be very effective, in that – as it can be deduced from Fig. 3.17 – it is possible to couple more than 90 % of the incident light into the resonator[33]. We will now quantitatively interpret these

[32]The geometric parameters $a$ and $f$ have been measured by optical microscopy; the epilayer thicknesses are the nominal ones, and the etching depths have been measured by SEM (see [Manceau13] for details). The THz response of the GaAs undoped layer contains the phonon contribution:

$$\varepsilon_{\mathrm{GaAs}} = \varepsilon_\infty \left(1 + \frac{\omega_L^2 - \omega_T^2}{\omega_T^2 - \omega^2 + i\omega\gamma_{ph}}\right),$$

with $\varepsilon_\infty = 11$ and the other parameters taken from [Palik91]. The doped GaAs layer is modeled as a Drude-like metal:

$$\varepsilon_{dop} = \varepsilon_\infty \left(1 - \frac{\omega_P^2}{\omega^2 + i\omega/\tau}\right),$$

with $\omega_P^2 = ne^2/\varepsilon_0\varepsilon_\infty m^*$, $n$ being the volume electron density provided by the nominal doping and $m^* = 0.067m_0$ the effective mass in the conduction band. The response of gold is taken from [Ordal83].

[33]It can be shown by RCWA that among this energy fraction less than 10 % is absorbed

results in terms of the coupled mode theory for a resonator featuring non-radiative, non-resonant losses (Eq. 2.15). This formula describes a reversed Lorentzian, whose full width at half maximum and whose minimum value (reflectance at resonance) are experimentally accessible quantities (as opposed to the individual radiative and non-radiative damping rates, $\gamma_r$ and $\gamma_{nr}$). If we name $2\bar{\gamma}$ the measured reflectance dip FWHM, and $\bar{R}$ the measured reflectance minimum, the following equivalences hold:

$$\begin{aligned} \bar{\gamma} &= \gamma_r + \gamma_{nr} \\ \bar{R} &= \left( \frac{\gamma_r - \gamma_{nr}}{\gamma_r + \gamma_{nr}} \right)^2 . \end{aligned} \tag{3.5}$$

From a dataset like that of Fig. 3.17, a set of points $(\bar{\gamma}, \bar{R})$ can hence be extracted. Actually, we had at our disposal several datasets like the above, each of them pertaining to a sample having a different fill factor $f$, and/or measured at a different incidence angle $\theta$. We have not plotted the spectra from which these datasets originate, since their appearance is very close to that reported in Fig. 3.17.

At this stage, we wondered whether it was possible to plot all these sets of points $(\bar{\gamma}, \bar{R})$ in a single graph, and to compare them with a universal function. The answer is positive, and relies on the hypothesis that when a given "sample" (i.e. a given combination of $f$ and $\theta$) is etched, the non-radiative damping rate is unchanged. Hence, if we define the *critical coupling damping rate* $\gamma_{cc} = 2\gamma_{nr}$ (i.e. $\gamma_{cc}$ is the *total* damping rate expected in conjunction with zero reflectance, Eqs. 3.5 becomes

$$\bar{R} = \left( \frac{1 - \bar{\gamma}/\gamma_{cc}}{\bar{\gamma}/\gamma_{cc}} \right)^2 . \tag{3.6}$$

Now, by fitting with respect to $\gamma_{cc}$, the points $(\bar{\gamma}/\gamma_{cc}, \bar{R})$ are expected to lie on the universal curve $y = ((1-x)/x)^2$. The result of this procedure is reported in Fig. 3.18. A very good agreement over a wide range of $\bar{\gamma}/\gamma_{cc}$ is reported, clearly showing the transition between undercoupling and overcoupling, passing through critical coupling. While the agreement is excellent in the region of small $\bar{\gamma}/\gamma_{cc}$'s, when $\bar{\gamma}/\gamma_{cc} > 0.9$ a slight mismatch between experiment and theory is observed. On the one hand, the experimental points close to $\bar{\gamma}/\gamma_{cc} = 1$ indicate a coupling efficiency slightly worse than the expected one, despite the fact that the theoretical curve has been offset upwards by the value 0.015

by the gold.

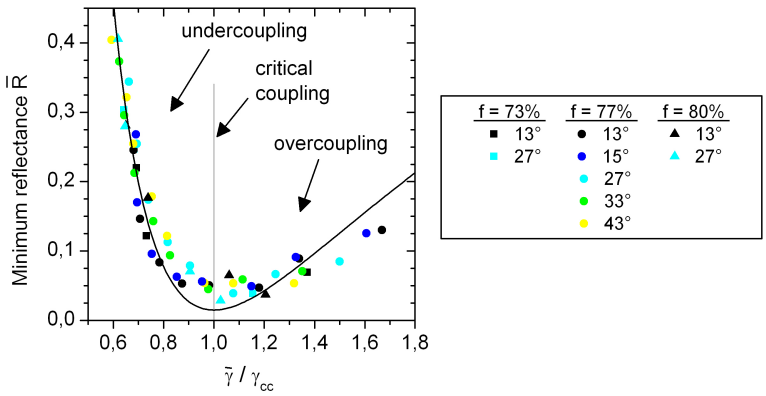


Figure 3.18: Universal trend of the mimimum reflectance $\bar{R}$ observed in different datasets (different fill factors $f$ and incidence angles). For each dataset, the sole physical parameter varied is the etching depth $h$, which influences the radiative damping rate and eventually the total damping rate $\bar{\gamma}$. When $\bar{\gamma}$ matches the critical coupling damping rate $\gamma_{cc}$, zero minimum refectance is expected. The slight shift of the theoretical curve from a full zero accounts for a known small leakage through the polarizer (see text for details).

in order to keep into account the measured non-ideality of the polarizer. On the other hand, the points corresponding to overcoupling ($\bar{\gamma}/\gamma_{cc} > 1.4$) indicate that the theory overestimates the coupling efficiency. Both these observations can be attributed to the approximate validity of the assumption that $\gamma_{nr}$ does not depend on the etching depth. This hypothesis, that at first glance may seem quite strong, is anyway supported by the observation that the resonant field is confined close to the bottom metal of the photonic crystal slab[34], and hence that the etching does not imply major redistribution of the field out of the active (absorbing) doped semiconductor layer.

Anyway, having reproduced the global trend and having demonstrated that about 90 % of the incident radiation is coupled into the device active region confirms that the idea of tuning the radiative coupling by progressive etching can be of significant help in designing THz dispersive cavities for active devices like detectors.

In addition, being the system an excellent *absorber*, the Kirchhoff's law of thermal radiation[35] implies that the same system is also an ex-

[34]This has been proved by RCWA; for a field plot, see [Manceau13].

[35]This states that the emissivity of a body at thermal equilibrium is the same as absorp-

cellent *thermal emitter*. For this reason, one of the samples has been heated and its radiation spectra measured by FTIR[36]. Being $E(\omega)$ the experimental emission trace, an excellent agreement is observed with respect to the experimental "absorption" curves $A(\omega) = 1 - R(\omega)$, hence confirming the picture that the dips in reflectance actually correspond to radiation being absorbed in the cavity and not to scattering into other radiation channels. In addition, the effect of the etching clearly appears also in this framework as an increase in the emissivity. Hence, this approach can have a role in the development of efficient terahertz or infrared thermal emitters with tailored spectral features.

## 3.4 Conclusions

In this Chapter we reported about intersubband polariton states observed in photonic crystal slab samples. The operating principles of these devices has been deeply understood both by means of the Hamiltonian microscopic theory, by numerical electromagnetic simulations (rigorous coupled wave analysis), and by a coupled-mode model.

It is especially within the last framework that we were able to interpret most of the data, in terms of damping rate matching/mismatching between the subsystem's decay rates. In particular, we showed that when the cavity decay rate is sufficiently close to the transition decay rate, a complete tuning of the absorption of polariton states is possible. This is to our knowledge the first report of *polariton coherent perfect absorption*. On the opposite side, as far as the decay rate mismatch is increased, it is more and more difficult to couple light into the polariton states, and hence to detect their spectral features. The above properties have been observed in delocalized or localized (defect-mode) resonances of a suspended membrane photonic crystal slab. While these behaves – within the coupled-mode theory – as prototypical symmetric two-port systems, if the focus is moved towards the *on-substrate* geometry the curious phenomenology of *polariton lineshape inheritance* appeared. Finally, we introduced a fine tuning tool for the radiative decay rate in a double-metal photonic crystal cavity, which can be the basis of efficient terahertz devices working in critical coupling.

In addition, the peculiar polariton dispersion which follows from

tivity. Hence, if a structure which has the absorption peaking at 1 at a given wavelength is heated, its thermal radiation spectrum has a peak – limited by the blackbody spectrum – at that exact wavelength.

[36] This experiment has been performed by J.-M. Manceau and R. Colombelli.

the photonic crystal modal dispersion could be the key for implementing devices where the scattering processes between polariton states require precise conditions on the momentum-space distribution of the involved modes. Furthermore, the absence of a bulk substrate which characterizes the membrane sample geometry is a strength point in view of experiments involving an ultrafast modulation of the light-matter coupling strength.

# Chapter 4

# Ultrafast spectroscopy and non-linear properties of intersubband polaritons in photonic crystal resonators

When a system is excited with a large intensity, significant departure from the ground state is likely to occur. In the intersubband polariton framework, two main interesting phenomena have been theoretically predicted. First, if the upper polariton branch is populated with a sufficient density of quasiparticles, polariton-polariton scattering processes are expected. Second, if the light-matter coupling constant is modulated on a time scale comparable to the inverse Rabi frequency, the emission of photons from the polariton vacuum state can be achieved.

The first phenomenon is the basis for an *intersubband polariton laser* [De Liberato09c]. While such a device is still far from experimental reach, the understanding of the scattering mechanisms involved are getting explored since a couple of years, mainly by means of electrical pumping [Delteil11]. In Sect. 4.1 we will instead analyze the behaviour of intersubband polaritons upon resonant optical pumping. Being the spectral width of the laser at our disposal too wide, no polariton-polariton scattering phenomena was observed, but rather the *polariton bleaching* appeared. Polariton bleaching, i.e. saturation and collapse of polariton states, actually deserves both intrinsic and potential interest.

First, it allowed to estimate the polariton saturation threshold, and to state that an optically pumped polariton laser is compatible with the requirement of a pumping that does not destroy the polariton states themselves. Second, it triggered the curiosity to explore other arrangements involving non-linear polariton dynamics, and it turned out that ultrasharp saturable filters, or bistable devices, can be realized upon a judicious design of a defect-mode polariton resonator (Sect. 4.1.4).

A route towards the observation of vacuum radiation phenomena is outlined in Sect. 4.2. As anticipated in the above, the virtual photons "contained" in the polariton vacuum state can be released upon an ultrafast modulation of the light-matter coupling strength. Although it has already been shown that such a modulation is feasible in a prism-based intersubband polariton sample [Günter09], the photonic crystal membrane sample geometry turns out to be more promising for a set of technical reasons concerning the ultrafast pulse manipulation. The Chapter closes with an estimate of the detectivity required for a read-out of the vacuum photon signal.

## 4.1 Polariton bleaching and bistability

In the world of exciton-polaritons, the pheomenon named *polariton bleaching* is known since several years. A few years after the observation of these quasiparticles [Weisbuch92], it turned out that a photoluminescence experiment carried out at large excitation intensity leads to a collapse of the two polaritonic peaks into a single peak – that is, the signature of the bare cavity resonance [Houdré95]. Meanwhile, the time-domain counterpart of this phenomenology was also reported [Norris95].

In the following, we will show that the collapse of polaritonic peaks can be observed also in the intersubband framework, although the saturation mechanism is different from that involved in the exciton case. Indeed, in the excitonic case the bleaching is driven by a screening mechanism due to a dense background electron-hole plasma. In our case, instead, we interpreted the phenomenon in terms of the saturation of the intersubband transition itself: in substance, the population of the second electronic sublevel becomes similar to that of the first sublevel.

### 4.1.1 Bleaching of delocalized polariton states

A first set of measurements has been carried out on the doped sample already analyzed in Sect. 3.1.3, where the photon state is the delocalized quasi-guided mode of a photonic crystal slab (see Figs. 3.1 and 3.7). The idea is to replace the weak, incoherent, continuous wave excitation provided by the FTIR white lamp with ultrafast mid-infrared pulses provided by the set-up schetched in Fig. 4.1. Starting point is a commercial Ti:sapphire amplified pulsed laser, which provides $\simeq$ 100 fs pulses with a repetition rate of 5 kHz and average power $\simeq$ 1 W. These pulses are fed into an optical frequency amplifier (TOPAS), which generates two infrared beams whose wavelengths lie in the 1.5 μm range. The precise control of the wavelengths is provided by a software that controls both the TOPAS and the subsequent device, that is a difference frequency generator (NDFG). At its output a train of mid-infrared pulses, with a central wavelength tunable in the range from 2 to 20 μm, with the same repetition rate of the Ti:sapphire pump laser, and with an average power of about 1 mW, are available for the experiment. The central wavelength of the output pulses (whose spectral width is of the order of 100 $cm^{-1}$) is tuned in order to cover both polaritonic peaks at anticrossing.

The beam is then focused by means of a parabolic mirror (PM1 in the figure), and collected by a second mirror (PM2) which collimates the beam into the spectrometer. The focal lengths have been chosen in order to have a beam waist of about 500 μm, and a collimated beam entering the spectrometer with $\simeq$ 1 cm diameter. In this experiment, the spectrometer essentially acts as an autocorrelator for the laser pulses: the Michelson interferometer splits the beam into two delayed replicas which are then overlapped and eventually detected through the internal MCT (mercury-cadmium-telluride) detector. If the intensity at the spectrometer input is sufficiently small, the detector operates in the linear regime and the first order autocorrelation is measured.

Since the spectrometer usually operates with continuous wave light, a special setting had to be implemented in order to detect the pulsed signal we are dealing with. In essence, the signal at the detector must be demodulated by a lock-in amplifier synchronized with the laser pulse trigger, and re-injected into the spectrometer as a slowly-varying signal that constitutes the interferogram (*slow scan*). This involves certain subtleties on the time scales, and requires an optimization of the measurement parameters in order to get a reasonable signal-to-noise ratio. It turned out that the best strategy is to set the lock-in integration

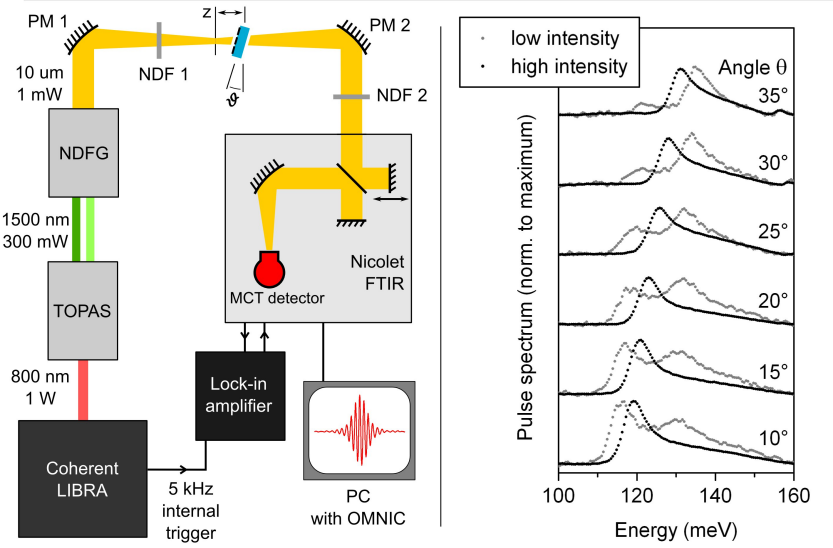


Figure 4.1: *Left panel,* schematic of the experimental setup for ultrafast excitation of polaritonic samples. The near-infrared beam from a Ti:Sapphire amplified laser (Coherent Libra, pulse duration $\simeq$ 100 fs, rep. rate 5 kHz, average power $\simeq$ 1W) are frequency-converted by an optical parametric amplifier (TOPAS) into two near-infrared beams. These beams eventually undergo difference frequency conversion (NDFG) into a mid-infrared beam, which is focused and collected by parabolic mirrors (PM 1, 2). The sample is positioned at a distance $z$ from the beam waist in order to tune the incident intensity; further control on the intensity is achieved by means of neutral density filters (NDF 1, 2). The light pulse eventually enters a Fourier-transform spectrometer (FTIR), which performs the pulse autocorrelation. *Right panel,* bleached and unbleached output pulse spectra revealing that the polaritonic anticrossing collapses when the sample is excited by a high intensity pulse.

time[1] to the smallest allowed value (1 ms) and the interferometer mirror velocity to either $\simeq$ 0.06 or 0.04 cm/s. Faster velocities would lead to a distortion of the interferogram, because the interference fringes are crossed in a time too small compared with the lock-in integration time. Slower velocities would in principle work better, but it turned out that mechanical noise often damaged the acquisition; in addition, the laser power fluctuations and/or beam position instabilities led to noisy interferogram baselines. In the case the signal was too small,

[1] A *Princeton Applied Research* 5210 lock-in was employed.

several interferograms collected in sequence were averaged.

In addition to these concerns, a control of the beam intensity is required. This applies for both the beam incident on the sample, and for the beam entering the spectrometer: the first influences the sample state (bleached/unbleached), while the second should not saturate the detector. For this purpose, we employed a set of neutral density filters (NDF1 and 2), and defocused the sample. In detail, NDF1 is a combination of mid-infrared filters manufactured by *Andover*, while NDF2 is a hole screen. The $z$-sweep was limited to $\simeq 10$ mm, to be compared with the PM1 focal length of 10 cm. Employing the nominal values of the optical density of NDF1, we figured out that the incident beam peak pulse intensity was varied in the range $0.05 \div 50$ MW/cm$^2$. This estimate relies on the average beam power measured by a power-meter and on the pulse time duration deduced by the autocorrelation trace, which shows a FWHM of $\simeq 100$ fs.

A set of angle-resolved spectra measured at low and high intensity ($I \simeq 0.05, 50$ MW/cm$^2$) are reported in the right panel of Fig. 4.1. While at low intensity the polariton anticrossing of Fig. 3.7 is retrieved, at high intensity the single spectral feature characteristic of the photonic mode (Fig. 3.7, *undoped sample*) appears. The transition between unbleached and bleached state is analyzed in detail in Fig. 4.2, revealing the collapse of the polariton doublet in a single spectral feature. In the same figure we report some of the corresponding interferograms, which reveal the time-domain counterpart of the polariton beating. Namely, the interferogram taken at $I_1$ shows an amplitude revival occurring at a time delay $\simeq 200$ fs.

The time dynamics of the bleaching process has been explored in more details by performing a short-time Fourier transform on the interferograms, as opposed to the ordinary Fourier transform applied while retrieving the spectra plotted in the previous figures. The interferogram $\mathcal{I}(\delta)$, where $\delta$ is the optical path difference between the interferometer arms, is convoluted with the Gaussian (Gabor) wavelet

$$\exp\left[2\pi i\delta/\lambda\right] \cdot \exp\left[-(\delta - \delta_0 - ct)^2/2\Delta^2\right].$$

As the wavelength $\lambda$ and the time delay $t$ are swept ($\delta_0$ denotes the zero path difference), the full time-wavelength information contained in the signal are extracted [Stade05]. The wavelet FWHM $\simeq 2\Delta$ has been set to 15 wavelengths at the central energy of 125 meV; this value corresponds to a temporal span of about 500 fs. A selection of short-time Fourier transforms is presented in Fig. 4.3 as contour plots, where

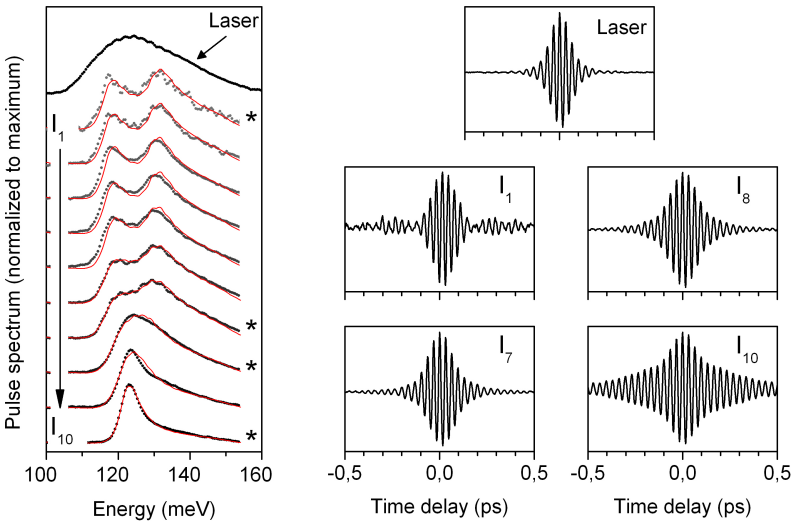


Figure 4.2: *Left panel,* polariton bleaching upon an increase of the input pulse intensity ($I_1$, low intensity, $I_{10}$, high intensity). The experimental traces (dots) have been fitted by rigorous coupled wave analysis (red traces). The laser spectrum is such that both polariton peaks are covered by the excitation. *Right panels,* interferograms (i.e. pulse autocorrelation) corresponding to the laser spectrum and to a selection of transmitted spectra (identified by a star in the left panel).

wavelengths are converted to photon energies. Under the conditions of smallest or largest incident intensity, $I_1$ and $I_{10}$ respectively, the sample is either fully unbleached or fully bleached, and no significant temporal evolution in the spectra is noticed (apart from the third peak appearing at 140 meV for $I_1$, which may originate from measurement noise). On the contrary, when the photon flux lies in the transition region ($I_7$ and $I_8$), a temporal evolution of the spectral features is observed. The most relevant effect is found for $I_7$, where a bifurcation is observed. We interpret this behaviour as follows: the overall intensity of the incoming pulse is responsible of a partial bleaching, which is revealed by the single, broad peak of the spectrum observed for zero time delay (corresponding to the interferogram centerburst, i.e. to the overlap of the most intense sections of the outcoming pulse). Meanwhile, the double-peaked spectra observed at time delays greater than a few hundred femtoseconds indicate that the interferogram tail is charac-

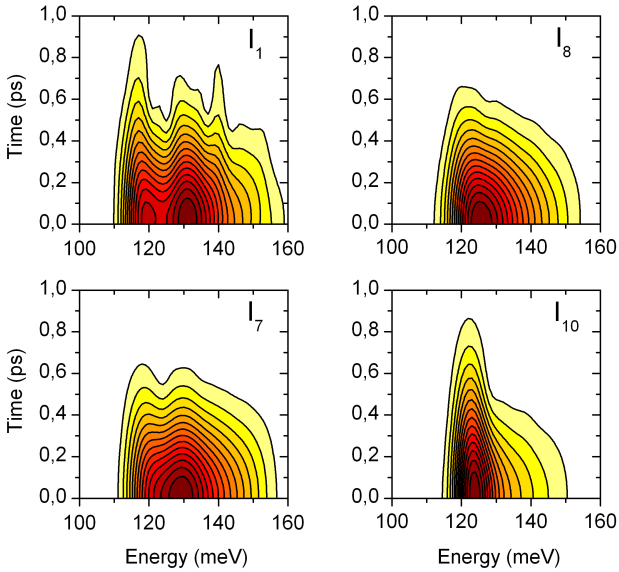


Figure 4.3: Time-resolved Fourier transform of the output pulse interferograms. The cut at zero time is substantially the ordinary spectrum reported in Fig. 4.2. Notice that for the intensity $I_7$ the single peak observed at zero time evolves in a doublet.

teristic of the unbleached state. As the interferogram tail derives from the overlap of the leading and the trailing part of the outcoming pulse, it can be inferred that at least in one of those time spans the sample is unbleached. In summary, when the incident pulse flux is in the transition region, the sample does not experience a steady bleached or unbleached state, while it passes through intermediate, non-stationary states.

From a microscopical point of view, we interpret the bleaching process as follows: the incident light is absorbed and converted into polaritons, which in turn have a "matter" part and hence imply excitation of the two-subband quantum well. As it turns out from the general theory (Eq. 1.32 and 1.39), the light-matter coupling constant depends on the surface charge *difference* between the subbands in the quantum well ($\Omega \propto \sqrt{\Delta n}$). Hence, upon strong excitation of the quantum well, $\Delta n$ may decrease and eventually reach values close to zero, implying a reduction of the polariton splitting and eventually the disappearance of strong coupling. Actually, the relation $\Omega \propto \sqrt{\Delta n}$ has been rigorously

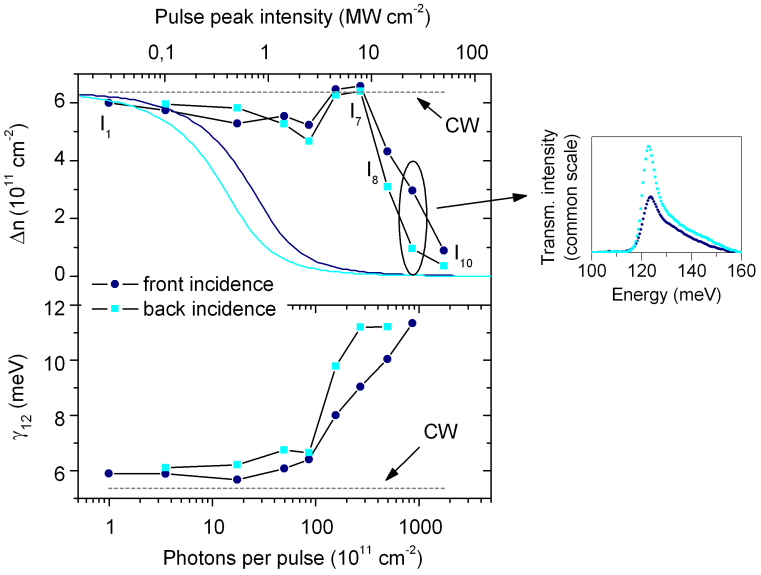


Figure 4.4: *Top panel,* dependence of the charge difference $\Delta n$ between the subband in the quantum wells upon a sweep of the incident pulse intensity. High pulse intensity means polariton bleaching and suppression of $\Delta n$ with respect to the value observed in continuous wave (CW) low intensity FTIR spectroscopy. Dots are experimental data; lines result from a rate-equation model. *Bottom panel,* dependence of the intersubband relaxation rate upon the pulse intensity. Both *front side* (gold stripe side) and *back side* (semiconductor side) excitation are considered. *Small panel,* transmittance spectrum at fixed incident pulse intensity for front and back excitation reveals a reciprocity-breaking behaviour.

proved in Chapter 1 within the steady-state hypothesis, while here we extend the concept to the ultrafast bleaching process.

The sample response as a function of $\Delta n$ has been quantified by means of rigorous coupled wave analysis (RCWA, widely employed and discussed throughout Chapter 3), in connection with the effective dielectric function (Sect. 1.4). Namely, we fitted the experimental spectra reported in Fig. 4.2, obtaining the red traces. We employed as fitting parameters the surface charge difference $\Delta n$ and the intersubband relaxation rate $\gamma_{12}$, while the other sample parameters were

already known[2] (see Sect. 3.1.3). The need to introduce $\gamma_{12}$ as a free parameter is justified according to the observations by [Kaindl01], who pointed out that upon a high excitation density the Coulomb electron-electron scattering rate within the quantum well is enhanced. As it clearly turns out from the data in Fig. 4.4, the surface charge difference starts decreasing in correspondence to the polariton collapse observed in Fig. 4.2; meanwhile, an increase in the scattering rate occurs. Notice that for low pulse intensities both $\Delta n$ and $\gamma_{12}$ are very close to the values observed in low-intensity continuous-wave spectroscopy (*CW* in Fig. 4.4; see also Sect. 3.1.3).

In order to give a definition of a *bleaching threshold*, from the evolution of $\Delta n$ and from the intensity dependent spectra it can be asserted that the bleaching occurs in the range $I = 5 \div 50$ MW/cm$^2$, where $\Delta n$ diminishes and the polariton peaks collapse[3]. However, in that range the evolution of $\Delta n$ is not smooth: this may be considered as an artifact stemming from the fact that we attempted to interpret the non-stationary bleaching process with a stationary theory. This vision is confirmed by recalling that a significant time evolution of the output pulse spectrum was occurring for intensities close to the bleaching threshold – see Fig. 4.3 and the related discussion. Nevertheless, it is clear that below 1 MW/cm$^2$ the sample is safely unbleached, while the contrary occurs for $I > 40$ MW/cm$^2$.

We now briefly discuss the role of symmetry in the non-linear dynamics of the intersubband-polariton sample. Owing to reciprocity[4], the transmittance spectra measured upon illumination of either the front or the back side of the membrane should be the same, despite the sample intrinsic asymmetry. While performing the ultrafast excitation experiment, it instead turns out that the transmittance depends on the excitation side (see the smaller panel in Fig. 4.4): at fixed beam intensity, when the sample is excited from the semiconductor side (*"back incidence"*) the absolute transmittance is larger with respect to what is observed by exciting the metal strip side. In terms of bleaching threshold, it means that the sample is more easily bleached upon back-side

[2]Actually, we also needed to introduce in the fit an overall scaling factor, since the measured transmission spectra were not available in absolute units.

[3]This value can be compared with the data reported in the literaure about the intersubband transition saturation of a MQW not embedded in a resonant cavity [Julien88, Duboz95]. The results of the second paper are in agreement with our observations, although it is not straightforward to compare results obtained with and without a resonant cavity, and – more in general – results in weak coupling with those in strong coupling.

[4]See footnote 7 in Chapter 2.

excitation. This non-reciprocal behaviour is typical of an intensity-dependent process, here provided by the two-level system saturation. It can indeed be proved by RCWA simulations that the intracavity field intensity, and hence the number of photoexcited carriers, is larger upon back-side excitation with respect to front-side excitation: this is the mechanism that provides an asymmetric response. In conclusion, an intersubband polariton device could constitute a promising platform for designing saturable absorbers and optical isolators working in the mid-infrared spectral range.

### 4.1.2 Rate-equation model of polariton saturation

As hinted at the end of the previous Section, an intersubband polariton sample shows features reminiscent of a saturable absorber and of an optical isolator. In order to design an effective device, and more in general in order to better understand the bleaching phenomenon, we developed a simple rate equation model capable of predicting the saturation of $\Delta n$ and the consequent operation of the intersubband polariton sample as a saturable filter, optical isolator or even as a bistable device.

The model works in the semiclassical approximation, hence it relies on the sample absorbance $A(\omega)$ calculated by means of RCWA with the QWs treated as an effective medium (Sect. 1.4), or by the coupled-mode theory (CMT, Chapter 2). Let's consider a sample surface $S$ excited by a beam of intensity $I$: the number of photons absorbed per unit time by the sample is given by $N_{abs} = A(\omega)IS/\hbar\omega$, where $\hbar\omega$ is the photon energy. Now, let us assume that each absorbed photon promotes an electron from the first to the second QW subband, and that the electrons in the second subband can undergo non-radiative decay into the first subband at a rate $\gamma_{12} = 1/\tau_{12}$. With these assumptions, the following rate equation is obtained:

$$\frac{dN_2}{dt} = -\frac{N_2}{\tau_{12}} + \frac{A(\omega)IS}{\hbar\omega}.$$

Imposing the stationary condition, and normalizing to the surface, the following equation holds:

$$\frac{n_2}{\tau_{12}}\frac{\hbar\omega}{I} = A(\Delta n, \omega). \tag{4.1}$$

Here, it is evidenced that the absorbance depends on the surface charge difference $\Delta n = n_1 - n_2$. In the case the absorbance is calculated by

RCWA, the dependence on $\Delta n$ occurs via the effective permittivity of the MQW, Eq. 1.44. In the case the absorbance is calculated by the CMT, the dependence on $\Delta n$ occurs via Eq. 2.13. Since the total number of electrons is given by the stationary doping $n^{(0)}$, the additional constraint $n^{(0)} = n_1 + n_2$ holds, and the above equation is a self-consistent formula that can be solved for the relation $\Delta n \leftrightarrow I$.

Equation (4.1) rigorously holds for a monochromatic and stationary excitation, hence in principle it is not properly applicable to the ultrafast bleaching process. Instead, it could be applied to a situation where the excitation is quasistatic, as for example mid-infrared pulses from a Q-switched laser or from a pulse generation system based on properly tuned non-linear crystals. Nevertheless, we naively try to reproduce the saturation transition observed in the previous Section with Eq. 4.1. The idea is to treat the broadband, ultrafast pulse as incoherent, and to replace the monochromatic absorption $A(\Delta n, \omega)$ which appears in Eq. 4.1 with an average absorption $\bar{A}(\Delta n) = (\int_{\Delta\omega} A(\Delta n, \omega) d\omega)/\Delta\omega$ where the averaging window is given by the laser pulse spectral width. In substance, the whole, double-peaked polaritonic absorbance has to be averaged out. The result of the self-consistent calculation is given in Fig. 4.4, upper panel, as a continuous line[5]. Apart for an underestimate of the bleaching threshold by about one and a half orders of magnitude, the slope of the saturation curve and the difference between front and back incidence are correctly reproduced. The mismatch of the absolute value of the bleaching threshold could be attributed either to the oversimplifying hypotheses assumed in the model, but also to a possible calibration imperfection of the experimental power impinging on the sample.

Further confidence in the model prediction will be gained by analyzing the bleaching process occurring in defect-mode polaritonic samples, which is the topic of the next Section.

### 4.1.3 Bleaching of defect-mode polariton states

Being the polariton bleaching driven by the saturation of the intersubband transition, which is a nonlinear phenomenon, at first glance it may appear that the bleaching threshold can be reduced by employing a cavity where the internal field at resonance is enhanced. Upon

[5]Here, the intersubband scattering rate $\gamma_{12}$ entering the effective permittivity, and hence the absorption calculation by RCWA, has been kept fixed to the static value, $\hbar\gamma_{12} \simeq 6$ meV. Accordingly, in Eq. 4.1 we employed $\tau_{12} = 1/\gamma_{12} \simeq 100$ fs.

broadband excitation, i.e. when a light pulse which covers both upper and lower polariton peaks is employed, this picture turns out to be wrong. Instead, samples with different field enhancement factors show the same behaviour, within the experimental error.

In Fig. 4.5 we report the result of the bleaching experiment performed on the three defect-mode samples whose linear response characterization has been described in Sect. 3.1.4. We just recall that the samples differ by the number of Bragg mirror periods $N$, a parameter that tunes the cavity mode radiative decay rate. The bleaching experiment follows the same lines already described in Sect. 4.1.1, with the sole difference that the fine tuning of the incident power has not been obtained by defocusing the sample, rather, we employed a home-made step filter fabricated by successive evaporation of Titanium over a double-side polished GaAs undoped wafer. Despite its calibrated optical density, it was not possible to figure out the absolute beam intensity incident on the sample, since the nonlinear generation stages of the source were not properly aligned and the output intensity from the laser system was out of the sensitivity range of the power meter.

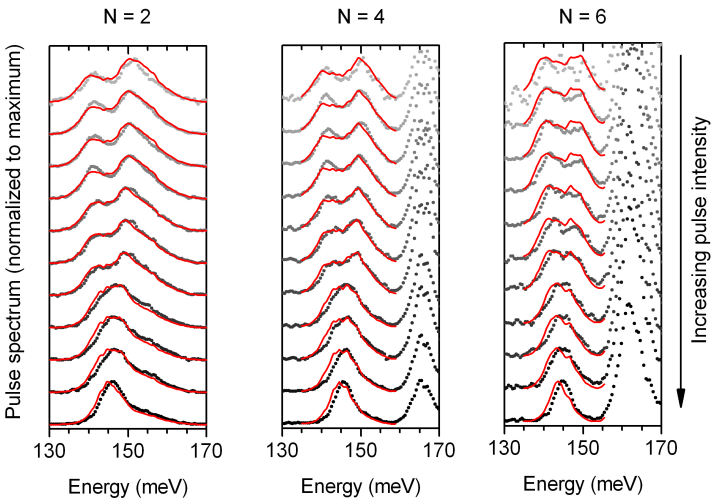


Figure 4.5: Bleaching of defect-mode polariton states, observed in samples which differ by the number of Bragg mirror periods $N$. The spectra at the top (bottom) correspond to low (high) intensity excitation.

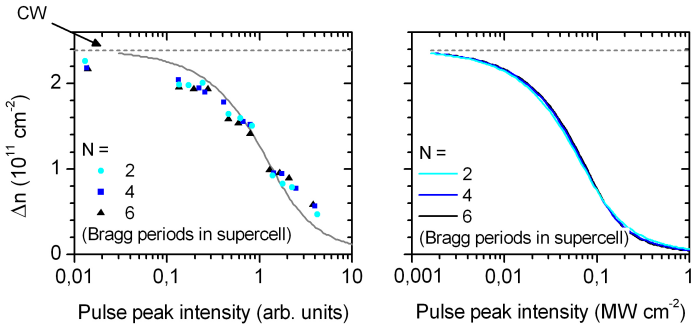


Figure 4.6: Dependence of the charge difference between the quantum well subbands on the incident pulse intensity. *Left panel*, experimental data, *right panel*, theoretical prediction. The theoretical curves obtained for different $N$'s are quasi-overlapped. One of them is reported in the left panel for comparison with the experimental data, however, it is not linked to absolute values of the pulse intensity (see text). The horizontal line labeled *CW* refers to the value obtained from continuous wave FTIR spectroscopy.

The spectra reported in Fig. 4.5 are ordered from the top to the bottom according to increasing incident power, but no absolute values can be given. The polariton bleaching clearly appears as the usual collapse of the polariton doublet; as for the data collected on the sample without defect (Fig. 4.2), the spectra were fitted by means of rigorous coupled wave analysis (red traces)[6].

The quantitative evolution of the surface charge difference upon the incident intensity is reported in Fig. 4.6, left panel. As anticipated, there is no significant difference between the data obtained in correspondence to a different number of Bragg mirror periods, which is the parameter that governs the intracavity field enhancement at resonance (see Fig. 3.5). An element supporting this vision is the result of the rate equation model outlined in the previous Section. Indeed, in the right panel of Fig. 4.6 we report the curves obtained by solving Eq. 4.1 with the spectrally-averaged absorption provided by RCWA: the data corresponding to different $N$ are mainly indistinguishable. Now, it would be interesting to quantitatively compare the experimental points with

[6] As opposed to the previous case, here we neglected the $\gamma_{12}$ dependence on the incident power.

the theoretical curves; however, as anticipated above, in the experiment we only know the incident power *modulus* a multiplying factor. Hence, in the left panel we tried to overlap to the experimental data a theoretical curve, without a quantitative link to the horizontal axis, and it clearly turns out that the experimental trend is well reproduced. For this reason, although we know that the experimental conditions are far more complex, we think that the rate equation model could be an element of support in designing further experiments.

### 4.1.4 Intersubband polariton bistability and sharp saturation

From the results given in the previous Section it appears that the strong field enhancement inherent to defect mode resonances does not lead to a saturation dynamics different from that observed in the delocalized mode sample. In the following we will show that this equality is lost when *broadband excitation* is no longer considered, i.e. when the incident light spectrum does not cover any more both polaritonic peaks. In this case, which we will refer to as *narrowband excitation*, the field enhancement actually plays a role. Better yet, the fundamental role is played by the *cooperativity increase* induced by a large cavity quality factor.

In order to better understand the polariton bleaching, it is worth having a look at the graphical solution of Eq. 4.1, both for broadband and for narrowband excitation. In Fig. 4.7, upper panels, we report the graphical solution that led to the saturation curve given in Fig. 4.6, i.e. broadband excitation of the defect-mode samples. The curves in Fig. 4.7 represent the left- and right-hand side members of Eq. 4.1. The RHS is here the average absorption $\bar{A}(\Delta n) = (\int_{\Delta\omega} A(\Delta n, \omega) d\omega)/\Delta\omega$, resulting from a RCWA calculation. The LHS, i.e. $n_2 \hbar\omega/\tau_{12} I$, is represented by the lines that converge on the $\Delta n$ axis at the point $n^{(0)}$; this is because of the relation $n_2 = (n^{(0)} - \Delta n)/2$. By increasing the beam intensity $I$ (the three lines correspond to $I = 0.01, 0.1, 1$ MW/cm$^2$), the slope decreases, and the self-consistent $\Delta n$ becomes smaller accordingly. The resulting $\Delta n(I)$ is exactly the saturation curve reported in Fig. 4.6; its smooth trend has hence to be ascribed to the smooth, monotonic function $\bar{A}(\Delta n)$.

A different situation is found if monochromatic excitation is supposed to be employed. In the lower panels of Fig. 4.7 we replace the averaged absorbance by its monochromatic value calculated at reso-

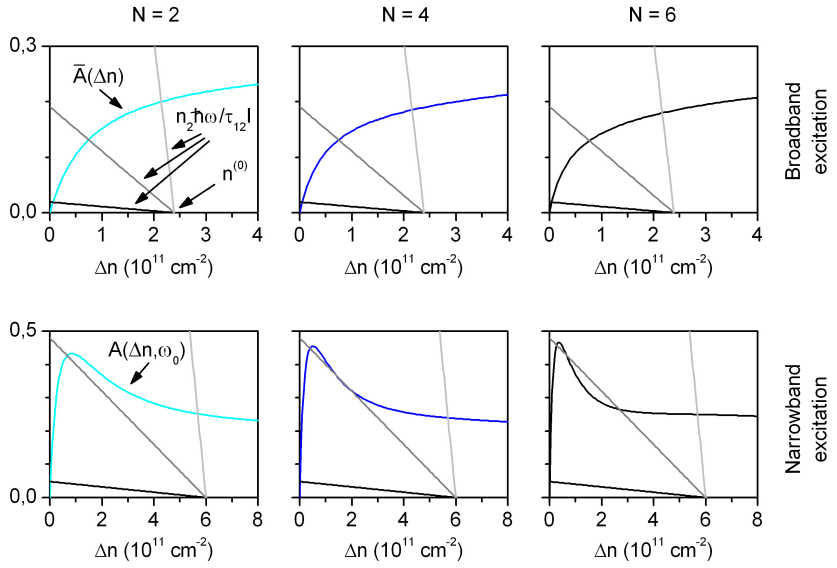


Figure 4.7: Graphical solution of Eq. 4.1 for the broadband case *(upper panels)* and the narrowband case *(lower panels)*. The calculations refer to different defect-mode samples, where the number of Bragg periods $N$ induces a tuning of the radiative decay rate. Other details are given in the main text.

nance, i.e. $A(\Delta n, \omega_0)$. The resulting curves are no more monotonic, rather, they exhibit a maximum whose width and position depends on the sample. In particular, in the samples with $N = 4$ and 6 Bragg periods the decrease of $A(\Delta n, \omega_0)$ after its maximum value is sufficiently faster that multiple solutions of the graphical equation can be attained, i.e. bistability[7]. This behaviour, here obtained by means of a numerical approach (the RCWA), is actually a general feature that finds its roots in the coupled mode theory of light-matter coupled resonators (Chapter 2).

Recalling Eqs. 2.7 and 2.23, it turns out that for zero detuning and zero non-resonant losses the absorbance of a symmetric two-port system reads

$$A = \frac{2\gamma_r\gamma_{12}\Omega^2}{(\gamma_r\gamma_{12} + \Omega^2)^2}$$

[7]For this purpose, we needed to assume a static charge density $n^{(0)} = 6 \cdot 10^{11}\ \mathrm{cm}^{-2}$, larger than the value $n^{(0)} \simeq 2.5 \cdot 10^{11}\ \mathrm{cm}^{-2}$ which characterizes the the sample employed for broadband bleaching.

where $\Omega$ is the coupling constant, whose square is proportional to the surface charge difference ($\Omega^2 \propto \Delta n$), and $\gamma_r, \gamma_{12}$ are the radiative decay rate of the cavity and the intersubband relaxation rate, respectively. This absorbance, considered as a function of $\Omega^2$, has a maximum at $\Omega^2 = \gamma_r\gamma_{12}$, where $A = 1/2$; actually, this is not a surprise, since it is nothing else than the weak critical coupling condition (Eq. 2.17). Hence, the trend observed in the absorbances of Fig. 4.7, bottom panel, as $N$ is increased, is consistent with the above picture. Recalling that larger $N$ means smaller $\gamma_r$, the absorbance peak occurs at smaller $\Omega^2$, hence at smaller $\Delta n$. In substance, bistability is favoured by a large mismatch between the $\Delta n$ value corresponding to the peak absorbance and the static charge density $n^{(0)}$; in terms of the coupled-mode theory, this means a large cooperativity $\Omega_0^2/\gamma_r\gamma_{12}$ (where $\Omega_0 \propto \sqrt{n^{(0)}}$ is the coupling constant of the unbleached sample).

The influence of a large cooperativity attained in large-$N$ defect mode samples on the actual saturation curves can be seen in Fig. 4.8. As opposed to what observed for broadband excitation (Fig. 4.6), here the saturation transition is sharper, and bistability develops when $N \geq 4$. The case $N = 6$ corresponds to a larger bistability cycle width, of about 20 %, but larger cycles could be achieved by a further sample optimization.

Polariton bistability in the excitonic framework has ben predicted about two decades ago [Tredicucci96], and observed in different declinations (see, e.g, [Baas04, Bajoni08]); however, intersubband polariton bistability has never been considered so far. While there is not an immediate application for the bistability phenomenon itself, the sharp saturation may find an application in mid-infrared saturable filters. One of the strength points is that the operation as saturable filter does not rely on the sole absorption: while it is clear from Fig. 4.8 (lower panels) that the transmittance is modulated from 0 to 1, Fig. 4.7 (lower panels) reveals that no more than 50 % of the incident radiation is absorbed. Indeed, recalling the above discussion about the coupled-mode theory, it can be stated that the operating principle of such a filter is the weak critical coupling condition in a polaritonic system, stressing once again the relevance of the critical coupling concept.

### 4.1.5 Bleaching *vs* polariton lasing thresholds

The bleaching experiments allowed to determine the threshold intensity of resonant excitation above which the polariton states are de-

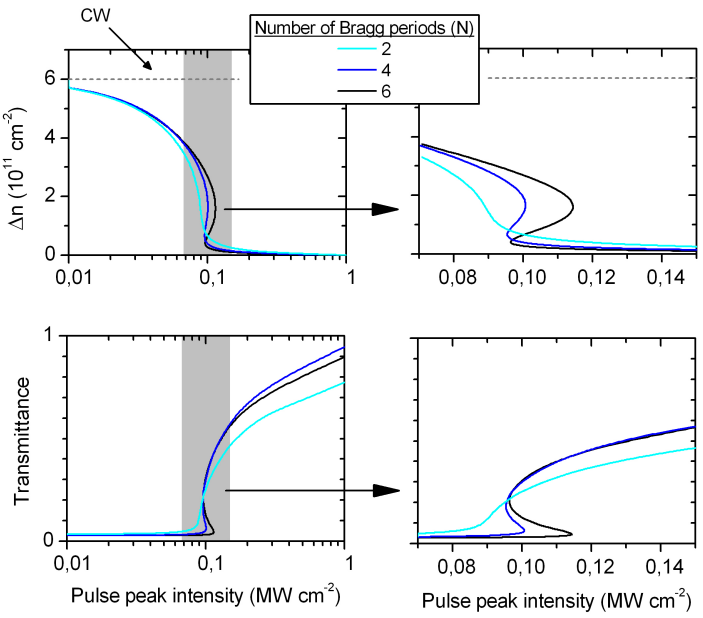


Figure 4.8: Sharp saturation and polariton bistability occurring in defect-mode polariton samples upon quasi-monochromatic excitation. Both surface charge difference *(top panels)* and transmittance *(lower panels)* exhibit a sudden transition, actually featuring a bistable behaviour in the cases $N = 4, 6$.

stroyed. It is interesting to compare this value with the typical intensities that are likely to induce polariton lasing [De Liberato09c]. In this work, the threshold pump intensity $I^{thr}_{pump} = 3.5 \cdot 10^4$ W/cm$^2$ was determined. A first comparison can be made with the measured bleaching threshold (see Fig. 4.6 and related discussion), i.e. $10^7$ MW/cm$^2$. The latter appears to be three orders of magnitude larger, hence polariton bleaching would not be an obstacle in view of the development of a polariton laser.

However, this estimate is subject to certain inconsistencies. First, the threshold pump intensity reported in the work cited above appears to be overestimated. Recalling the expression given there,

$$I^{thr}_{pump} = \frac{1}{A(\omega_{\mathrm{UP}})|z_{\mathrm{LP}}|^2|z_{\mathrm{UP}}|^2 Q_{phon} F_\sigma} \frac{\gamma_{\mathrm{UP}}\gamma_{\mathrm{LP}}\hbar^2\omega_{\mathrm{UP}}\varepsilon_0\varepsilon_r}{4e^2 L_{\mathrm{QW}}}$$

we obtain a threshold pump intensity of $3.75 \cdot 10^2$ W/cm$^2$. Here, we slightly modified the notation in order to be consistent with the present thesis work: $A(\omega_{\mathrm{UP}})$ is the absorption coefficient at the upper polariton frequency, $z$ are the electronic components of the polaritonic state, $Q_{phon}$ is the phonon resonance quality factor, $F_\sigma$ is an overlap factor stemming from phonon-electron wavefunction overlap, $\gamma$ are the polariton linewidths, and $L_{\mathrm{QW}}$ is the quantum well thickness. The parameters we employed are exactly the same considered in the original paper, and, by the way, they are very close to the experimental reality[8].

The second inconsistency stems from the mismatch between the measured bleaching threshold, and that calculated with the rate equation model. Despite the oversimplifying model, the good agreement between the experimental and the theoretical trends observed in Fig. 4.6, and – to a lesser extent – in Fig. 4.4, induces to think that the experimentally determined absolute incident powers could be affected by an error of about one order of magnitude. Under this hypothesis, and trusting the rate equation model, the bleaching occurs in the incident power range of about $10^4 \div 10^5$ W/cm$^2$ for the defect samples, and $10^5 \div 10^6$ W/cm$^2$ for the ordinary photonic crystal sample[9]. These values, compared with the corrected estimate of polariton lasing threshold, are still safely above by two orders of magnitude.

In conclusion, it appears that polariton lasing is not precluded by polariton saturation. However, it should be recalled that the bleaching thresholds we observed correspond to broadband excitation, while polariton scattering processes – at least in the excitonic framework – work better under narrowband excitation. In substance, a more complete and reliable insight into both polariton saturation and into stimulated scattering and lasing phenomena would rely on a new experiment, where the pump beam could be tuned in frequency, intensity, and incident angle on the sample surface. Meanwhile, the output radiation from the sample should be analyzed in an angluarly-resolved fashion. These issues cannot be solved immediately, since the flexibility of ultrafast mid-infrared systems is not as wide as that of near-infrared or visible instruments. For instance, the output pulse from the NDFG has a fixed bandwidth, related to the pulse time duration, and cannot be varied witout acting into the calibrated commercial system. Meanwhile, the detection of the emitted radiation at variable angles is

[8] In detail, $\gamma_{\mathrm{UP}} = \gamma_{\mathrm{UP}} = 5 \cdot 10^{12}$ s$^{-1}$, $\hbar\omega_{\mathrm{UP}} = 120$ meV, $A(\omega_{\mathrm{UP}}) = 0.4$, $|z_{\mathrm{LP}}|^2 = |z_{\mathrm{UP}}|^2 = 1/2$, $Q_{phon} = 100$, $F_\sigma = 0.1$, $L_{\mathrm{QW}} = 10$ nm.

[9] This difference has to be ascribed to the different doping $n^{(0)}$.

not directly feasible, in that an ordinary FTIR spectrometer cannot be mounted on a rotational stage. Hence, an ad-hoc experimental setup needs to be developed in order to explore the intriguing dynamics of intersubband polaritons upon intense optical excitation.

## 4.2 Polariton switch-on and vacuum photon emission

While the topic of the previous Section was the *destruction* of polaritons on an ultrafast time scale, here we are going to deal with polariton *creation* occurring on a sub-picosecond characteristic period. While it started about ten years ago, following a set of theoretical works [Ciuti05, De Liberato07, De Liberato09a], the search for vacuum photon emission from the polariton ground state revealed significant technical difficulties. First of all, the need of a mechanism which is able to induce a modulation of the coupling constant, i.e. of the Rabi frequency, on a time scale comparable with the inverse of the Rabi frequency itself. A first idea to modulate the light-matter coupling relied on an electrical gating technique [Anappara05, Anappara06], but the limitations due to the frequency cutoffs characteristic of capacitive elements intrinsic in the device turned out to be a major challenge to overcome. Afterwards, the possibility to *optically dope* the quantum well has been considered. The basic idea is to fabricate a polaritonic sample with an undoped heterostructure, where the polaritonic coupling is intrinsically absent, and to promote the electrons from the semiconductor valence band to the conduction band by means of an ultrashort near-infrared laser pulse. The electrons have to be promoted only into the first electronic subband of the quantum well, in order to have a finite $\Delta n$.

This key experiment has been carried out at the University of Konstanz, in the group of A. Leitenstorfer and R. Huber [Günter09]. By employing a custom-made ultrafast laser system, capable of delivering 12 fs near-infrared pump pulses, with in parallel a mid-infrared probe pulse generation and detection line, it was possible to observe the polariton switch-on dynamics occuring on a time scale of $\simeq 100$ fs. This would already have led to the emission of vacuum photons, but a detection scheme has to be designed and carefully optimized in order to match the detectivity requirements. However, before embarking into such task a new sample geometry had to be devised. In the

experiment by Günter, the "historical" planar waveguide sample geometry was employed, with a prism-shaped sample. There, the pump and the probe beam were not collinear, with the resulting need to tilt the pump beam wavefronts, which involved delicate tuning of certain optical components. Hence it is preferrable to develop a new sample geometry where the pump and the probe beam could travel in a collinear fashion. This is the photonic crystal slab geometry, widely analyzed troughout the doctoral work.

### 4.2.1 Polariton switch-on in a photonic crystal membrane

Before attempting a vacuum photon emission experiment, we went through the ultrafast characterization of the photonic crystal samples. The results were obtained in collaboration with the group of R. Huber, now at the University of Regensburg, and are fully detailed in a publication [Porer12]. In Fig. 4.9 (a) and (b) a sample schematic is reported, together with a sketch of the light pulses involved in the experiment. The samples employed here are both of the *on-substrate* type (see Sect. 3.2), and of the *membrane* type (see Sect. 3.1); both are desiged in order to observe a polaritonic anticrossing at a finite value of the $k$-vector in the Brillouin zone. The sample is excited by a near-infrared pump pulse, followed after a time $\tau$ by the mid-infrared probe pulse.

Analyzing the on-substrate sample, in the absence of the pump pulse, the Fano resonance typical of this photonic resonator is observed [Fig. 4.9 (e)]. An angularly-resolved characterization of the sample leads to the transmittance map reported in Fig. 4.10 (a), with a clear evidence of a photonic band starting from the center of the Brillouin zone. When the pump beam is turned on, the photonic band splits into two polaritonic branches, with the anticrossing evidenced in Fig. 4.10 (b). The spectra have been measured after a time delay $\tau = 1000$ ps, since the polariton switch-on dynamics turned out to be very slow with respect to the pump pulse time scale. This behaviour has been attributed to the fact that the sample has a large metal coverage ($f \simeq 60\,\%$ in the notation of Fig. 3.13), and hence the short-wavelength pump beam only excites electrons in a small fraction of the active quantum well region. While it is true that the electrons subsequently migrate in the whole active region, which actually leads to the polariton splitting build-up, no ultrafast polariton switching was here observed. This is because the characteristic diffusion times are much longer than the ultrafast time scales ($\simeq 10$ fs) we were looking for. In addition, it was not even

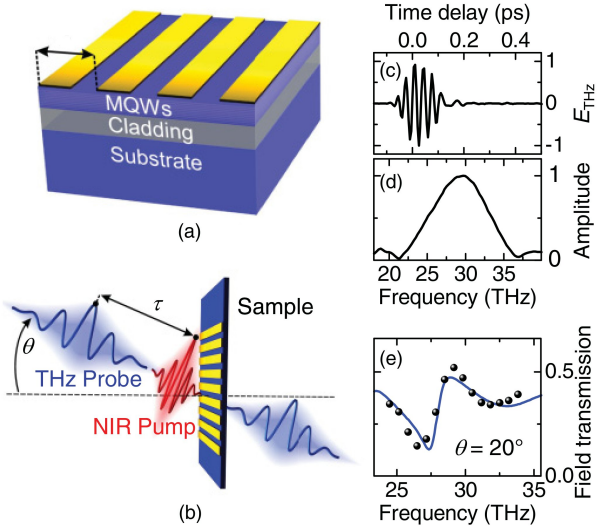


Figure 4.9: *Panels (a) and (b),* schematics of the samples and measurement operation principle. A near-infrared pump pulse is used to photoinduce a carrier density in the QWs; it is followed after a time $\tau$ by a multi-THz (mid-infrared) probe pulse. The time-resolved electric field of the probe pulse is read out by means of electro-optical sampling: a typical time-domain trace of the bare probe pulse is reported in *panel (c),* with the corresponding amplitude spectrum in *panel (d)*. In *panel (e)* we report a normalized transmitted probe pulse spectrum, which reveals the typical Fano-like photonic lineshape occurring when the pump beam is off.

possible to pump the sample from the other side, since the bulk GaAs substrate would have absorbed all the pump light.

This was one of the reasons that led us to develop the photonic crystal membrane technology, which turned out to be very promising in order to observe ultrafast polariton phenomena. The result of a time-resolved pump-and-probe experiment carried out on a membrane similar to those described in Section 3.1 is reported in Fig. 4.11. At first, we analyzed the dependence of the polaritonic splitting upon the pump beam fluence [panel (a)]. As the fluence is increased, more and more electrons are promoted from the semiconductor valence band to the first conduction subband in the quantum well, and the splitting increases. In the inset we quantify this phenomenon, by plotting the peak splitting as a function of the pump flux. Since the number of

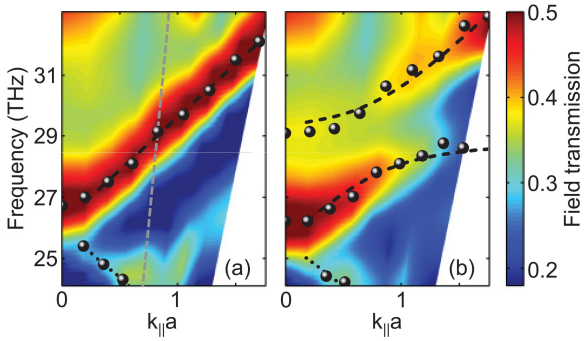


Figure 4.10: Band structure measured by means of ultrafast spectroscopy. *Panel (a),* bare photonic bands observed when the pump beam is off; *panel (b),* polaritonic splitting of the upper photonic band upon pumping (i.e. photoinduced doping of the quantum wells).

excited electrons is proportional, in first approximation, to the incident pump flux, the peak splitting is expected to grow linearly with the square root of the pump flux. This is what happens at low fluxes; when fluxes larger than 400 $\mu J/cm^2$ are employed, the splitting increases at a lower rate. This has been attributed to the saturation of the interband transition, and sets an upper limit to the Rabi splitting that can be dymanically activated.

The ultrafast polariton switch-on is reported in the right panel of Fig. 4.11, where several spectra corresponding to a fixed pump intensity and variable pump-probe delay times are considered. The main switch-on dynamics occurs on a time scale of the order of 100 fs, compatible with the original observations on the planar waveguide sample [Günter09]. This is a significant number, since the switch-on time influences the number of vacuum photons that can be emitted.

### 4.2.2 Estimate of the vacuum photon emission rate

Having demonstrated that the light-matter interaction can be non-adiabatically switched on in an intersubband polaritonic photonic crystal sample, we will now estimate the number of vacuum photons that are expected to be released from the cavity during the process. Our estimate follows the guidelines sketched in [De Liberato09a], Sect. 2.2, with specific reference to the photonic crystal geometry. In that work, a more sophisticated estimate based on a full quantum-mechanical treat-

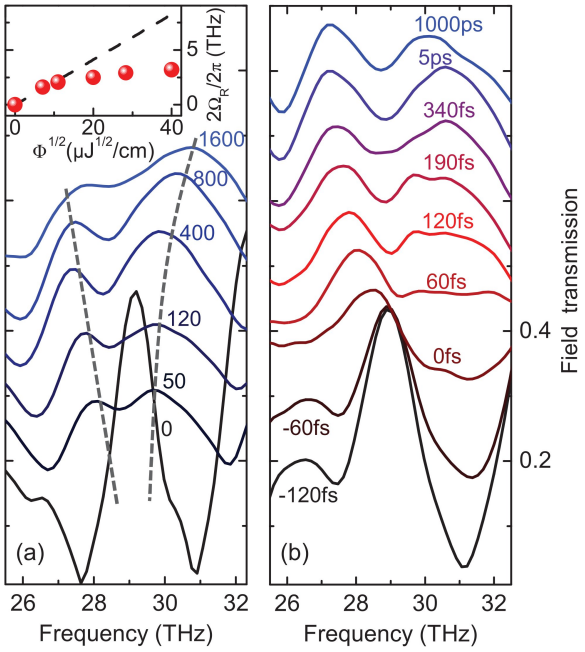


Figure 4.11: *Panel (a),* weak/strong coupling transition driven by ultrafast photoinduced doping. The single photonic peak observed at zero pump fluence ($\Phi$, stated in $\mu J/cm^{-2}$) develops in the polaritonic doublet when $\Phi$ is increased. All the measurements are taken at $\tau = 1000$ ps. In the *inset* the peak splitting $2\Omega_R/2\pi$ as a function of the pump fluence is reported. *Panel (b),* time-resolved polariton build-up. As opposed to panel (a), the fluence is kept fixed at $\Phi = 1600$ $\mu J/cm^{-2}$, while the pump-probe delay $\tau$ is swept.

ment of the dynamic process is also provided. These estimates explicitly refer to a prism-shaped cavity based on a planar waveguide, while we will make reference to the photonic crystal slab geometry. Since our results differ by two orders of magnitude, the problem seems to be still open to discussion.

The estimate relies on the idea that if the coupling is suddenly turned on, all the virtual waveguide photons "contained" in the sample are released as free propagating photons. Starting point is the number of waveguide photons per mode in the polariton vacuum, calculated according to Eq. 1.43:

$$\langle G_{\mathbf{q}} | a^{\dagger}_{\mathbf{q}} a_{\mathbf{q}} | G_{\mathbf{q}} \rangle = |y_{\mathrm{LP}}|^2 + |y_{\mathrm{UP}}|^2 \simeq 0.2 \times \left( \frac{\Omega_R}{\omega_{12}} \right)^2 ,$$

where the approximate equivalence stems from an analysis of the numerical solution of the Bogoljubov transformation (Eq. 1.40). This expression quantifies the relevance of the *ultrastrong coupling* in the phenomena connected to the vacuum photon concept.

Now it is sufficient to count the photon states which are available and relevant for the emission process. While at first glance it may appear that the only relevant photon states are those corresponding to energies close to the anticrossing, it has already been pointed out in connection to the results given in Fig. 1.5 that the vacuum photon distribution is fairly broad, and also the $q$-states far from the anticrossing significantly contribute. Hence, the main limitation is the angular acceptance of the detecting device, which sets the limits on the region of the $q$-space from which the photons can be collected. Referring to the acceptance angle as $\theta$, the number of $q$-states involved is simply $\pi k_0 \sin^2\theta/(2\pi/L)^2$, and the total number of vacuum photons is finally

$$0.2\left(\frac{\Omega_R}{\omega_{12}}\right)^2 \pi \sin^2\theta \frac{S}{\lambda_0^2},$$

where $S$ is the sample surface and $\lambda_0$ the photon wavelength in vacuum. By employing the typical values for the photonic crystal samples, i.e. $\hbar\Omega_R \simeq 7$ meV, $\hbar\omega_{12} \simeq 120$ meV, and assuming a collection angle[10] $\theta = 20^\circ$ and an active sample surface[11] $S = (100\ \mu\text{m})^2$, one gets 0.025 photons emitted per each switch-on event.

This number is two orders of magnitude below the value reported in [De Liberato09a]. It appears that this is due to two contributions. First, in that work, one of the two angular integrations has not been considered, hence lacking a factor $\sin\theta$. Second, it seems that there is an extra $\varepsilon_r$ contribution, where $\varepsilon_r \simeq 10$ is the substrate dielectric constant. The author was dealing there with an on-substrate sample, and it seems unreasonable that the presence of a high-index substrate can lead to an increase in the *overall* number of photons. Possibly, the *local* density of electromagnetic states has been employed, rather than the *far-field* photon density.

What is not possible to figure out from the present simplified model is the dependence of the number of emitted photons upon the duration of the switch-on process. In this sense, the number stated above is

[10] Notice that the estimate has been performed assuming that the sample is isotropic along the $xy$ plane. This is not true for the grating sample, but we think that no major departure from this behaviour is expected – at least for small collection angles.

[11] This is dictated by the pump spot in the Regensburg setup.

an *upper limit*, that can be achieved upon *instantaneous* switch-on of the light-matter coupling, and *complete* extraction of the virtual photons. Relying on [De Liberato09a], passing from the instantaneous switch-on to a typical time of $\simeq$ 10 fs, which is the lower limit dictated by the pump pulse in the Regensburg setup, a further loss of one order of magnitude will occur. In substance, the expected number of emitted photons per pump pulse is 0.0025, more than four orders of magnitude less with respect to the state-of-the-art sensitivity for the electro-optical detection scheme already integrated in the pump-and-probe setup. Actually, this is not all: as observed in the switch-on experiment, despite a 12 fs pump pulse, the switch-on dynamics appears to occur on a $\simeq$ 100 fs time scale. If this were the relevant number, an even stronger limit would appear, since the estimates given by De Liberato report a further loss of 2 orders of magnitude at least.

Hence, the quest for vacuum photon emission from intersubband polariton states is still hard. This is because of several constraints encountered while attempting to optimize the experiment. On the one hand, one may attempt to enlarge the active sample surface, but this means employing a more powerful pump laser and leads to possible sample damage. On the other hand, one may look for larger $\Omega_R/\omega_{12}$, a situation that can be attained in THz intersubband polaritons. However, it is tougher to detect THz photons rather than mid-infrared photons; what is even worse, is that the sample geometry is not favorable at all. Indeed, as outlined in Sect. 4.2.1, the pump beam cannot be shined on the metal pattern side of the sample, while the present technology for THz resonators implies a double-metal structure [Todorov09, Todorov10a], thus making the experiment unfeasible unless a new generation of THz resonators is developed.

# Conclusions and perspectives

This thesis work is centered around the development of a new class of photonic resonators which constitute the basis for samples where the intersubband polariton quasiparticles can be observed. Intersubband polaritons stem from the strong light-matter coupling of a photonic resonator embedding an heterostructure supporting intersubband transitions, and show potential for light-emitting devices operating either in the mid-infrared or in the terahertz spectral range, based on polariton-polariton stimulated scattering processes. In addition, the possibility of reaching the ultra-strong coupling regime is the basis for the observation of vacuum photon emission from the polariton ground state.

Intersubband polaritons are quasiparticles originating from the quantum treatment of the light-matter coupling at mid-infrared or terahertz frequencies in a semiconductor (multi-) quantum well heterostructure, spatially overlapped with the resonant electromagnetic field of a microresonator. The general description of the problem was given in **Chapter 1**, where the focus is on a formula showing how the field inhomogeneity across the multi-quamtum well influences the light-matter coupling strength, i.e. the vacuum Rabi frequency. The approach is based on the complete Hamiltonian, including the anti-resonant terms (responsible for the ultra-strong coupling regime) and the electron-electron interaction.

While the Hamiltonian theory gives fundamental insights into the quantum nature of the quasiparticles, it does not answer the question on how effectively the external fields couple to the polaritons. This problem has been approached in a semiclassical way, introcuding a set of coupled-mode equations (**Chapter 2**) which depend on a limited set

of parameters; namely, the light-matter coupling $\Omega$, the cavity radiative and non-radiative damping rates $\gamma_r$ and $\gamma_{nr}$, and the transition damping rate $\gamma_{12}$. The model, which has a much more general application span than the sole intersubband polariton framework, predicts a peculiar situation which we named *strong critical coupling* (SCC). When the system is under SCC, the absorption spectrum is double-peaked – which we interpret as a signature of *strong coupling* – and the peaks reach unity values. In other words, all the incoming photons are converted into the quasiparticles. This occurs under the generalized *critical coupling* condition $\gamma_r = \gamma_{nr} + \gamma_{12}$, from where the introduced nomenclature is drawn.

Moreover, if the system under consideration can exchange energy with the exterior by means of two scattering ports (like a suspended membrane photonic crystal, see below), a further degree of freedom in controlling the system is gained. Actually, when the system is excited from both ports, a simple sweep of the relative phase difference of the input beams allows to tune the absorption from unity to zero. This phenomenon, already known as *coherent perfect absorption* (CPA) when a broadband weak absorber is embedded in a Fabry-Pérot cavity, is here theoretically predicted and experimentally observed for the first time in a strongly coupled system, hence leading to the terminology *polariton CPA*.

Perfect coherent energy transfer into polariton states, i.e. polariton CPA, is only one of the experimental achievements detailed in **Chapter 3**. There, we started from the design and characterization of novel metallo-dielectric photonic crystal suspended-membrane resonators, aimed at accessing the polaritonic resonances from the surface and at developing a dispersive polaritonic band which mimicks the dispersion underlying the *polariton bottlenecking*. The surface access is a requisite for simplifying the experimental set-up involved in vacuum photon emission experiments (see below), while the the polariton band dispersion could play a role in stimulated scattering experiments, in analogy with the known observations about exciton-polaritons.

Polariton CPA, or strong critical coupling – which requires the damping rate matching recalled in the above – ensued from the specific values of the $\gamma$'s of a membrane photonic crystal slab resonator and of the mid-infrared intersubband transition. If one's intention is to move SCC into the THz spectral region, suspended photonic crystal are not feasible and double-metal structures have to be considered. Without specific optimization, these structures suffer from a large $\gamma$

mismatch, and another relevant contribution reported in **Chapter 3** is a tuning mechanism of the radiative $\gamma$ based on an etching technique. While this technique allows for an *increase* of $\gamma_r$, we also reported on how to *reduce* $\gamma_r$, now back in a suspended membrane photonic crystal system.

This reduction, observed in defect-mode photonic resonances, is responsible for sudden saturation and bistability of intersubband polaritons, as it follows from a rate-equation model introduced in **Chapter 4**. More in general, in that Chapter we reported on certain non-linear behaviours observed in intersubband polariton samples, with the aim of stating whether polariton-polariton scattering experiments, and vacuum photon emission experiments, are within the experimental reach or not.

By employing a train of ultrashort, high-power mid-infrared light pulses, we showed that the strong coupling is destroyed when an excitation threshold is exceeded; however, this threshold is larger than the stimulated scattering threshold reported in the literature. Together with the possibility of efficiently populate and coherently control the polariton population, this offers potential for a new generation of mid-infrared or terahertz light emitting devices.

A less enthusiastic conclusion is instead drawn in view of the possible detection of vacuum photons. While it is clear that the photonic crystal geometry considerably simplifies the ultrafast switch-on of the strong coupling regime, from the precise knowledge of the experimental set-up and of the samples it turned out that the number of photons emitted per single switch-on event is far less than the minimum detection threshold achievable without radical modifications in the present detection scheme.

In conclusion, photonic crystal resonators offer significant potential for either fundamental physics studies and more application-oriented analysis concerning intersubband polaritons. Last, but not least, it is noteworthy to recall that the metallo-dielectric photonic crystal membrane resonator itself – i.e. when no strong coupling is involved – may play a role in applied devices, like guided mode resonance filters, or quantum well infrared photodetectors. It is especially the latter, either in the ordinary linear or in the two-photon operation regime, that can benefit from the large field enhancement and overlap with the active region intrinsic in the present resonator geometry.

# Appendix A

# Coherent perfect absorption in a general 2-port system

When a linear system coupled to the exterior via a certain number of ports is driven by an input signal, it may happen that a certain amount of the input energy is dissipated by the system itself: this is ordinary *absorption*. A less common configuration is that in which the system is driven through more than one input channel: if the signals are coherent, the amount of input energy which is absorbed may depend on the *phases* of the input beams. This phenomenon is known as *interferometric control of absorption* (ICA), and was first observed experimentally in 2011 [Wan11].

Upon certain conditions, the system can absorb *all* the incoming energy, hence showing perfect absorption. Since this phenomenon relies on the coherence of the input signals, the terminology *coherent perfect absorption* (CPA) has been introduced [Chong10]. The CPA may find applications in integrated optics, for the detection of coherent signals, but it is also a phenomenon of fundamental interest. Indeed, in [Chong10] it has been claimed that the CPA is the time-reversed couterpart of the *lasing*.

In general, the absorption properties of a linear system are linked to certain properties of the scattering matrix, i.e. the matrix that connects input and output amplitudes through the relation $|s^-\rangle = S|s^+\rangle$. Here, $|s^\pm\rangle = (s_1^\pm, \ldots, s_i^\pm, \ldots)$ are the input and output amplitudes in

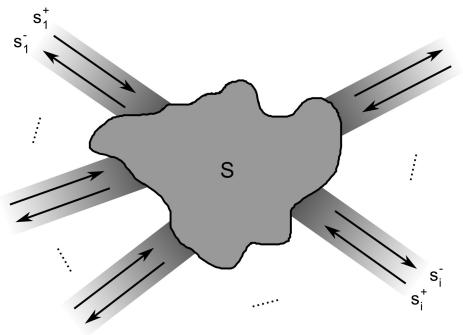


Figure A.1: General scheme of a multiport linear system.

the scattering channels, as sketched in Fig. A.1. The scattering channels are, for instance, plane waves, representing diffraction channels in the case of a photonic crystal slab excited from the free space, or waveguide modes in the case of fiber-coupled resonators, or transmission lines in integrated microwave chips. A suitable normalization has to be chosen, such that $|s_i^{\pm}|^2$ represents the in/out power flux through the $i$-th channel.

If the system conserves energy, $S^\dagger S = SS^\dagger = \mathbf{1}$ and the total output energy flux equals the input energy flux; this condition implies $|\det S| = 1$. If this hypothesis is released, and $|\det S| < 1$, the system can absorb energy from the input channels. Eventually, upon the extreme condition $|\det S| = 0$, there is the possibility of absorbing *all* the input energy. Indeed, the output vector $|s^-\rangle$ can now be the zero vector $|0\rangle$, even when the input vector $|s^+\rangle$ is non-zero. This happens if the input vector is chosen to be the eigenvector corresponding to the zero eigenvalue of the S-matrix. This situation is the *coherent perfect absorption* (CPA) [Chong10].

In the following we will detail the conditions for observing the CPA – and, more in general, the ICA – in the most general, reciprocal[1], 2-port system, by relying on a limited set of significant parameters. Let's start from the scattering matrix. A possible parametrization is the following:

$$S = e^{i\phi} \begin{pmatrix} \rho_1 e^{i\psi_1} & i\tau \\ i\tau & \rho_2 e^{i\psi_2} \end{pmatrix}. \tag{A.1}$$

where $0 < \rho_1, \rho_2, \tau < 1$, and $\phi, \psi_1, \psi_2 \in [0, 2\pi]$. A pair of quantities that

[1]See footnote 7 in Chapter 2 about reciprocity in optical systems.

immediately follow are the ordinary *single-beam absorbances* $A_{1,2} = 1 - \rho_{1,2}^2 - \tau^2$, that measure the ratio [energy absorbed]/[energy in] when one channel at a time is turned on. Clearly, this quantity does not keep track of the phases, neither of the input beam nor of the scattering matrix.

If both input channels are turned on, one can define a *joint absorbance* with the same principle, $A_{\text{joint}} = 1 - \langle s^-|s^-\rangle / \langle s^+|s^+\rangle$. With straightforward algebraic manipulations one gets

$$A_{\text{joint}} = \frac{1+\xi}{2} A_1 + \frac{1-\xi}{2} A_2 - \sqrt{1-\xi^2}\, A_{\text{mod}} \sin(\Delta\phi + \delta) \qquad \text{(A.2)}$$

where

$$\begin{aligned} \xi &= \frac{|s_1^+|^2 - |s_2^+|^2}{|s_1^+|^2 + |s_2^+|^2} \\ \Delta\phi &= \arg(s_1^+ / s_2^+) \\ \tan\delta &= \frac{\rho_2 \sin\psi_2 + \rho_1 \sin\psi_1}{\rho_2 \cos\psi_2 - \rho_1 \cos\psi_1} \\ A_{\text{mod}} &= \sqrt{(1-A_1)(1-A_2) - |\det S|^2}. \end{aligned} \qquad \text{(A.3)}$$

If $\xi = \pm 1$, there is only one input beam active at a time, and the single-beam absorbances are recovered. If $|\xi| \neq 1$, a sweep of the relative phase $\Delta\phi$ between the input beams induces a modulation of the absorbance; this peculiar behaviour is reported in Fig. A.2 (a). In general, sweeping $\xi$ and $\Delta\phi$ does not allow to reach the value $A_{\text{joint}} = 1$, that is, one only observes ICA; however, if $|\det S| = 0$ there exists a set of values $\xi$ and $\Delta\phi$ that imply $A_{\text{joint}} = 1$, i.e. CPA [Fig. A.2 (b)]. In addition, it may happen that the joint absorbance is *zero* for specific $\xi$ and $\Delta\phi$, in a system which is otherwise absorbing: we refer to this phenomenon as *coherent perfect transparency* [CPT, Fig. A.2 (c)].

A deeper look at Fig. A.2 (a) and Eq. A.2 reveals that the maximal absorption modulation in a generic asymmetric system ($A_1 \neq A_2$) always happens at $\xi = 0$. Hence, even under the simultaneous presence of CPA and CPT, an asymmetric system will never lead to full interferometric control of absorption. A full ICA happens *only* if $A_1 = A_2 = A_{\text{mod}} = 1/2$, as reported in Fig. A.2 (d). However, if the asymmetry is "small", a system close to CPA and CPT, anyway exhibits a large absorption modulation depth. This situation is schematized in Fig. A.2 (e), where we also highlighted that a small deviation from the symmetric excitation condition ($\xi = 0$) anyway leads to a large modulation

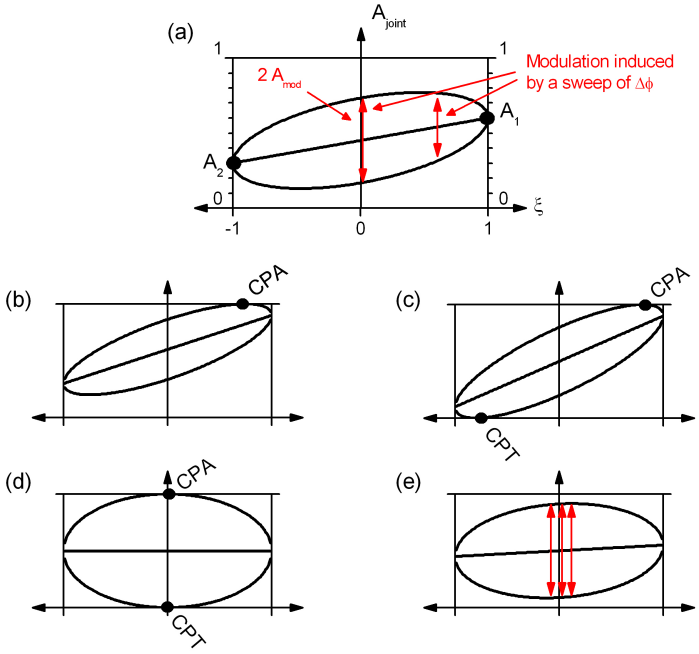


Figure A.2: Global picture of the joint absorbance modulation in a two-port system.

depth. These conditions have been found in the experiment reported in Sect. 3.1.5, where a sample close to *strong critical coupling*, and hence to CPT and CPA, has been analysed.

A final remark is due about the possibility of accessing certain phases of the S-matrix. If one is able to separately measure the two output intensities occurring upon coherent excitation, direct access to the following quantities is achieved:

$$\begin{aligned} |s_1^-|^2 &= \rho_1^2|s_1^+|^2 + \tau^2|s_2^+|^2 + 2\rho_1\tau|s_1^+||s_2^+|\sin(\Delta\phi - \psi_1 + \pi) \\ |s_2^-|^2 &= \rho_2^2|s_1^+|^2 + \tau^2|s_2^+|^2 + 2\rho_2\tau|s_1^+||s_2^+|\sin(\Delta\phi + \psi_2). \end{aligned} \quad \text{(A.4)}$$

The two sinusoidal outputs (Fig. A.3) are dephased by the amounts $(\Delta\phi + \psi_2) - (\Delta\phi - \psi_1 + \pi) = \psi_1 + \psi_2 - \pi$: in essence, even though the *absolute* input beam dephasing is unknown, from an experiment where $\Delta\phi$ is linearly swept[2] one can access the phase *sum* $\psi_1 + \psi_2$.

[2]See Fig. 3.12 in Sect. 3.1.5.

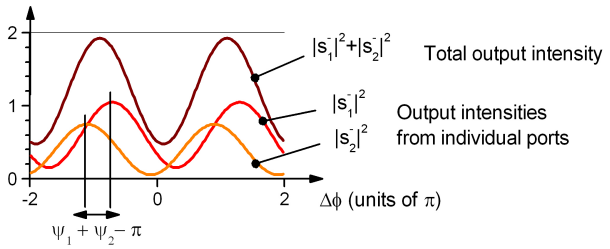


Figure A.3: Output beam intensity upon a sweep of the input beam dephasing $\Delta\phi$. For the illustration, we assumed equal-intensity input beams ($|s_1^+|^2 = |s_2^+|^2 = 1$), and an asymmetric sample ($A_1 \neq A_2$) close to CPT (maximum output intensity close to 2). This situation corresponds to the experimental traces in Fig. 3.12 (a) and (c).

Notice that CPA can be observed only if the two output beams are in phase, i.e. $\psi_1 + \psi_2 = (2m+1)\pi$. This is consistent with the zero determinant requirement: indeed, from (A.1) one gets

$$\det S = 0 \;\leftrightarrow\; \left(\rho_1\rho_2 e^{i(\psi_1+\psi_2)} + \tau^2\right) = 0.$$

By zeroing the imaginary part one gets exactly the condition $\psi_1 + \psi_2 = (2m+1)\pi$; then from the real part one gets $\rho_1\rho_2 = \tau^2$, i.e. the geometric mean of the reflectances must equal the transmittance.

# Appendix B

# Fabrication protocols

In this Appendix we outline the main processing steps involved in the fabrication of the photonic crystal samples analyzed in Sections 3.1, 3.2, 4.1 and 4.2.

The processing is divided in two main blocks: first, definition of the metal grating; second, etching of the substrate until getting a suspended membrane. Clearly, the second step is not performed when fabricating an on-substrate photonic crystal (as for all the samples of Sect. 3.2 and for some of Sect. 4.2).

## Definition of the metal grating

The metal grating is defined via ordinary electron-beam lithography followed by metal deposition and lift-off. Both positive and negative resists have been employed; in the following we report both recipes.

**Sample cleaning**

- Wash the sample in acetone at 50 degrees for at least 5'
- Bake at a temperature between 120 and 180 degrees for burning solvent residuals
- Ash the carbon residuals in $O_2$ plasma (100 W, 3', 5 sccm).

**Positive resist lithography**

- Spin resist AR-P 679-04 for 1' at 4000 rpm
- Bake at 120 degrees for 15'

- Expose at 200 - 300 $\mu C/cm^2$ with 30 kV electron beam
- Develop with AR 600-56 at room temperature for 2', stop in IPA.

**Negative resist lithography**

- Spin adhesion promoter AR 600-56 for 1' at 4000 rpm
- Bake at 180 degrees for 2'
- Spin resist MA-N 2903 for 1' at 4000 rpm
- Bake at 90 degrees for 1'
- Expose at $\simeq$ 60 $\mu C/cm^2$ with 30 kV electron beam
- Develop with MA-D 525 for 1', stop in water.

**Metal deposition and lift-off**

- Descum with $O_2$ plasma (20 W, 60", 12.5 sccm)
- Evaporate 7 nm of Cr and 40 nm of Au
- – *If positive resist*, leave in acetone at room temperature for $\simeq$ 1 hour, or in acetone at 50 degrees for several minutes
  – *If negative resist*, leave in acetone at room temperature overnight, or in acetone at 50 degrees for at least 1 hour
- Lightly sonicate in acetone, in a plastic becher.

As usual for e-beam lithography, the recipe may depend on the specific system under use. We employed both LEO and MERLIN SEMs, always in conjunction with NABITY NanoPattern Generation System. A dose array is strongly reccommended after modifications concerning other processing conditions.

In most of the samples we fabricated, the patterned area is about $500 \times 500$ μm. This area is sufficiently large that optical characterization with free-space propagating mid-infrared light – either incoherent (FTIR) or coherent (ultrafast pulses) – can be carried out with easy alignment and good signal-to-noise ratio. Meanwhile, the time needed for patterning such a surface is not too long. The actual length of the lithographic step crucially depends on the lithography settings: in general, when dealing with large-area structures, it can make the difference between a few-minute and an overnight lithography. We optimized the parameters in such a way that patterning a $500 \times 500$ μm

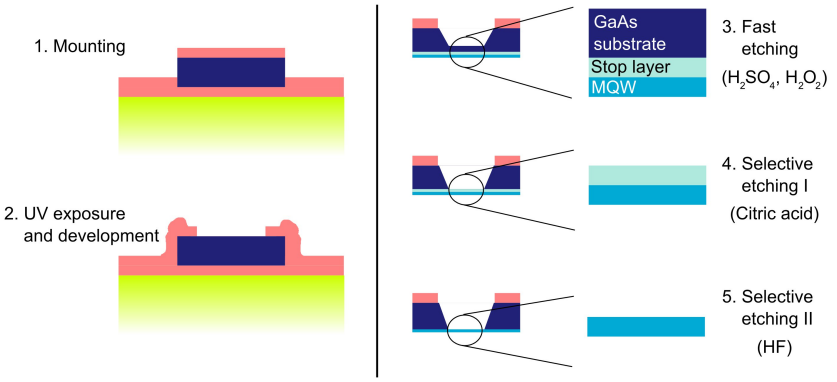


Figure B.1: Main fabrication steps of a photonic crystal membrane.

area with metal stripes having 80 % metal coverage needs about 2 minutes. In details, we set the beam current at 350 pA, center-to-center distance (CCD) at $\simeq$ 20 nm and line spacing (LS) at $\simeq$ 10 nm. In general, the idea is to set the CCD and the LS in order to fulfil the roughness requirements, and then set the current to the maximum value allowed by the beam dwelling time. This works for the NABITY system operated in *continuous writing* mode.

The above figures refer to the negative tone resist, since it was the most employed throughout the doctoral work; it is actually on this resist that we developed most of process optimization. Despite it is not so common to employ a negative e-beam resist for lift-off, given the scarce undercut, it turned out that – as far as less than 50 nm of metal is deposited – the lift-off procedure is easily performed.

## Substrate etching

Photonic crystal slabs are obtained by removing the substrate until the epitaxial layer which defines the photonic crystal membrane is free-standing. This procedure is the most "handcrafted" piece of work, as it has not undergone specific technological development. The main steps are sketched in Fig. B.1; in detail, they are:

**0. Substrate thinning** The sample is mounted on a thickness-control chuck and polished with coarse alumina powder until $\simeq$ 300 μm.

**1. Sample mounting**

- The sample is mounted upside-down on a piece of microscope glass, or on a piece of silicon wafer; baked optical resist S1818 works well as a glue.
- A layer of S1818 is spinned on the sample back surface (3000 rpm for 1').
- Bake the resist at 90 degrees. Two minutes or more are needed since the glass acts as thermal isolator.

**2. Exposure and development**

- Expose the area corresponding to the metal pattern on the other side of the sample.
- Develop in MF319 for 30', stop in water.
- Protect the sample sides by casting a resist border by hand with the pipette.
- Bake for at least 5 minutes at 90 degrees.

**3. Fast etching** Etch the GaAs substrate until reaching $\simeq 50 - 70$ μm less than the total sample thickness measured in Step 0. A "piraña"-like solution is employed: $H_2SO_4 : H_2O_2 : H_2O$ in concentration 1:8:1 attacks about 10 μm per minute. The etching progress is controlled every $\simeq$ 10 minutes in the first phases, and then as necessary. We employed the calibrated focusing knob of an optical microscope for measuring the etched thickness.

**4. Selective etching I** Etch the remaining GaAs substrate until reaching the etch stop layer – either $Al_{0.5}Ga_{0.5}As$ or $Al_{0.95}Ga_{0.05}As$ depending on the heterostructure. The "mountain" appearance typical of GaAs (see the cover image) will become perfectly flat. A 3:1 solution of citric acid in hydrogen peroxide is employed. The citric acid is prepared in 1:1 weight ratio with water. This solution nominally etches 1 μm per minute, but the experience shows that most of the times it is slower[1]. Anyway, if the heterostructure is good, the aluminum content strongly inhibits an attack of the stop layer by means of the citric acid solution.

[1]Faster etching rates can be attained modifying the ratios and the temperature. However, this would imply less selectivity.

5. **Selective etching II** Etch the Al-containing stop layer by means of concentrated hydrofluoric acid (HF). The $\simeq$ 50 % solution commercially available attacks the stop layer in less than one minute, but a process involving more diluted (and less dangerous) solutions could be probably developed. Again, the GaAs layers encountered at the beginning of the MQW are not attacked at all by the HF. Since HF attacks glass, if the sample was mounted on a glass holder, it has to be detached and remounted on a silicon holder before this processing step.

The sample can now be dismounted, with extreme care. Usually, we let it overnight in a Petri glass with acetone, gradually replaced the dirty acetone with clean IPA, and let it dry without blowing. Then, the sample is mounted on a metallic holder in correspondence to a drilled hole. E-beam resist AR-P 679-04 dried for a couple of hours works well as a glue. There are many difficulties inherent to this process:

1. If the sample is not well protected, the etching solution can destroy the sample borders and penetrate up to the metallic pattern.
2. If the starting thickness is not carefully known, or the fast etching is not well controlled, the sample can be easily destroyed.
3. When the membrane is free, the sample has to be manipulated with extreme care.
4. The membrane-defining hole must be aligned with the metal grating.

The last issue has been tackled with two main approaches:

1. Before mounting the sample on the holder, the position of the metal grating with respect to a side of the sample is determined for instance via the calibrated scale of the optical microscope. Then, the optical microscope itself is used for exposing a circular hole in the resist.
2. The gratings are lithographed at given distances from the sample sides, according to an optical mask featuring proper markers. Then, ordinary UV lithography is employed. Although it is more reproducible, this last approach has been employed later since the proper UV mask was unavailable. Actually, the employed mask is a *home-made* mask fabricated via e-beam lithography and ICP-RIE etching of aluminum on a glass substrate.

Apart from being more time-consuming and cumbersome, the first approach does not allow to define large-surface membranes: with the 20x microscope objective holes with $\simeq 1$ mm radius are obtained. On the contrary, with the second approach we fabricated membranes as large as $4 \times 4$ mm wide, hence featuring 9 grating patterns – which means less substrate consumption and larger sweeps of the photonic crystal parameters. The drawback is the sample fragility, that increases with increasing membrane size. However, an attempt to merge sample robustness and simultaneous fabrication of several patterns has been carried out. Namely, we performed the fast etching with a $4 \times 4$ mm hole, followed by a further resist deposition and a lithographic step which defined an array of $500 \times 500$ μm membranes in correspondence to the metal patterns on the other side. Despite the elegance of the approach, it unfortunately turned out that the resulting small-sized membranes exhibit a sharp bending due to residual stress in the epitaxial layers, hence implying the "washing out" of certain spectral features (see Sects. 3.1.1 and 3.1.2).

# Bibliography


[Anappara05] A. A. Anappara, A. Tredicucci, G. Biasiol & L. Sorba. Electrical control of polariton coupling in intersubband microcavities. *Applied Physics Letters*, **87** 051105 (2005). *(Cited on page 113)*

[Anappara06] A. A. Anappara, A. Tredicucci, F. Beltram, G. Biasiol & L. Sorba. Tunnel-assisted manipulation of intersubband polaritons in asymmetric coupled quantum wells. *Applied Physics Letters*, **89** 171109 (2006). *(Cited on page 113)*

[Anappara09] A. A. Anappara, S. De Liberato, A. Tredicucci, C. Ciuti, G. Biasiol, L. Sorba & F. Beltram. Signatures of the ultrastrong light-matter coupling regime. *Phys. Rev. B*, **79** 201303 (2009). *(Cited on pages 4 and 9)*

[Ando82] T. Ando, A. B. Fowler & F. Stern. Electronic properties of two-dimensional systems. *Rev. Mod. Phys.*, **54** 437 (1982). *(Cited on page 10)*

[Andreani99] L. C. Andreani, G. Panzarini & J.-M. Gérard. Strong-coupling regime for quantum boxes in pillar microcavities: Theory. *Phys. Rev. B*, **60** 13276 (1999). *(Cited on pages 25 and 35)*

[Auffèves-Garnier07] A. Auffèves-Garnier, C. Simon, J.-M. Gérard & J.-P. Poizat. Giant optical nonlinearity induced by a single two-level system interacting with a cavity in the Purcell regime. *Phys. Rev. A*, **75** 053823 (2007). *(Cited on pages 30 and 41)*

[Baas04] A. Baas, J. P. Karr, H. Eleuch & E. Giacobino. Optical bistability in semiconductor microcavities. *Phys. Rev. A*, **69** 023809 (2004). *(Cited on page 110)*

[Bajoni08] D. Bajoni, E. Semenova, A. Lemaitre, S. Bouchoule, E. Wertz, P. Senellart, S. Barbay, R. Kuszelewicz & J. Bloch. Optical bistability in a GaAs-based polariton diode. *Phys. Rev. Lett.*, **101** 266402 (2008). *(Cited on page 110)*

[Bastard88] G. Bastard. *Wave Mechanics applied to Semiconductor Heterostructures*. Les Editions de Physique (1988). *(Cited on page 6)*

[Born99] M. Born & E. Wolf. *Principles of Optics*. Cambridge University Press (1999). *(Cited on pages 23 and 56)*

[Cai00] M. Cai, O. Painter & K. J. Vahala. Observation of critical coupling in a fiber taper to a silica-microsphere whispering-gallery mode system. *Phys. Rev. Lett.*, **85** 74 (2000). *(Cited on pages 29 and 36)*

[Cao02] Q. Cao & P. Lalanne. Negative role of surface plasmons in the transmission of metallic gratings with very narrow slits. *Phys. Rev. Lett.*, **88** 057403 (2002). *(Cited on page 54)*

[Chassagneux09] Y. Chassagneux, R. Colombelli, W. Maineult, S. Barbieri, H. E. Beere, D. A. Ritchie, S. P. Khanna, E. H. Linfield & A. G. Davies. Electrically pumped photonic-crystal terahertz lasers controlled by boundary conditions. *Nature*, **457** 174 (2009). *(Cited on page 85)*

[Chassagneux10] Y. Chassagneux, R. Colombelli, W. Maineult, S. Barbieri, S. P. Khanna, E. H. Linfield & A. G. Davies. Graded photonic crystal terahertz quantum cascade lasers. *Applied Physics Letters*, **96** 031104 (2010). *(Cited on page 60)*

[Chong10] Y. D. Chong, L. Ge, H. Cao & A. D. Stone. Coherent perfect absorbers: Time-reversed lasers. *Phys. Rev. Lett.*, **105** 053901 (2010). *(Cited on pages 30, 44, 125, and 126)*

[Christ03] A. Christ, S. G. Tikhodeev, N. A. Gippius, J. Kuhl & H. Giessen. Waveguide-plasmon polaritons: Strong coupling of photonic and electronic resonances in a metallic photonic crystal slab. *Phys. Rev. Lett.*, **91** 183901 (2003). *(Cited on page 54)*

[Christ04] A. Christ, T. Zentgraf, J. Kuhl, S. G. Tikhodeev, N. A. Gippius & H. Giessen. Optical properties of planar metallic photonic crystal structures: experiment and theory. *Phys. Rev. B*, **70** 125113 (2004). *(Cited on page 54)*

[Chutinan08] A. Chutinan & S. John. Light trapping and absorption optimization in certain thin-film photonic crystal architectures. *Phys. Rev. A*, **78** 023825 (2008). *(Cited on page 45)*

[Ciuti05] C. Ciuti, G. Bastard & I. Carusotto. Quantum vacuum properties of the intersubband cavity polariton field. *Phys. Rev. B*, **72** 115303 (2005). *(Cited on pages 9, 17, 18, 22, and 113)*

[Ciuti06] C. Ciuti & I. Carusotto. Input-output theory of cavities in the ultrastrong coupling regime: The case of time-independent cavity parameters. *Phys. Rev. A*, **74** 033811 (2006). *(Cited on pages 19 and 25)*

[De Liberato07] S. De Liberato, C. Ciuti & I. Carusotto. Quantum vacuum radiation spectra from a semiconductor microcavity with a time-modulated vacuum rabi frequency. *Phys. Rev. Lett.*, **98** 103602 (2007). *(Cited on page 113)*

[De Liberato08] S. De Liberato & C. Ciuti. Quantum model of microcavity intersubband electroluminescent devices. *Phys. Rev. B*, **77** 155321 (2008). *(Cited on page 25)*

[De Liberato09a] S. De Liberato. *Cavity quantum electrodynamics and intersubband polaritonics of a two dimensional electron gas*. Ph.D. thesis, Université Paris Diderot (Paris 7) (2009). *(Cited on pages 14, 15, 113, 116, 118, and 119)*

[De Liberato09b] S. De Liberato & C. Ciuti. Quantum theory of electron tunneling into intersubband cavity polariton states. *Phys. Rev. B*, **79** 075317 (2009). *(Cited on page 25)*

[De Liberato09c] S. De Liberato & C. Ciuti. Stimulated scattering and lasing of intersubband cavity polaritons. *Phys. Rev. Lett.*, **102** 136403 (2009). *(Cited on pages 2, 30, 39, 49, 95, and 111)*

[De Liberato13] S. De Liberato, C. Ciuti & C. C. Phillips. Terahertz lasing from intersubband polariton-polariton scattering in asymmetric quantum wells. *Phys. Rev. B*, **87** 241304 (2013). *(Cited on pages 2, 30, 39, and 49)*

[Delteil11] A. Delteil, A. Vasanelli, P. Jouy, D. Barate, J. C. Moreno, R. Teissier, A. N. Baranov & C. Sirtori. Optical phonon scattering of cavity polaritons in an electroluminescent device. *Phys. Rev. B*, **83** 081404 (2011). *(Cited on pages 19 and 95)*

[Dini03] D. Dini, R. Köhler, A. Tredicucci, G. Biasiol & L. Sorba. Microcavity polariton splitting of intersubband transitions. *Phys. Rev. Lett.*, **90** 116401 (2003). *(Cited on pages 2, 3, and 23)*

[Duboz95] J. Y. Duboz, E. Costard, E. Rosencher, P. Bois, J. Nagle, J. M. Berset, D. Jaroszynski & J. M. Ortega. Electron relaxation time measurements in GaAs/AlGaAs quantum wells: Intersubband absorption saturation by a free-electron laser. *Journal of Applied Physics*, **77** 6492 (1995). *(Cited on page 103)*

[Ebbesen98] T. W. Ebbesen, H. J. Lezec, H. F. Ghaemi, T. Thio & P. A. Wolff. Extraordinary optical transmission through sub-wavelength hole arrays. *Nature*, **391** 667 (1998). *(Cited on page 54)*

[Fan03] S. Fan, W. Suh & J. D. Joannopoulos. Temporal coupled-mode theory for the Fano resonance in optical resonators. *J. Opt. Soc. Am. A*, **20** 569 (2003). *(Cited on pages 29, 40, 41, 42, 54, and 59)*

[Fan06] J. A. Fan, M. A. Belkin, F. Capasso, S. Khanna, M. Lachab, A. G. Davies, E. H. Linfield *et al.* Surface emitting terahertz quantum cascade laser with a double-metal waveguide. *Opt. Express*, **14** 11672 (2006). *(Cited on pages 59 and 85)*

[Feuillet-Palma12] C. Feuillet-Palma, Y. Todorov, R. Steed, A. Vasanelli, G. Biasiol, L. Sorba & C. Sirtori. Extremely sub-wavelength THz metal-dielectric wire microcavities. *Opt. Express*, **20** 29121 (2012). *(Cited on page 18)*

[Gansch11] R. Gansch, S. Kalchmair, H. Detz, A. M. Andrews, P. Klang, W. Schrenk & G. Strasser. Higher order modes in photonic crystal slabs. *Opt. Express*, **19** 15990 (2011). *(Cited on page 61)*

[Geiser10] M. Geiser, C. Walther, G. Scalari, M. Beck, M. Fischer, L. Nevou & J. Faist. Strong light-matter coupling at terahertz frequencies at room temperature in electronic LC resonators. *Applied Physics Letters*, **97** 191107 (2010). *(Cited on page 3)*

[Gerace04] D. Gerace & L. C. Andreani. Gap maps and intrinsic diffraction losses in one-dimensional photonic crystal slabs. *Phys. Rev. E*, **69** 056603 (2004). *(Cited on page 55)*

[Gerace07] D. Gerace & L. C. Andreani. Quantum theory of exciton-photon coupling in photonic crystal slabs with embedded quantum wells. *Phys. Rev. B*, **75** 235325 (2007). *(Cited on page 18)*

[Granet96] G. Granet & B. Guizal. Efficient implementation of the coupled-wave method for metallic lamellar gratings in TM polarization. *J. Opt. Soc. Am. A*, **13** 1019 (1996). *(Cited on page 58)*

[Günter09] G. Günter, A. A. Anappara, J. Hees, A. Sell, G. Biasiol, L. Sorba, S. De Liberato, C. Ciuti, A. Tredicucci, A. Leitenstorfer & R. Huber. Sub-cycle switch-on of ultrastrong light-matter interaction. *Nature*, **458** 178 (2009). *(Cited on pages 4, 96, 113, and 116)*

[Haus84] H. A. Haus. *Waves and fields in optoelectronics*. Prentice-Hall (1984). *(Cited on pages 3, 29, and 36)*

[Hoop60] A. Hoop. A reciprocity theorem for the electromagnetic field scattered by an obstacle. *Applied Scientific Research, Section B*, **8** 135 (1960). *(Cited on page 40)*

[Houdré95] R. Houdré, J. L. Gibernon, P. Pellandini, R. P. Stanley, U. Oesterle, C. Weisbuch, J. O'Gorman, B. Roycroft & M. Ilegems. Saturation of the strong-coupling regime in a semiconductor microcavity: Free-carrier bleaching of cavity polaritons. *Phys. Rev. B*, **52** 7810 (1995). *(Cited on pages 4 and 96)*

[Jalas13] D. Jalas, A. Petrov, M. Eich, W. Freude, S. Fan, Z. Yu, R. Baets, M. Popovic, A. Melloni, J. D. Joannopoulos, M. Vanwolleghem, C. R. Doerr & H. Renner. What is

– and what is not – an optical isolator. *Nature Photonics*, **7** 579 (2013). *(Cited on page 40)*

[Joannopoulos95] J. D. Joannopoulos, S. G. Johnson, J. N. Winn & R. D. Meade. *Photonic Crystals*. Princeton University Press (1995). *(Cited on pages 53 and 60)*

[Jouy11a] P. Jouy, Y. Todorov, A. Vasanelli, R. Colombelli, I. Sagnes & C. Sirtori. Coupling of a surface plasmon with localized subwavelength microcavity modes. *Applied Physics Letters*, **98** 021105 (2011). *(Cited on page 86)*

[Jouy11b] P. Jouy, A. Vasanelli, Y. Todorov, A. Delteil, G. Biasiol, L. Sorba & C. Sirtori. Transition from strong to ultrastrong coupling regime in mid-infrared metal-dielectric-metal cavities. *Applied Physics Letters*, **98** 231114 (2011). *(Cited on page 86)*

[Julien88] F. H. Julien, J.-M. Lourtioz, N. Herschkorn, D. Delacourt, J. P. Pocholle, M. Papuchon, R. Planel & G. L. Roux. Optical saturation of intersubband absorption in $GaAs - Al_xGa_{1-x}As$ quantum wells. *Applied Physics Letters*, **53** 116 (1988). *(Cited on page 103)*

[Kaindl01] R. A. Kaindl, K. Reimann, M. Woerner, T. Elsaesser, R. Hey & K. H. Ploog. Homogeneous broadening and excitation-induced dephasing of intersubband transitions in a quasi-two-dimensional electron gas. *Phys. Rev. B*, **63** 161308 (2001). *(Cited on page 103)*

[Kalchmair11] S. Kalchmair, H. Detz, G. D. Cole, A. M. Andrews, P. Klang, M. Nobile, R. Gansch, C. Ostermaier, W. Schrenk & G. Strasser. Photonic crystal slab quantum well infrared photodetector. *Applied Physics Letters*, **98** 011105 (2011). *(Cited on page 61)*

[Kaluzny83] Y. Kaluzny, P. Goy, M. Gross, J. M. Raimond & S. Haroche. Observation of self-induced rabi oscillations in two-level atoms excited inside a resonant cavity: The ringing regime of superradiance. *Phys. Rev. Lett.*, **51** 1175 (1983). *(Cited on page 1)*

[Kats12] M. A. Kats, D. Sharma, J. Lin, P. Genevet, R. Blanchard, Z. Yang, M. M. Qazilbash, D. N. Basov, S. Ramanathan

& F. Capasso. Ultra-thin perfect absorber employing a tunable phase change material. *Applied Physics Letters*, **101** 221101 (2012). *(Cited on page 36)*

[Kavokin07] A. V. Kavokin, J. J. Baumberg, G. Malpuech & F. P. Laussy. *Microcavities*. Oxford University Press (2007). *(Cited on pages 2 and 15)*

[Lalanne96] P. Lalanne & G. M. Morris. Highly improved convergence of the coupled-wave method for tm polarization. *J. Opt. Soc. Am. A*, **13** 779 (1996). *(Cited on page 62)*

[Li96] L. Li. Use of fourier series in the analysis of discontinuous periodic structures. *J. Opt. Soc. Am. A*, **13** 1870 (1996). *(Cited on page 62)*

[Liscidini08] M. Liscidini, D. Gerace, L. C. Andreani & J. E. Sipe. Scattering-matrix analysis of periodically patterned multilayers with asymmetric unit cells and birefringent media. *Phys. Rev. B*, **77** 035324 (2008). *(Cited on page 58)*

[Liu97] A. Liu. Rabi splitting of the optical intersubband absorption line of multiple quantum wells inside a Fabry-Pérot microcavity. *Phys. Rev. B*, **55** 7101 (1997). *(Cited on page 2)*

[Lourtioz08] J.-M. Lourtioz, H. Benisty, V. Berger, J.-M. Gerard & D. Maystre. *Photonic Crystals: Towards Nanoscale Photonic Devices*. Springer (2008). *(Cited on pages 54, 60, and 63)*

[Manceau13] J.-M. Manceau, S. Zanotto, I. Sagnes, G. Beaudoin & R. Colombelli. Optical critical coupling into highly confining metal-insulator-metal resonators. *Applied Physics Letters*, **103** 091110 (2013). *(Cited on pages 89 and 91)*

[Marquier05] F. Marquier, J.-J. Greffet, S. Collin, F. Pardo & J. Pelouard. Resonant transmission through a metallic film due to coupled modes. *Opt. Express*, **13** 70 (2005). *(Cited on page 54)*

[Martín-Moreno01] L. Martín-Moreno, F. J. García-Vidal, H. J. Lezec, K. M. Pellerin, T. Thio, J. B. Pendry & T. W. Ebbesen. Theory of extraordinary optical transmission through subwavelength hole arrays. *Phys. Rev. Lett.*, **86** 1114 (2001). *(Cited on page 54)*

[Nau07] D. Nau, A. Schönhardt, C. Bauer, A. Christ, T. Zentgraf, J. Kuhl, M. W. Klein & H. Giessen. Correlation effects in disordered metallic photonic crystal slabs. *Phys. Rev. Lett.*, **98** 133902 (2007). *(Cited on page 54)*

[Noda07] S. Noda, M. Fujita & T. Asano. Spontaneous-emission control by photonic crystals and nanocavities. *Nature Photonics*, **1** 449 (2007). *(Cited on page 60)*

[Norris95] T. B. Norris, J. K. Rhee, D. S. Citrin, M. Nishioka & Y. Arakawa. Coherent and incoherent dynamics of excitons in semiconductor microcavities. *Il Nuovo Cimento*, **17** 1295 (1995). *(Cited on pages 4 and 96)*

[Ordal83] M. A. Ordal, L. L. Long, R. J. Bell, S. E. Bell, R. R. Bell, J. R. W. Alexander & C. A. Ward. Optical properties of the metals Al, Co, Cu, Au, Fe, Pb, Ni, Pd, Pt, Ag, Ti, and W in the infrared and far infrared. *Appl. Opt.*, **22** 1099 (1983). *(Cited on page 89)*

[Palik91] E. Palik. *Handbook of Optical Constants of Solids*. Academic Press (1991). *(Cited on page 89)*

[Peretti12] R. Peretti, G. Gomard, C. Seassal, X. Letartre & E. Drouard. Modal approach for tailoring the absorption in a photonic crystal membrane. *Journal of Applied Physics*, **111** 123114 (2012). *(Cited on page 45)*

[Porer12] M. Porer, J.-M. Ménard, A. Leitenstorfer, R. Huber, R. Degl'Innocenti, S. Zanotto, G. Biasiol, L. Sorba & A. Tredicucci. Nonadiabatic switching of a photonic band structure: Ultrastrong light-matter coupling and slow-down of light. *Phys. Rev. B*, **85** 081302 (2012). *(Cited on page 114)*

[Pozar12] D. M. Pozar. *Microwave Engineering*. Wiley (2012). *(Cited on page 85)*

[Reithmaier04] J. P. Reithmaier, G. Sek, A. Loffler, C. Hofmann, S. Kuhn, S. Reitzenstein, L. V. Keldysh, V. D. Kulakovskii, T. L. Reinecke & A. Forchel. Strong coupling in a single quantum dot-semiconductor microcavity system. *Nature*, **432** 197 (2004). *(Cited on page 60)*

[Rosenberg10] J. Rosenberg, R. V. Shenoi, S. Krishna & O. Painter. Design of plasmonic photonic crystal resonant cavities for polarization sensitive infrared photodetectors. *Opt. Express*, **18** 3672 (2010). *(Cited on pages 36 and 61)*

[Sakat11] E. Sakat, G. Vincent, P. Ghenuche, N. Bardou, S. Collin, F. Pardo, J.-L. Pelouard & R. Haïdar. Guided mode resonance in subwavelength metallodielectric free-standing grating for bandpass filtering. *Opt. Lett.*, **36** 3054 (2011). *(Cited on page 61)*

[Sakat12] E. Sakat, G. Vincent, P. Ghenuche, N. Bardou, C. Dupuis, S. Collin, F. Pardo, R. Haïdar & J.-L. Pelouard. Free-standing guided-mode resonance band-pass filters: from 1d to 2d structures. *Opt. Express*, **20** 13082 (2012). *(Cited on page 61)*

[Sarrazin03] M. Sarrazin, J.-P. Vigneron & J.-M. Vigoureux. Role of Wood anomalies in optical properties of thin metallic films with a bidimensional array of subwavelength holes. *Phys. Rev. B*, **67** 085415 (2003). *(Cited on page 54)*

[Schartner08] S. Schartner, M. Nobile, W. Schrenk, A. M. Andrews, P. Klang & G. Strasser. Photocurrent response from photonic crystal defect modes. *Opt. Express*, **16** 4797 (2008). *(Cited on page 61)*

[Schneider08] H. Schneider, H. C. Liu, S. Winnerl, O. Drachenko, M. Helm & J. Faist. Room-temperature midinfrared two-photon photodetector. *Applied Physics Letters*, **93** 101114 (2008). *(Cited on page 61)*

[Shen09a] J.-T. Shen & S. Fan. Theory of single-photon transport in a single-mode waveguide. i. coupling to a cavity containing a two-level atom. *Phys. Rev. A*, **79** 023837 (2009). *(Cited on page 30)*

[Shen09b] J.-T. Shen & S. Fan. Theory of single-photon transport in a single-mode waveguide. ii. coupling to a whispering-gallery resonator containing a two-level atom. *Phys. Rev. A*, **79** 023838 (2009). *(Cited on page 30)*

[Shen10] J.-T. Shen & S. Fan. Quantum critical coupling conditions for zero single-photon transmission through a coupled atom-resonator-waveguide system. *Phys. Rev. A*, **82** 021802 (2010). *(Cited on page 30)*

[Srinivasan07] K. Srinivasan & O. Painter. Mode coupling and cavity–quantum-dot interactions in a fiber-coupled microdisk cavity. *Phys. Rev. A*, **75** 023814 (2007). *(Cited on page 30)*

[Stade05] E. Stade. *Fourier analysis*. Wiley-Interscience (2005). *(Cited on page 99)*

[Tassone97] F. Tassone, C. Piermarocchi, V. Savona, A. Quattropani & P. Schwendimann. Bottleneck effects in the relaxation and photoluminescence of microcavity polaritons. *Phys. Rev. B*, **56** 7554 (1997). *(Cited on pages 51 and 86)*

[Thompson92] R. J. Thompson, G. Rempe & H. J. Kimble. Observation of normal-mode splitting for an atom in an optical cavity. *Phys. Rev. Lett.*, **68** 1132 (1992). *(Cited on pages 1 and 83)*

[Todorov09] Y. Todorov, A. M. Andrews, I. Sagnes, R. Colombelli, P. Klang, G. Strasser & C. Sirtori. Strong light-matter coupling in subwavelength metal-dielectric microcavities at terahertz frequencies. *Phys. Rev. Lett.*, **102** 186402 (2009). *(Cited on pages 3, 9, 86, and 119)*

[Todorov10a] Y. Todorov, A. M. Andrews, R. Colombelli, S. De Liberato, C. Ciuti, P. Klang, G. Strasser & C. Sirtori. Ultrastrong light-matter coupling regime with polariton dots. *Phys. Rev. Lett.*, **105** 196402 (2010). *(Cited on pages 86 and 119)*

[Todorov10b] Y. Todorov, L. Tosetto, J. Teissier, A. M. Andrews, P. Klang, R. Colombelli, I. Sagnes, G. Strasser & C. Sirtori. Optical properties of metal-dielectric-metal microcavities in the THz frequency range. *Opt. Express*, **18** 13886 (2010). *(Cited on page 86)*

[Todorov12] Y. Todorov & C. Sirtori. Intersubband polaritons in the electrical dipole gauge. *Phys. Rev. B*, **85** 045304 (2012). *(Cited on pages 7, 10, 18, and 27)*

[Tredicucci96] A. Tredicucci, Y. Chen, V. Pellegrini, M. Börger & F. Bassani. Optical bistability of semiconductor microcavities in the strong-coupling regime. *Phys. Rev. A*, **54** 3493 (1996). *(Cited on page 110)*

[Wan11] W. Wan, Y. Chong, L. Ge, H. Noh, A. D. Stone & H. Cao. Time-reversed lasing and interferometric control of absorption. *Science*, **331** 889 (2011). *(Cited on pages 44, 47, and 125)*

[Weisbuch92] C. Weisbuch, M. Nishioka, A. Ishikawa & Y. Arakawa. Observation of the coupled exciton-photon mode splitting in a semiconductor quantum microcavity. *Phys. Rev. Lett.*, **69** 3314 (1992). *(Cited on pages 2 and 96)*

[Whittaker99] D. M. Whittaker & I. S. Culshaw. Scattering-matrix treatment of patterned multilayer photonic structures. *Phys. Rev. B*, **60** 2610 (1999). *(Cited on page 58)*

[Williams03] B. S. Williams, S. Kumar, H. Callebaut, Q. Hu & J. L. Reno. Terahertz quantum-cascade laser at $\lambda \simeq 100\mu$m using metal waveguide for mode confinement. *Applied Physics Letters*, **83** (2003). *(Cited on page 85)*

[Xu12] G. Xu, R. Colombelli, S. P. Khanna, A. Belarouci, X. Letartre, L. Li, E. H. Linfield, A. G. Davies, H. E. Beere & D. A. Ritchie. Efficient power extraction in surface-emitting semiconductor lasers using graded photonic heterostructures. *Nature Communications*, **3** 952 (2012). *(Cited on page 60)*

[Yariv07] A. Yariv & P. Yeh. *Photonics: Optical Electronics in Modern Communication*. Oxford University Press (2007). *(Cited on pages 3, 8, and 62)*

[Yoshie04] T. Yoshie, A. Scherer, J. Hendrickson, G. Khitrova, H. M. Gibbs, G. Rupper, C. Ell, O. B. Shchekin & D. G. Deppe. Vacuum Rabi splitting with a single quantum dot in a photonic crystal nanocavity. *Nature*, **432** 200 (2004). *(Cited on page 60)*

[Yu12] Z. Yu, A. Raman & S. Fan. Thermodynamic upper bound on broadband light coupling with photonic structures. *Phys. Rev. Lett.*, **109** 173901 (2012). *(Cited on page 36)*

[Załużny99] M. Załużny & C. Nalewajko. Coupling of infrared radiation to intersubband transitions in multiple quantum wells: The effective-medium approach. *Phys. Rev. B*, **59** 13043 (1999). *(Cited on page 25)*

[Załużny09] M. Załużny & W. Zietkowski. Intersubband cavity polaritons: The role of higher photonic modes. *Phys. Rev. B*, **80** 245301 (2009). *(Cited on page 18)*

[Zanotto10] S. Zanotto, M. Liscidini & L. C. Andreani. Light trapping regimes in thin-film silicon solar cells with a photonic pattern. *Opt. Express*, **18** 4260 (2010). *(Cited on page 60)*

[Zanotto12] S. Zanotto, R. Degl'Innocenti, L. Sorba, A. Tredicucci & G. Biasiol. Analysis of line shapes and strong coupling with intersubband transitions in one-dimensional metallodielectric photonic crystal slabs. *Phys. Rev. B*, **85** 035307 (2012). *(Cited on pages 10 and 18)*

[Zentgraf06] T. Zentgraf, A. Christ, J. Kuhl, N. A. Gippius, S. G. Tikhodeev, D. Nau & H. Giessen. Metallodielectric photonic crystal superlattices: Influence of periodic defects on transmission properties. *Phys. Rev. B*, **73** 115103 (2006). *(Cited on page 54)*

# Acknowledgements

This thesis, and more in general the path through which I walked in the last years, is the result of a hard work where the contribution of many people played a fundamental role. Support in the laboratory, suggestions in the cleanroom, ideas in the brainstorming; but also encouragement in the troubles, fun in the free time, and enjoying the fantastic lands of Pisa and Toscana. For this reason I hearthly acknowledge all my colleagues and friends of NEST and Scuola Normale: Alessandro, Lorenzo, Luca, Riccardo, Ji-Hua, Federica, Fabrizio, Miriam, Giorgio, Emanuela, Marco, Sandro, Vito, Maria, Pepa, Mario, Antonio, Jonna, Alberto, Camilla... Last, but not least, Federico, Alice, Leonardo, Gaia and Chiara.

I am deeply indebted with my advisor, Alessandro, for his continuous support and for the physical insight, and to Raffaele for the fruitful period in Paris.

A special mention is for Giulio Rampa, who passed away too early with his special passion for physics. This work is dedicated to him, since his incentive had a special weight in my decision to join the PhD course in Scuola Normale.

Finally, there is probably no way to fully communicate a "thank you" to my family, never ending source of support and confidence for the future.